Available online at www.sciencedirect.com
ScienceDirect
Progress in Crystal Growth and Characterization of Materials
53 (2007) 1–56
Progress in Crystal Growth and Characterization of Materials
www.elsevier.com/locate/pcrysgrow

Raman Spectroscopy of nanomaterials: How spectra relate to disorder, particle size and mechanical properties

Gwénaël Gouadec*, Philippe Colomban

Laboratoire de Dynamique, Interactions et Réactivité (LADIR), UMR7075 – CNRS & Université Pierre et Marie Curie – Paris 6, 2 rue Henry Dunant, 94320 Thiais, France

Abstract

The purpose of this review is to provide non-specialists with a basic understanding of the information micro-Raman Spectroscopy (μRS) may yield when this characterization tool is applied to nanomaterials, a generic term for describing nano-sized crystals and bulk homogeneous materials with a structural disorder at the nanoscale – typically nanoceramics, nanocomposites, glassy materials and relaxor ferroelectrics. The selected materials include advanced and ancient ceramics, semiconductors and polymers developed in the form of dots, wires, films, fibres or composites for applications in the energy, electronic and aeronautics–aerospace industries. The text is divided into five sections:

- Section 1 is a general introduction.
- Section 2 outlines the principles of conventional μRS.
- Section 3 introduces the main effects for nanomaterials, with special emphasis on two models that connect Raman spectra features to ''grain size'', namely the Phonon Confinement Model (PCM) and the Elastic Sphere Model (ESM).
- Section 4 presents the experimental versatility of μRS applied to nanomaterials (phase identification, phase transition monitoring, grain size determination, defect concentration assessment, etc.).

* Corresponding author. Tel.: +33 1 49 78 11 07; fax: +33 1 49 78 13 18.
E-mail address: gouadec@glvt-cnrs.fr (G. Gouadec).

0960-8974/$ - see front matter
doi:10.1016/j.pcrysgrow.2007.01.001

- Section 5 deals with the micro-mechanical aspects of μRS (''Raman extensometry''). Special emphasis is placed on the relationship between the stress-related coefficients $S^{\varepsilon/\sigma}$ and the macroscopic response of the materials to the applied stress.

PACS: 63.20.-e; 63.50.+x; 78.30.-j; 81.40.Jj; 81.05.Ys

Keywords: A1. Raman Spectroscopy; A1. Disorder; A1. Stress; B1. Nanomaterials; B1. Nanotubes; B1. Oxides; B2. Semiconductors; B2. Carbon; B1. Glasses

1. Introduction

Most properties of traditional ceramics (notably a good shapability and low sintering temperatures) stem from the fact that their raw material – natural clay – is nanosized [1]. Besides, because of the sharpness of the human eye, the size of the pigment particles must be smaller than 500 nm to homogeneously colour enamels and glasses [2]. Potters and ceramists have thus been using nanoscience for thousands of years [3,4] but a new generation of engineered nanomaterials (grain size < 100 nm) has been in development – if not already commercially available – for the last 20 years. Reducing the dimension of matter domains down to the nanometer scale confines the electronic and vibrational wavefunctions while increasing the specific surface, which results in unique properties and opens a wide range of potential applications in domains as different as [5–8]:

Optics: pigments for the cosmetic industry (metal-oxides), fluorescent markers (quantum dots), photonic crystals (multiplexing and switching in optical networks), quantum computer components, light emitting devices [9], etc.
Mechanics: cutting tools, wear-resistant and anti-corrosion coatings (cemented carbides), ''nano-polishing'' powders (SiC, diamond, boron carbide), fibres and fibre-reinforced composites, structural nanocomposites [10], etc.
Electrical devices: miniaturized silicon chips, single electron transistors, relaxor ferroelectrics [11–14], carbon or silicon nanotube transistors, lithium batteries [15], solar cells [16], etc.
Magnetic devices: data storage, giant magneto-resistances (reading heads), etc.
Reactivity: improved combustion of fuel-rich propellants (Al, Ti, Ni, B) [17], filters (Ti/Zr oxides), nanosensors [18,19], catalysts [20], etc.
Biomedicine: in vivo drug delivery, diagnostic devices [21], fluorescent markers for imaging, etc.

The challenge for the so-called nanotechnologies is to achieve perfect control of nanoscale-related properties. This obviously requires correlating the parameters of the synthesis process (self-assembly, microlithography, sol–gel, polymer curing, electrochemical deposition, laser ablation, etc.) with the resulting nanostructure. Not every conventional characterization technique is suitable for that purpose but Raman Spectroscopy (RS) has already proven to be. For quite a long time this technique was mainly devoted to fundamental research, but instrumental progress (laser miniaturization, CCD detection, notch filters and data processing softwares) have rendered it a general characterization method. Not only can it provide basic phase identification but also subtle spectra alterations can be used to assess nano-scale structural changes and characterize micromechanical behaviour. RS is thus a unique tool for probing or mapping nanophases dispersed in a matrix (e.g. pigments in a ceramic glaze [2], precipitates

in a fibre coating [22]), surface-formed nanophases (corrosion mechanisms [23]) and solid-state devices [24–27]. Some specific features can even be used to study a charge transfer [28,29], a film orientation [30], the size of clusters trapped in nano-cavities [31], Grüneisen's parameter [32], configurational order (for instance the proportion of trans-gauche chains in Poly(ethylene terephtalate)-PET [33]) or intercalation [34], interfacial [35] and polymerisation [36] reactions.

The present review, which is an extended version of previous papers from our group [37–39], is intended to review the achievements of RS in the world of nanomaterials, both from the fundamental and experimental points of view. The selected materials include advanced and ancient ceramics, glasses, semiconductors and polymers developed in the form of dots, wires, films, fibres or composites for applications in the energy, electronic and aeronautics–aerospace industries. The interested reader will find useful complementary information in Refs. [40–43] and a special issue of the Journal of Raman Spectroscopy [44].

2. The fundamentals of Raman Spectroscopy

2.1. Vibrations in crystalline solids

All collective vibrations that occur in crystals can be viewed as the superposition of plane waves that virtually propagate to infinity [45]. These plane waves, the so-called normal modes of vibration, are commonly modelled by quasi-particles called *phonons*. A normal coordinate of the form $Q = Q_0\cos(2\pi\nu_{\text{vib}}t)$, which is actually a linear combination of bond lengths and bond angles, is associated with each normal mode. Depending on the dominant term in the normal coordinate, modes can be classified as either stretching (ν), bending (δ), torsional (τ), librational (R′/T′ pseudo-rotations/translations) or lattice modes (the latter include the relative displacement of the unit cells).

For a three-dimensional (3D) solid containing N unit cells with p atoms each, $(3pN - 6)$ different phonons can propagate[1] and their wavevectors ($\vec{\mathbf{k}}$) all point in a volume of the reciprocal space called the Brillouin Zone (BZ).[2] There are modes with in-phase oscillations of neighbouring atoms and modes with out of phase oscillations. The former are called acoustic vibrations and the latter are called optical vibrations. On the other hand, phonons are referred to as being longitudinal or transversal depending on whether the atoms move parallel or perpendicular to the direction of the wave propagation given by $\vec{\mathbf{k}}$. Phonons with the same two criteria are all gathered in the BZ on $3p$ (discrete) lines called the dispersion branches (see an example in Fig. 17). Fig. 1 is an illustration of the concept of phonons in crystals showing the transverse vibrations in a one-dimensional lattice where $p = 2$.

2.2. The Raman Effect

The polarization of the dipoles excited in solids when a laser beam (amplitude E_0; frequency ν_{las}) interacts with phonons of frequency ν_{vib} depends on the polarisability tensor $\overline{\overline{\alpha}}$:

$$\vec{P} = \overline{\overline{\alpha}} \times \vec{E}_0\cos(2\pi\nu_{\text{las}}t) \tag{1}$$

[1] There are $3pN$ degrees of freedom but the six rotations and translations of the whole solid are not considered to be proper vibrations.

[2] The BZ describes the geometrical distribution of the wavevectors in the reciprocal space in the same way the unit cell describes the geometry and periodicity of the crystalline arrangement in the direct space.

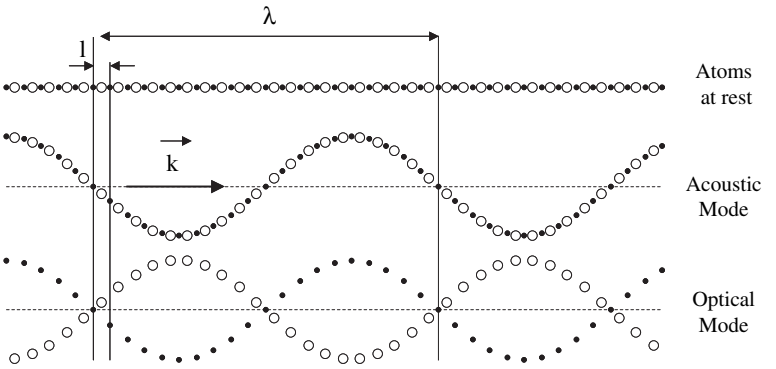

Fig. 1. The transverse phonons ($\|\vec{k}\| = 2\pi/\lambda$) in a 1D-solid with unit cell parameter l.

where $\overline{\overline{\alpha}}$ terms can be individually described as functions of the normal vibration coordinates Q using a Taylor approximation:

$$\alpha_{ij} = \alpha_{ij}^0 + \left(\frac{\partial \alpha_{ij}}{\partial Q}\right)_{Q=Q_0} \times Q \quad (i,j = x,y \text{ or } z) \tag{2}$$

$$P_i = \sum_j \alpha_{ij} \times E_j = \sum_j \left[\alpha_{ij}^0 E_{0_j} \cos(2\pi \nu_{las} t) + \frac{E_{0_j} Q_0}{2} \left(\frac{\partial \alpha_{ij}}{\partial Q}\right)_{Q=Q_0} \times [\cos(2\pi(\nu_{las} - \nu_{vib})t) + \cos(2\pi(\nu_{las} + \nu_{vib})t)] + \cdots \right] \tag{3}$$

With the scattered electric field being proportional to $\vec{P}$, Eq. (3) predicts both quasi-elastic ($\nu \sim \nu_{las}$) and inelastic ($\nu = \nu_{las} \pm \nu_{vib}$) light scattering. The former is called the Rayleigh scattering and the latter, which occurs only if vibrations change polarisability ($\partial \alpha_{ij}/\partial Q \neq 0$), is the Raman scattering [46,47]. Raman spectroscopists normally refer to vibration modes by their wavenumber $\overline{\nu} = \nu_{vib}/c$ (c the light speed, $\overline{\nu}$ in cm^{-1} unit) and the classical electromagnetic theory of radiations from an oscillating dipole demonstrates that Raman peaks have a Lorentzian shape[3]:

$$\mathbf{I}(\overline{\nu}) = \mathbf{I}_0 \times \int_{(BZ)} \frac{d^3\vec{\mathbf{k}}}{[\overline{\nu} - \overline{\nu}(\vec{\mathbf{k}})]^2 + \left(\frac{\Gamma_0}{2}\right)^2} \tag{4}$$

In Eq. (4), $\overline{\nu}(\vec{\mathbf{k}})$ represents the dispersion branch to which the mode belongs and Γ_0 is the half-width for the ordered reference structure.

The scattering of one photon ($\vec{\mathbf{k}} \sim \vec{0}$) by n phonons (wavevectors $\vec{\mathbf{k}}_i$) is governed by the momentum conservation rule:

[3] The experimental bands are a convolution between this natural lineshape, the instrumental transfer function [48,49] and the disorder-induced distribution of vibrators. It is often taken as a Gaussian or a Voigt function (a perfectly symmetric convolution of Lorentzian and Gaussian functions).

$$\sum_{i=1}^{i=n} \vec{\mathbf{k}}_i = \vec{\mathbf{k}}_{\text{scattered}} - \vec{\mathbf{k}}_{\text{incident}} \approx \vec{0} \tag{5}$$

Therefore, only vibrations from the centre of BZ (BZ_c), i.e. long wavelength phonons can be active in any one phonon process (first order spectrum).[4] However, not all BZ_c phonons are active in RS. According to Eq. (3), $\partial\alpha_{ij}/\partial Q$ terms must be different from zero and this condition is governed by the symmetry of the crystals. Raman activity can therefore be predicted through Group Theory [52].

An interesting feature of Eq. (3) is to reveal the dual sensitivity of RS to the electrical (α_{ij}) and mechanical (ν_{vib}) properties of the investigated materials. Two kinds of parameters will therefore influence the spectra:

(i) Parameters acting on the ''mechanics'' like atomic mass, bond strength or the system geometry (interatomic distances, atomic substitutions) will set the peaks' positions (the eigenfrequencies of matter vibrations).
(ii) Parameters acting on the ''charge transfer'' (iono-covalency, band structure, electronic insertion) will set intensity, on the basis of the vibration-induced charge variations occurring at the very bond scale.[5]

As polarisability changes for different kinds of bonds, Raman intensity may not be used to quantitatively determine the amounts of different phases. This limitation can sometimes be an advantage since some secondary phase like an enamel pigment [59–61] or carbon in SiC fibres [38] can be detected in a very small quantity (even traces) and its crystalline structure identified [62]. Elements with high atomic numbers that are situated on the right side of the periodic table (covalent materials in general) are good Raman scatterers whereas ionic structures are difficult to analyse with RS. As for the metals, their surface plasmons limit the penetration of the light. Thus, their Raman signal is extremely weak.[6] There are, however, compounds like the superconducting YBaCuO oxides in which metal atoms produce a strong Raman signal, owing to their covalent bonding along certain directions of the structure [64,65]. Some transition metal ions from the 3*d* (chromium) or 4*f* (lanthanides) groups produce strong fluorescence signals which often mask the Raman spectra but can be used for short range structure [66] and/or residual stress [67] assessment.

[4] It is actually the case in large and flawless crystals. For such materials, inelastic neutron scattering is the only way to explore the BZ [50,51].

[5] The vibration of charged species is somewhat analogous to a high frequency conductivity. There is for instance a direct link between the infrared absorption coefficients $\alpha(\bar{\nu})$ and the conductivity $\sigma(\bar{\nu})$ ([53], [50, pp. 375, 391]):

$$\alpha(\bar{\nu}) = \frac{4\pi}{nc}\sigma(\bar{\nu}) \tag{N1}$$

In Eq. (N1), n is the refraction index and c is the light speed. There is also a formal equivalence between the Raman intensity and $\sigma(\bar{\nu})$ [50, p. 375] but it has rarely been characterized on experimental Raman spectra [55]:

$$I_{\text{Raman}}(\bar{\nu})\alpha\frac{n^{\text{B}}(\bar{\nu})+1}{\bar{\nu}}\sigma(\bar{\nu});\ n^{\text{B}} = \text{Bose occupation factor} \tag{N2}$$

The presence of mobile charge carriers in ionic conductors can be revealed by a temperature dependence of the intensity of the Raman bands [55,56]. Thorough discussions on ionic motions can be found in papers by Funke et al. [57,58].

[6] Hexagonal close-packed metals like Be are an exception [63].

2.3. Conventional Raman spectrometers

Fig. 2a shows the principle of a Raman spectrometer. Up-to-date equipment would include holographic gratings, for improved excitation light rejection, a set of monochromators and a liquid nitrogen- or Peltier effect-cooled CCD mosaic for detection [46,68]. The laser source is often built-in but light coming from an external excitation source can also be used. In the "macro"-configuration, the beam section is $\sim 1\,mm^2$ but the laser spot can be reduced to $\sim 1\,\mu m$ diameter by using the high-magnification microscope objectives which most commercial Raman spectrometers are equipped with. This technique is known as micro-Raman Spectroscopy (μRS). The main additional options are motorized stages for XY(Z) mappings and optical fibre plugs for connection to remote optical heads equipped with microscope objectives [69].

Raman maps are images generated from spectra recorded at discrete points of the sample (the recording is automated). They show the variation of any fitted parameter (i.e. intensity, width or position of one band) as a function of the point of analysis. If the mapping is regular and sufficiently tight, one gets a "smart map" of the parameter (colour or contrast scaling) superimposed with the optical image of the probed area (see Fig. 14b) [39]. Raman parameters can thus be correlated with the crossover from one specific region (phase) to another.

Raman mapping is not to be mistaken for direct *Raman imaging* where a large area of the sample is probed all at once and no fitting is required. More precisely, only photons from a narrow spectral domain are sent to the CCD mosaic and each pixel receives those coming from a given area of the sample. The intensity of the signal thus reveals the presence and location of any substance with a strong Raman signal in the selected spectral window. This is used by customs services to search for drugs hidden in permissible powders like sugar [70].

2.4. Lateral and "in-depth" resolution of conventional μRS

Owing to the diffraction of light, the intensity coming from a point observed through a microscope is distributed over an "Airy disk". The lateral resolution R, which is the smallest distance between two points to still appear distinctively on the microscope image, is half the width of the Airy disks. According to the Rayleigh criterion [71]:

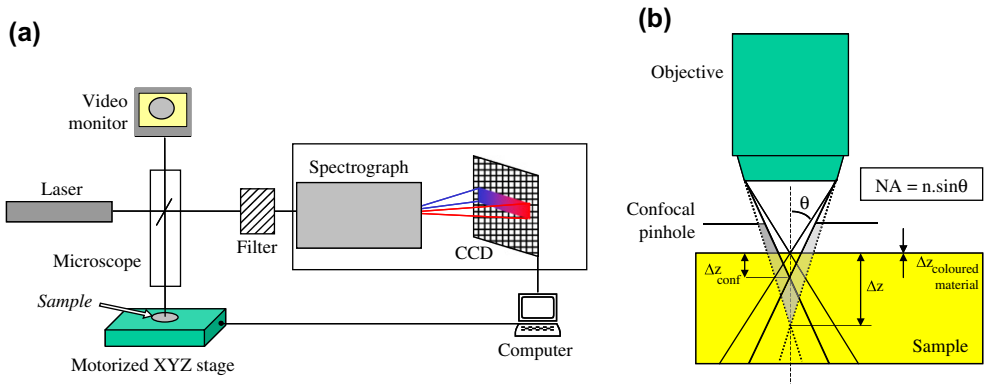

Fig. 2. (a) Principle of a conventional micro-Raman spectrometer. (b) Observation of a sample through a microscope (NA, Numerical Aperture; n, the refractive index of the medium separating the objective from the sample). A confocal hole rejects the shadowed light and facilitates a more accurate in-depth analysis ($\Delta z_{conf} < \Delta z$).

$$R = \frac{0.61 \times \lambda}{\mathrm{NA}} \tag{6}$$

In Eq. (6), λ is the light wavelength and NA represents the numerical aperture (see Fig. 2-b). As for the axial resolution (Δz) of μRS, an estimate is given by the depth of field, which is defined as half the width of the axial intensity profile. Born and Wolf [72] came up with a famous analytical expression for Δz, which is well approximated by a simpler expression by Conrady [73]:

$$\Delta z = \frac{\lambda}{n \sin^2 \theta} \Rightarrow \Delta z_{\text{through air } (n=1)} = \frac{\lambda}{\mathrm{NA}^2} \tag{7}$$

Under "standard" conditions ($n = 1$, $\lambda = 500$ nm, NA = 0.5), the typical lateral and in-depth resolutions of μRS are about 1 and 2 μm, respectively. Even with the smallest visible wavelength (~400 nm) and the highest numerical apertures (oil immersion objectives with $n = 1.515$; NA ~ 1.4), one should not expect a lateral resolution better than $R = 0.2$ μm (the Abbé criterion states that the wave nature of light prevents the distinction of points closer than $\lambda/2$) and a field depth below $\Delta z = 0.4$ μm [74].

However, if a series of spectra are recorded at very close equidistant locations (X–Y stages commonly have a displacement resolution of one-tenth of a micron), a reduced "effective" spot size is obtained through a convolution of the spot profile with the displacement step (see Fig. 3 generated after a Rayleigh scattering mapping procedure; similar conclusions would apply to Raman images). Even then, there is still a high number of "nano-sources" contributing to the Raman signal.

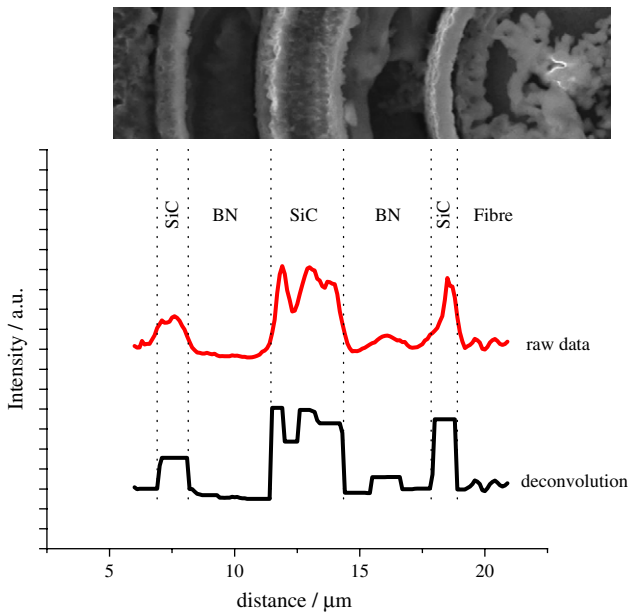

Fig. 3. The intensity profile obtained from a step by step Rayleigh mapping of a multilayered SiC/BN coating deposited on a Hi-Nicalon fibre ($\lambda = 632.8$ nm, Obj. × 100 Olympus MSPlan ULND, NA = 0.80) can be deconvoluted by a function (shown in Ref. [75]) characterizing the distribution of energy in the spot (adapted from Ref. [39, pp. 8–16]).

2.5. Resonant Raman Spectroscopy (RRS)

If the energy of the laser excitation (usually in the UV-nIR range) is high enough to approach those of the various electronic states of the material (in other words if the material is coloured), Raman spectra may be mingled with photoluminescence spectra arising from excited electronic levels. The consequence is the strong enhancement of some vibrational modes (near-resonance/resonance Raman scattering) but one should notice that the probed chemical bonds are in a markedly disturbed state [22,26,27,76–78]. The light penetration is reduced to a few tens of nanometers only ($\Delta z_{\text{coloured}}$ in Fig. 2b), which makes μRS a good method for surface analysis [23,79].[7] If films or fibre-reinforced composites made of absorbent materials are polished with surface to growth direction and surface to fibre axis angles slightly different from, respectively, 90° and 0°, then in-line scans of the samples provide high spatial resolution across the film thickness [83–85] or the fibre–matrix contact region (interphase) [22].

The penetration depth δ of the light is directly related to the wavelength-dependent coefficient of linear absorption a_l (cm^{-1}):

$$\delta = \frac{\lambda_{\text{excitation}}}{4\pi nk} = \frac{1}{a_l(\lambda)} \tag{8}$$

In Eq. (8), n and k are, respectively, the refraction and extinction indexes. The penetration depth δ is indeterminate in the (frequent) lack of absorption coefficients but switching excitation wavelengths close to the electronic absorption threshold can help separate surface from bulk Raman contributions [37]. This is illustrated in Fig. 4, where polyaniline fibres spectra recorded with red, green and blue laser lines, are compared [86]. The bottom spectrum corresponds to the surface of these fibres (maximum electronic absorption) where a ''type I'' monoclinic form of polyaniline is dominant [87]. By contrast, the bulk of the fibre (as seen with blue excitation on the top spectrum) contains more of the type II orthorhombic form. Following the same principle, Shen and Pollak [49] and Yakimova et al. [48] used multiple laser lines to measure spectra at different depths below the surface of semiconductor films.

Note that when the absorption is very high, the temperature may rise at the point of laser impact, even for a few $\mu W/\mu m^2$ irradiation. This effect is reduced if the sample is either dispersed in a non-absorbing matrix, put in a rotating cell or observed in a low temperature cryostat but often results in a wavenumber shift or even a chemical degradation of the sample (oxidation, decomposition, etc.). It is then mandatory to calibrate the thermal effects [88–90]. Besides, whenever the absorbing phase is not dispersed in a transparent matrix, a significant part of the scattered light intensity may be reabsorbed.

2.6. Analysis of ''isolated'' units: the molecular scheme

Eq. (4) corresponds to a description where the vibrations in the solids are pictured as collective waves but another description is possible for solids with different bond strengths. In this ''molecular'' description, clusters of strong covalent bonds are isolated from one another by weaker ionic bonds and, thus, become the relevant vibrational unit (localized vibrations). All atoms from this unit must exclusively belong to it (including, for example, oxygen atoms from polymerised

[7] Resonance Raman spectra recorded with different wavelengths of excitation are also a way of characterizing excitons and polarons in semiconductors [80,81] and conducting polymers [82].

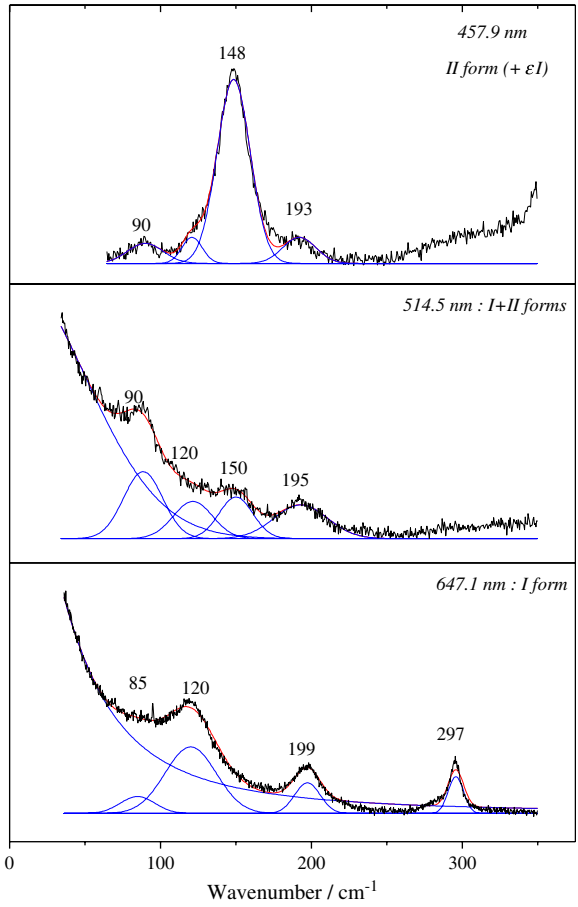

Fig. 4. Raman spectra recorded on polyaniline/camphor sulfonic acid fibres. The use of three different excitation wavelengths modifies the probing depth (Adapted from Ref. [86, pp. 215–220]).

oxides) for the normal coordinates of Eqs. (2) and (3) to coincide with given bond lengths and bond angles. The spectra then reveal stretching and bending modes equivalent to those of polyhedral (mostly tetrahedral or octahedral) isolated molecules [91–94]. The difference arises from the cations generating T′ (translational) and R′ (rotational) libration modes. The molecular scheme not only describes most organic polymers but also crystalline/amorphous inorganic polymers such as silicates, phosphates, niobiates, titanates [95–97] and all compounds with polyatomic cations such as NH_4^+, H_3O^+ or $N_2H_5^{2+}$ [50, p. 379]. A given vibration then always appears in the same region, its exact position giving information about the local environment of the corresponding bonds, both in the crystalline and amorphous states [93,98–103]. Yet, these bonds are probed with a 1 μm^2 section beam, which means one gets only an average view over their distribution.

2.7. *''Nano-specific'' modes*

There are two ways of truly isolating the Raman signal coming from nano-particles. One is by having a nano-particle to be the only one of its kind in the laser's path (SERS) while the other involves a breaking of the $\lambda/2$ diffraction limit of optical microscopes (nano-Raman).

2.7.1. Surface-Enhanced Raman Spectroscopy (SERS)

The Raman signal may be amplified by several orders of magnitude for molecules adsorbed on roughened surfaces [104,105], colloid particles [106] and nanowires [107] of transition metals (mostly silver). This technique is called Surface-Enhanced Raman Spectroscopy (SERS) and the amplification results from the interaction between the electromagnetic field of the laser excitation and the surface plasmon of the metal. This enhancement may be so high that a signal can be recorded with just one or a few particles being probed simultaneously. Unfortunately, getting the right conditions for SERS requires much sample preparation and additional measurements are often necessary to interpret the SERS data collected [106,108]. SERS is seldom applied to solid films [109] and is mainly used in biology, where ''molecules'' must be sufficiently diluted to enable a tracking of their interactions (e.g. a protein with its ''Redox'' partner [110]). Roy et al. [111,112] used SERS for a specific study of the surface carbon in Hot Filament CVD carbon. Azoulay et al. [113] also demonstrated the possibility of selecting single wall carbon nanotubes by SERS.

2.7.2. Nano-Raman

In Near-Field Scanning Optical Microscopy (NSOM in the US; SNOM in Europe), the $\lambda/2$ diffraction limit of optical microscopes (Abbé criterion) is surpassed thanks to the addition of a small aperture made at the end of a tapered probe, frequently a metal-coated optical fibre tip. This confines the optical field and thus imposes the lateral resolution [114]. The probe must be kept extremely close to the sample using micro-manipulation tools borrowed from Atomic Force and Scanning Tunneling Microscopes (AFM/STM) and the technique becomes NSOM-Raman or, simply, ''nano-Raman'', when an NSOM equipment is coupled with a Raman spectrometer [115–123]. Even under the most favourable operating conditions, the excitation is reduced by the optical fibre cut-off and only a faint signal is collected from the small volume that is excited. This is why nano-Raman proved to be efficient only with very good Raman scatterers [119,120,122]. More recently, SERS capability was implemented on nano-Raman equipments by the addition of a vibrating apertureless metallic tip brought close to the surface of the sample [124–127]. This is called Tip Enhanced Raman Spectroscopy (TERS). The intensity enhancement varies in d^{-12} (d being the probe-sample spacing) [128] and getting a good TERS signal is thus far from trivial.

SERS and nano-Raman will not be further discussed in this review. The focus shall instead be placed on the nano-related information that can be retrieved using conventional micro-Raman spectrometers that have nowadays become standard in a number of research and industrial laboratories, owing to the availability of convenient commercial instruments.

3. The vibrational spectra of nanomaterials

The translational symmetry of crystalline materials is broken at grain boundaries, which results in the appearance of specific surface and interface vibrational contributions [129]. Besides, the outer atomic layers of the grains often react with neighbouring species (lattice reconstruction, passivation/corrosion layers, contamination) and experience steep thermo-chemical gradients during processing, which generates new phases, with their own spectral contributions. These two factors are often neglected in RS but we can expect them to become very significant in nano-crystals, where the concentration of grain boundaries is very high.

3.1. Phase identification and phase transitions in nanoparticles

In many nanomaterials, the Raman spectrum remains sufficiently similar to that of the corresponding single crystal to facilitate direct identification of the phases [28,32,129–145]. Once the Raman spectra are known, phase transitions can be characterized (transition temperature, transition pressure, transition order) through mode variation, much the same way as in bulk materials [92,137,146–158]. Besides, the observation of any theoretically forbidden mode is a very sensitive probe of lattice distortions [131,159].

Barborini et al. [157] showed with RS that the structure of gas phase-deposited TiO_2 clusters turned from rutile to anatase whenever they reached 5 nm in diameter. A difference in surface energy usually plays a determinant role in such a phenomenon, as proposed a long time ago by Garvie [160] for zirconia. Similarly, Fray and Payne [158] showed how the temperature of the orthorhombic-tetragonal phase transition of $BaTiO_3$ ceramics depends on the grain size.

3.2. Analysis of amorphous nanodomains

Micro-Raman Spectroscopy is sometimes more powerful than X-ray analysis for detecting and monitoring crystallisation/amorphisation processes in covalent materials [92,100,146,161–164]. Of course, both crystallographers and Raman spectroscopists characterize disorder through peak broadening. Yet, while a loss of long distance translational periodicity (of high atomic number atoms) is always associated with broadening for diffraction patterns, only lattice and librational (R′, T′) modes are sensitive to the same ''long distance'' disorder in RS [165]. The width of the other Raman modes is mainly sensitive to the ''local'' crystal field, more specifically to the short range order in the first (0.1–0.5 nm) and second (0.5–5 nm) atomic shells. If the ''molecular'' description of vibrations applies (see Section 2.6), then Raman bending modes are even specifically sensitive to local geometric disorientation and Raman stretching modes to the neighbouring disorder (particularly atoms from other sublattices or electric defects resulting from substitutions/vacancies).

In fact, diffraction discriminates ''periodical'' domains from ''disordered'' ones but does not easily differentiate clear-cut separations in the real space and progressive orientational disorders (para-crystal), especially in strongly covalent structures such as organic and inorganic polymers [166, p. 615–620]. In materials, mainly polymers, which present interlocking submicronic ''crystalline'' and ''amorphous'' conformational domains [167–174], the distinction is sometimes possible using μRS. The simplest way to picture the problem is to fit lattice modes with two components, one representing the amorphous state and the other the crystalline state. The area ratio of the two underlying areas yields a good estimate of the crystallinity [175,176]. Fig. 5 illustrates this point with a spectrum of the polyamide 6.6 fibre. The polarization analysis clearly shows the orientational effect of straining (fibre extrusion) on the nanocrystals whereas the specific analysis of the low frequency components, which show the collective chain movements, facilitates the separate analysis of the amorphous (wide Gaussian band) and crystalline (narrow Lorentzian) phases. These results were used to demonstrate that the mechanical fatigue of the fibres results from the progressive transformation of the amorphous phase [169,170,172]. Nanophase separation was also investigated in glasses where the connectivity of constitutive polyhedra sets the wavenumbers [177]. Some bands could be attributed to definite clusters in comparison with the experimental spectra of reference crystalline phases [177] or first principle Density Functional Theory (DFT) calculations [94,178].

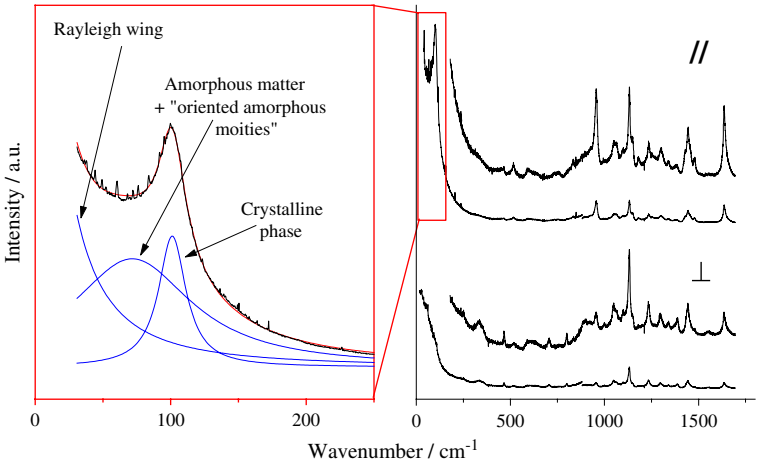

Fig. 5. Low wavenumber Raman spectra of the PA 66 polyamide fibre (FUHP grade, Rhodia) recorded with the exciting electric field polarized either parallel (//) or perpendicular (⊥) to the fibre axis ($\lambda_{exc} = 514.5$ nm) [171]. The collective mode at $\sim 100\ cm^{-1}$ is highly polarized. The zoom shows how the crystalline and amorphous (much wider) contributions can be analysed separately [169].

3.3. Size determination in nanomaterials

Two models are widely used to derive particle size from Raman spectra. The Phonon Confinement Model (PCM) projects Raman "inactive" bulk modes onto the BZ_c whereas the Elastic Sphere Model (ESM) describes the free oscillations of homogeneous spheres.

3.3.1. The Phonon Confinement Model (PCM)

Richter et al. [179] proposed a very intuitive Phonon Confinement Model (PCM) for the phonons in nanospheres of diameter L. They simply multiplied the plane wave describing a phonon, with wavevector $\vec{\mathbf{k}}_0$ (in a perfect crystal $\Phi(\vec{\mathbf{k}}_0, \vec{\mathbf{r}}) = u(\vec{\mathbf{k}}_0, \vec{\mathbf{r}})e^{i\vec{\mathbf{k}}_0 \cdot \vec{\mathbf{r}}}$, u having the same spatial periodicity as the lattice) by a Gaussian function:

$$\Phi(\vec{\mathbf{k}}_0, \vec{\mathbf{r}}) = e^{-\alpha\left(\frac{r}{L}\right)^2} \times u(\vec{\mathbf{k}}_0, \vec{\mathbf{r}})e^{i\vec{\mathbf{k}}_0 \cdot \vec{\mathbf{r}}} \tag{9}$$

Assuming $u(\vec{\mathbf{k}}_0, \vec{\mathbf{r}}) \sim u(\vec{\mathbf{r}})$ and using FT to refer to Fourier Transforms, Eq. (9) is equivalent to:

$$\Phi(\vec{\mathbf{k}}_0, \vec{\mathbf{r}}) \propto \mathrm{FT}^{-1}\left[\mathrm{FT}\left(e^{-\alpha\left(\frac{r}{L}\right)^2} \times e^{i\vec{\mathbf{k}}_0 \cdot \vec{\mathbf{r}}}\right)\right] = \int d^3\,\vec{\mathbf{k}}\, C(\vec{\mathbf{k}}_0, \vec{\mathbf{k}}) \cdot e^{i\vec{\mathbf{k}} \cdot \vec{\mathbf{r}}} \tag{10}$$

$$\text{with} \quad C(\vec{\mathbf{k}}_0, \vec{\mathbf{k}}) = \frac{1}{(2\pi)^3} \int d^3\vec{\mathbf{r}}\left(e^{-\alpha\left(\frac{r}{L}\right)^2} e^{i(\vec{\mathbf{k}}_0 - \vec{\mathbf{k}})\vec{\mathbf{r}}}\right) \tag{11}$$

Thus, the wave associated with a phonon confined in an imperfect crystal simply is a superposition of plane waves with $|C(\vec{\mathbf{k}}_0, \vec{\mathbf{k}})|^2$ weight. Recalling that each wave gives rise to a Lorentzian (Eq. (4)), the total Raman intensity is eventually given by:

$$I(\overline{\nu})\alpha\int_{\mathrm{BZ}}\mathrm{d}^3\vec{\mathbf{k}}\frac{|C(\vec{\mathbf{k}}_0,\vec{\mathbf{k}})|^2}{[\overline{\nu}-\overline{\nu}(\vec{\mathbf{k}})]^2+\left(\frac{\Gamma_0}{2}\right)^2} \tag{12}$$

Eq. (12) mathematically expresses the Raman selection rule breaking induced by phonon confinement[8] with a weighed exploration of the dispersion curves. Taking $\mathbf{k}_{\mathrm{BZe}}$ as the edge of BZ, $\mathbf{q}$ as the reduced wavevector ($\mathbf{q}=\mathbf{k}/\mathbf{k}_{\mathrm{BZe}}$) and assuming isotropic mode dispersion [180], Eq. (12) yields:

$$I(\overline{\nu})\alpha\int_{\mathbf{q}=0}^{\mathbf{q}=1}\mathrm{d}\mathbf{q}\mathrm{e}^{-\frac{k_{\mathrm{BZe}}^2(\mathbf{q}-\mathbf{q}_0)^2L^2}{2\alpha}}\times\frac{1}{[\overline{\nu}-\overline{\nu}(\mathbf{q})]^2+\left(\frac{\Gamma_0}{2}\right)^2} \tag{13}$$

This is the equation to which most authors refer when using the PCM [179–186].[9] For semiconductor Quantum Dots (QDs), NanoWires (NWs) or slabs, the PCM is easily adapted using the appropriate expressions for the $\mathrm{d}^3\vec{\mathbf{k}}$ integration volume in Eq. (12) [189–193].[10] Knowledge of the Vibrational Density of States (VDOS) is required for computing Eq. (13). It may be obtained either from neutron scattering measurements, from data on parent structures or from *ab initio* calculations based on a rigid-model structure [182,183,195–197]. The PCM, which does not apply to the acoustic modes because their energy is nil at BZc is very seldom used for the TO modes on account of their low dispersion [192,198]. It is almost exclusively applied to the LO modes. With LO wavenumbers usually being maximum at BZc, the integration in Eq. (13) introduces additional contributions on the low frequency side of the single crystal mode and the resulting peaks become asymmetric. Peak adjustment is not always mandatory once phonon confinement has been invoked. In first approximation, the peak shift is indeed proportional to the inverse of the grain size [187,199]. The overall half-width at half-height also is proportional to the inverse of the grain size, as was reported for nanocrystalline CeO_2 [196,197] (see Fig. 6) or boron nitride [187] and can be verified with data on Ge [184].

In the paper introducing the PCM, Richter et al. [179] assumed $\alpha=2$. Campbell and Fauchet [193] later tested several forms for the weighing function introduced in Eq. (9). They came to

[8] As a consequence of Heisenberg's principle, the uncertainty $\Delta k=\Delta p/\hbar$ on the wavevector must remain above or equal to $(2L)^{-1}$.

[9] Based on the triple hypothesis that modes from different crystallites are uncorrelated, that lifetimes can be simulated with a Lorentzian broadening (Γ_0) and that susceptibility variations ($\Delta\chi$) are proportional to the normal vibration coordinates, Nemanich et al. [187] predicted the Raman intensity on probing of N orthorhombic crystallites to be:

$$I(\overline{\nu})\alpha S(\vec{\mathbf{k}}_0,\overline{\nu})=\frac{N}{c^2V^2}\left(\frac{n^{\mathrm{B}}(\overline{\nu})+1}{\overline{\nu}}\right)V^{-1}\sum_{\vec{\mathbf{k}}_j}C\left(\vec{\mathbf{k}},\overline{\nu}_j(\vec{\mathbf{k}})\right)|F(\vec{\mathbf{k}}-\vec{\mathbf{k}}_0)|^2\times\frac{\Gamma_0/4\pi}{\left[\overline{\nu}-\overline{\nu}_j(\vec{\mathbf{k}})\right]^2+\left(\Gamma_0^2/4\right)} \tag{N3}$$

In this equation, S is the Fourier transform of polarisability variations associated with Raman scattering, $(n^{\mathrm{B}}(\overline{\nu})+1)$ is the Bose population factor ($n^{\mathrm{B}}(\overline{\nu})=1/(\mathrm{e}^{h\nu/kT}-1)$), C is the Raman coupling coefficient for branch j and $|F(k-k_0)|^2$ is the uncertainty on the wavevector induced by phonon confinement [187,188]. This approach is entirely equivalent to the PCM if the F function is assumed to be Gaussian and the occupation term is neglected (this simplification is justified only when a single band is modelled).

[10] Note that the PCM failed to predict the Raman shift in silicon spherical or columnar nanocrystals. Zi et al. [194] showed with a Bond Polarisability Modelling that it could rather be predicted using the following expression:

$$\overline{\nu}_{\mathrm{vib}}=\overline{\nu}_{\mathrm{bulk}}-A\left(\frac{a}{L}\right)^{\gamma} \tag{N4}$$

In Eq. (N4), a is the lattice constant whereas A and γ fully characterize the nanocrystal geometry.

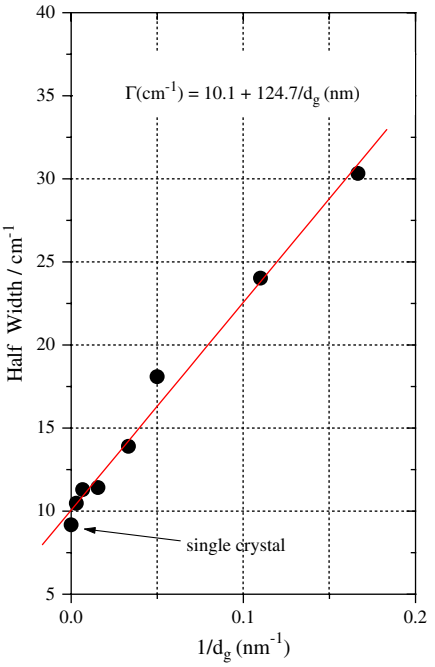

Fig. 6. The half-width at half height of the CeO_2 Raman band at 466 cm^{-1} plotted as the inverse of the grain size obtained by X-ray diffraction. Reprinted from Ref. [196, pp. 99–105] with permission from Elsevier.

acknowledge the choice of a Gaussian form but chose the more confining parameter $\alpha = 8\pi^2$ first proposed by Tiong et al. [198], which corresponds to a rigid confinement hypothesis ($|C(\vec{\mathbf{k}}_0, \vec{\mathbf{k}})|^2 = 0$ for $r = L/2$) [180,183,185,197,200]. A bond polarisability modelling of vibrations in silicon nanocrystals also returned a value of 9.67 for α [201]. As a matter of fact, α may be considered, with L, as an adjustment variable of the model [184]. Besides, L should not systematically identify with the grain size. Phonons can indeed be confined by any "spatially limiting" feature in the grain (twins, stacking faults, inclusions, vacancies, boundaries, pores, etc.). L is therefore equal to $2\pi/\Delta k$, where Δk is the extension of BZ domain of which the modes are activated. It is nothing but a coherence length which may correspond to an actual grain size [179,191,202–205] but also to defects/impurities interspacing [185,196,200,206,207] or the size of cation-ordered domains in incommensurate phases [91], undamaged crystalline domains in ion-implanted GaAs [198], polytypic domains (see Fig. 16 and associated comments) [181,208,209] or clusters in semiconducting alloys [182,183,210] and ferroelectrics [12]. The physical interpretation of L therefore is a key element. For instance, Weber thought it was the grain size in CeO_2 but found an order of magnitude discrepancy with results from electronic microscopy [197]. In fact, Kosacki et al. [196] showed L was the distance between defects in the oxygen lattice of ceria (see Fig. 18b and attached comments). Carles et al. [180] showed that the meaning of L could even change for germanium particles depending on their size: L corresponds to the actual size for the bigger grains, but represents the domain size in smaller grains where alloying has taken place.

Although Richter et al. took $\vec{\mathbf{k}}_0$ at the BZc, their model did not preclude it from standing somewhere else (which many authors have forgotten). Adding this degree of freedom to the

model finds a physical justification in at least two situations. First, when nanoparticles are surrounded by a parent material, the phonons can be reflected at grain boundaries and their interferences can "activate" modes away from BZc. This effect was mentioned by Arora et al. [211] for CVD-diamond particles embedded in amorphous carbon. They fitted the spectra with as many as 20 contributions calculated with Eq. (13) at specific values of $\vec{\mathbf{k}}_0 \neq \vec{0}$. Second, in their "Random Stacking Fault" model of disorder in silicon carbide, Rohmfeld et al. [181,208] used a Bond Polarisability Model (BPM) to calculate the influence of stacking defects occurring with ΔL interspacing. They concluded to the extinction of BZc modes to the benefit of modes with wavevectors equal to $\mathbf{k}_m = (2m+1)\pi/\Delta L$; $m = 0,1,2\ldots$ which is analogous to the application of Eq. (13) at $\mathbf{k}_m$ points. Even though disorder and nanometric dimension effects often participate simultaneously to phonon confinement, their relative contributions can theoretically be separated whenever $\vec{\mathbf{k}}_0$ is allowed to vary:

- Disorder will disturb the short range order and fold the BZ. $\vec{\mathbf{k}}_0$ will be away from BZc and L should then be inversely proportional to the density of defects.
- If the confinement results from the existence of domains in which order is perfect, typically nanocrystals, then the activated modes should be centred in Γ ($\vec{\mathbf{k}}_0 = \vec{0}$) and L will represent the grain size.

In Ref. [179], Richter et al. attributed the Raman signal not accounted for by the PCM to fully amorphous matter (they actually worked on microcrystalline silicon). This explanation was later used by several authors [191,200,212–214] but should not hide the fact that the PCM is based on approximations and neglects some peculiarities of vibrations in nanomaterials.

(i) *The PCM supposes isotropy*: as is, the PCM only applies to materials with homogeneous structure in all directions of space (spherical model). An "isotropic dispersion hypothesis" is probably acceptable for almost any material in the limit of $\vec{\mathbf{k}}_0$ close to BZc [184] but integrating Eq. (13) along the main directions of the BZ returns more satisfactory results [215]. Carles et al. [180] proposed a simple way of taking anisotropy into account: all directions are plotted on the same reduced wavevector axis and the wavenumbers are simply averaged. As for Γ_0, it is adjusted by means of an anisotropy parameter based on the maximum branch "splitting" observed between different directions.

(ii) *The PCM supposes uniform size and shape*: another approximation is made with the PCM when a Gaussian weighing function is introduced in Eq. (9). This assumes all crystallites have the same shape – either spherical [181] or orthorhombic [187] – and size, whereas the actual distributions must be taken into account in a model describing reality [184,192,202,216,217].

(iii) *The PCM neglects surface/interface phonons*: the PCM progressively loses its relevance when the particle size decreases and the surface [218–224]/interface [219,225] modes (which it does not account for) become preponderant in the signal. Richter et al. [179] were aware of this limitation when they proposed the PCM and Roy and Sood [222] simultaneously considered confined bulk modes (PCM description) and surface phonons in CdS/CdSe nanoparticles embedded in glass matrix. The surface modes in ionic crystals become important below $\sim$100 nm [226,227] but can be predicted using a "Dielectric Continuum Approach" (DCA). Surface Optical modes (SO) are expected at wavenumbers $\overline{\nu}_{SO}$ in the intermediate region between the TO and LO modes, whose splitting is

a consequence of the long range Coulomb interaction. In spherical crystals of Blende type semiconductors [223,226,228]:

$$\overline{\nu}_{SO} = \sqrt{\frac{\frac{\ell+1}{\ell}\overline{\nu}_{TO}^2 + \frac{\varepsilon_\infty}{\varepsilon_M}\overline{\nu}_{LO}^2}{\frac{\ell+1}{\ell} + \frac{\varepsilon_\infty}{\varepsilon_M}}} \tag{14}$$

In Eq. (14), $\ell = 1, 2, 3, \ldots$, ε_∞ is the high frequency dielectric constant of the semiconductor and ε_M is the frequency-independent dielectric constant of the surrounding medium. The radial dependence of the surface modes is in the $r^{\ell-1}$ form and only the $\ell = 1$ surface mode (the so-called Fröhlich mode), with its constant amplitude, is thus expected to make a significant contribution. Surface optical modes were similarly described for semiconductors of the Wurtzite type [225] and metals [229]. Surface/interface modes for the specific geometries of nanocylinders and nanowires [221], spherically capped QDs/Quantum Wells (QWs) [230] and Multiple QWs (MQWs) [231,232] have also been addressed.

(iv) *The confinement function has limited physical meaning*: most criticisms formulated against the PCM concerned the arbitrariness of the confinement function. As a matter of fact, the PCM only is a phenomenological tool and even its best advocates acknowledge it cannot be expected to fully account for the lineshape when it relies on propagating phonons (''bulk'' dispersion curves) to describe confined modes. Alternative and more ''physical'' descriptions of the optical modes confined in nanocrystals were mostly proposed by semiconductor specialists. First, it was predicted [233] and confirmed experimentally for PbS [234] that the TO and LO modes are coupled in nanocrystals. Besides, the dipoles generated in polar semiconductors by optical vibrations generate electromagnetic fields and thus may interact with electrons (polarons) or electron–hole pairs (excitons). This so-called Fröhlich interaction is weak in single crystals but leads to strong resonances of the LO and SO modes in confined semiconductors: quantum dots, wires and superlattices [195,219,223,233,235–239]). Pusep et al. [240] tried to adapt the PCM to the electron–LO coupling in doped semiconductors but an accurate description would require a continuous approach like the one proposed by Roca et al. [233], later improved by Vasilevskiy et al. [241]. Note that in conducting/coloured nanomaterials (carbon, conducting polymers, etc.) and superlattices, an additional Fano coupling is possible between the continuum of electronic states and the discrete energy levels of the phonons [211,242–245].

3.3.2. The Elastic Sphere Model (ESM)

The use of bulk dispersion curves is questionable when there is a lot of reduction in particle size [9,237]. Meyer et al. [246] used Molecular Dynamics Simulations to calculate the nanoparticle VDOS and demonstrated the importance of grain boundary-related contributions. An alternative to considering the vibrations as ensuing from a disturbed infinite crystal (what the PCM does) is to adopt a first principle description of vibrations in a free sphere. This problem was theoretically discussed in 1882 by Lamb [247]. A brief description will be given but detailed information can be found elsewhere (with a broad spectrum of notations) [248–250,252,253,255,256].

Imagine a sphere of radius R with vector $\vec{\mathbf{u}}(M,t)$ as the displacement field induced by propagating waves at a given point (M) and for a given time (t). Assuming the sphere is

homogeneous (constant density ρ) and elastic, the elastodynamics theory commands the waves to satisfy the general Navier equation:

$$\ddot{\mathbf{u}} = \left(\frac{\lambda+2\mu}{\rho}\right)\nabla(\nabla\cdot\vec{\mathbf{u}}) - \frac{\mu}{\rho}\nabla\times(\nabla\times\vec{\mathbf{u}}) = v_{\mathrm{L}}^2\nabla(\nabla\cdot\vec{\mathbf{u}}) - v_{\mathrm{T}}^2\nabla\times(\nabla\times\vec{\mathbf{u}})$$
$$= \left(v_{\mathrm{L}}^2 - v_{\mathrm{T}}^2\right)\nabla(\nabla\cdot\vec{\mathbf{u}}) + v_{\mathrm{T}}^2\Delta\vec{\mathbf{u}} \tag{15}$$

In Eq. (15), $\ddot{\mathbf{u}}$ represents the second time derivative of vector $\vec{\mathbf{u}}$, λ and μ are the so-called Lamé coefficients characterizing the bulk mechanical properties[11] while v_{L} and v_{T} are, respectively, the longitudinal and transverse sound propagation velocities. A general law states that two potentials exist with which $\vec{\mathbf{u}}$ can be decomposed into a sum of three components:

$$\Phi = \frac{1}{k_{\mathrm{L}}}\, j_l(k_{\mathrm{L}}r)Y_l^m(\theta,\varphi)\mathrm{e}^{-i\omega t};\ k_{\mathrm{L}} = \frac{2\pi\nu_n}{v_{\mathrm{L}}} \tag{16}$$

$$\psi = \frac{1}{k_{\mathrm{T}}}\, j_1(k_{\mathrm{T}}r)Y_1^m(\theta,\varphi)\mathrm{e}^{-i\omega t};\ k_{\mathrm{T}} = \frac{2\pi\nu_n}{v_{\mathrm{T}}} \tag{17}$$

$$\vec{\mathbf{u}}_1 = \nabla\Phi \tag{18}$$

$$\vec{\mathbf{u}}_2 = \nabla\times\nabla(\vec{\mathbf{r}}\psi) \tag{19}$$

$$\vec{\mathbf{u}}_3 = k_{\mathrm{T}}\nabla\times(\vec{\mathbf{r}}\psi) \tag{20}$$

In Eqs. (16) and (17), j_l are spherical Bessel functions of the first kind and Y_l^m are the usual spherical harmonics. The radial quantum number n indicates the mode order ($n=0$ for surface modes [249,257]) while the orbital quantum number l and its z-axis component m ($-l \le m \le +l$) define the symmetry of the vibrations and the number of nodal surfaces.[12] ϕ governs longitudinal (compressive) waves (P-waves in seismology) whereas Ψ is associated with transverse (shear) waves (S-waves in seismology). For convenience, replace the vector base classically used in problems with spherical symmetry (Fig. 7a) by the following one:

$$\vec{\mathbf{e}}_{lm}(\theta,\varphi) = Y_l^m(\theta,\varphi)\vec{\mathbf{e}}_r \tag{21}$$

$$\vec{\mathbf{n}}_{lm}(\theta,\varphi) = \mathbf{r}\nabla Y_l^m(\theta,\varphi) \tag{22}$$

$$\vec{\mathbf{m}}_{lm}(\theta,\varphi) = \vec{\mathbf{e}}_r\times\vec{\mathbf{n}}_{lm}(\theta,\varphi) \tag{23}$$

In this new base, Eqs. (18)–(20) can be rewritten as follows (the prime indicates differentiation with respect to r):

$$\vec{\mathbf{u}}_1 = j_l'(k_{\mathrm{L}}r)\vec{\mathbf{e}}_{lm}(\theta,\varphi) + \frac{j_l(k_{\mathrm{L}}r)}{k_{\mathrm{L}}r}\vec{\mathbf{n}}_{lm}(\theta,\varphi) \tag{24}$$

[11] They are related to Young's Modulus (E) and Poisson's Ratio (σ) via the following relations:

$$\lambda = \frac{\sigma E}{(1+\sigma)(1-\sigma)};\ \mu = \frac{E}{2(1+\sigma)}$$

[12] Duval et al. [258] added a fourth parameter – the polarization index p – to distinguish the spheroidal modes from the torsional ones (see further).

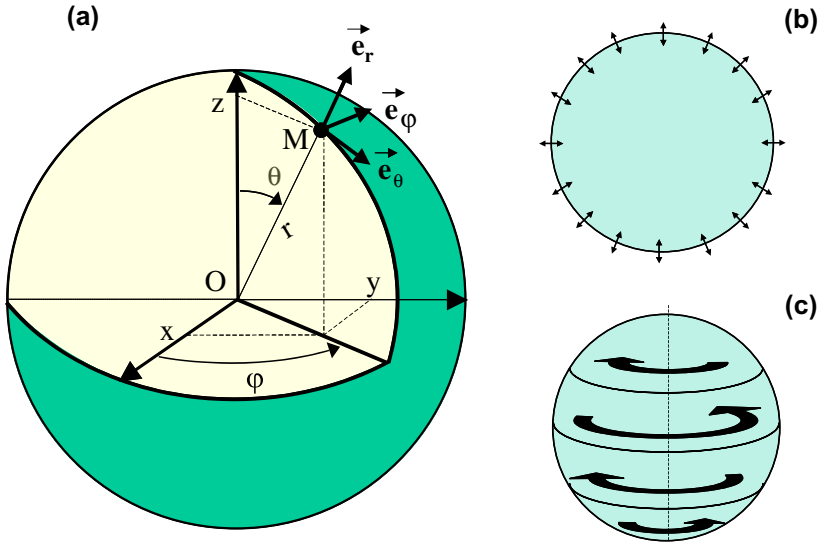

Fig. 7. (a) Description of one nanoparticle in the Elastic Sphere Model (ESM). (b) Oscillation of a free sphere in a single spheroidal mode. (c) Oscillation of a free sphere in a single torsional mode.

$$\vec{\mathbf{u}}_2 = l(l+1)\frac{j_l(k_L r)}{k_L r}\vec{\mathbf{e}}_{lm}(\theta,\varphi) + \left(\frac{j_l(k_L r)}{k_L r} + j_l'(k_L r)\right)\vec{\mathbf{n}}_{lm}(\theta,\varphi) \tag{25}$$

$$\vec{\mathbf{u}}_3 = j_l(k_T r)\vec{\mathbf{m}}_{lm}(\theta,\varphi) \tag{26}$$

A distinction is possible between two families of modes (see Fig. 7b and c):

Modes with purely radial displacement are called spheroidal modes.
Modes with purely tangential displacement, occurring with no volume change, are called torsional modes.

Duval [259] was the first to establish the selection rules for the ESM. Since the modes irreducible representations had to coincide with those of the sphere group, he showed that only purely spherical ($l = 0$; irreducible representation $D_g^{(0)}$) and quadrupolar ($l = 2$; $D_g^{(2)}$) spheroidal modes are Raman active (while all torsional modes are forbidden).[13] Their relative intensity is variable but only the first order "surface" ones ($n = 0$), those shown in Fig. 8, have significant contributions [257,260–262]. Their identification is easy since only $D_g^{(0)}$ is polarized (parallel polarization). An expression for the stress field can be derived from Eqs. (24)–(26) and the subsequent

[13] In group theory, the $D_i^{(l)}$ notation indicates modes of $(2l+1)$ degeneracy with either symmetry ($i = g$) or antisymmetry ($i = u$) with respect to an inversion centre.

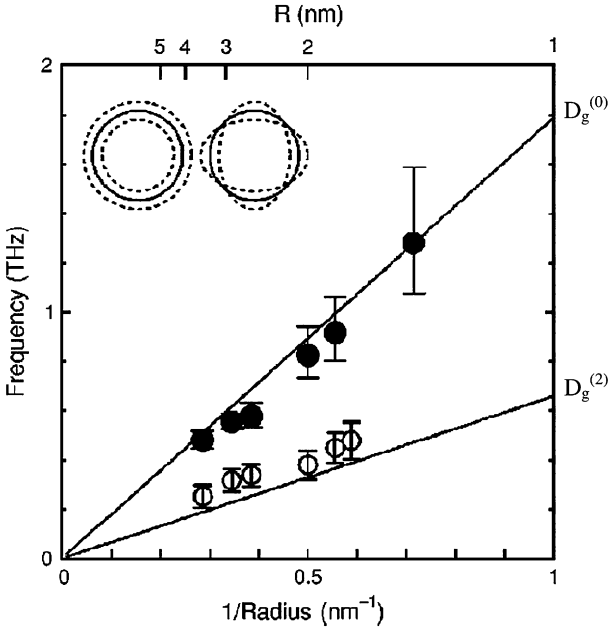

Fig. 8. Size dependence of the $D_g^{(0)}$ and $D_g^{(2)}$ modes in PbSe quantum dots. Reprinted with permission from M. Ikezawa et al. [272]. Copyright 2001 by the American Physical Society.

application of stress-free boundary conditions for $r = R$ eventually yields the vibration eigenfrequencies ν_n.[14] For $l = 0$ spheroidal modes, a good approximation of ν_n is given by [256]:

$$\nu_n = \frac{v_L}{R}\left((n+1)\pi - \arcsin\frac{4}{(n+1)\pi}\left(\frac{v_T}{v_L}\right)^2\right) \tag{27}$$

No analytic solutions can be obtained for the other modes, which have to be calculated numerically, but the wavenumbers are always proportional to R^{-1} (see Fig. 8):

$$R = \frac{A \cdot v_L}{c \cdot \nu_{D_g^{(0)}}} \tag{28}$$

$$R = \frac{A' \cdot v_T}{c \cdot \nu_{D_g^{(2)}}} \tag{29}$$

In Eqs. (28) and (29), c is the light speed in vacuum while A and A' are dimensionless constants. These equations were used to determine the radius of silver clusters in ancient and advanced materials[15] [263–266] or particles size in cordierite [261], TiO_2 [267–269], silicon

[14] Some authors added electromagnetic continuity as a grain boundary condition [233,241].

[15] Most authors only considered Ag^0 [263] but clusters integrating Ag^+ ions are rather expected in a iono-covalent matrix (there are Ag^+ ions at the surface of the clusters formed in oxides fired at high temperatures [4]). Analysis with different excitations should reduce Ag^+ contribution through metallic silver exaltation.

[270,271], PbSe [272], etc. Note that the scattering efficiency scales like ν^{-3} [260]. Consequently, directly applying Eqs. (28) and (29) when there is a size distribution will lead to an overestimation of R average. Besides, the ESM assumes the nanoparticles are homogeneous and only modes with λ much greater than the interatomic distance, mostly the low energy fundamental and first harmonic modes, are described [258]. On account of this restriction, the ESM is often referred to as a predicting model for ''confined acoustic modes'', although optical phonons were occasionally studied using the same model [273].

Just like for the PCM, the use of the ESM for grain size determination comes with certain approximations. Strictly speaking the model applies to equal size, ''free-standing'', isotropic spheres. The triple degeneracy of the $D_g^{(2)}$ mode is lifted for ellipsoidal particles [259,274] and Hernandez-Rosas et al. [275] recently proposed a generalised model for oblate spheroids. Like for the PCM, it is also possible to include the size distribution [217,264,276,277] and the problem of anisotropic materials was discussed by Murray et al. [278]. It had been previously dealt with by Fujii et al. [270] who tried calculations based on the longitudinal and transversal sound velocities for the main crystallographic directions of silicon but they found no agreement with their experimental results.

It has been assumed for a long time that the ESM held in matrices with Lamé coefficients sufficiently different from those of the nanospheres [279,280], but the presence of a matrix also activates a torsional surface mode ($l = 1$) which eventually dominates the spectra [259,269,280]. Moreover, some couplings of the Raman active modes with matrix vibrations can be expected [249–251,255,276,278–281], knowing that the smaller the nanoparticles, the stronger the coupling [250,256]. They were modelled by a ''Complex Frequency Method'' (CFM) [258,278]. If the nanoparticles are in relatively high concentration, which will surely be the case in active devices like QD networks, a collective Fröhlich mode will also contribute to the Raman spectrum [282].

3.3.3. Validity domains of the PCM and the ESM

Fig. 9 illustrates the different approaches to the RS of nanoparticles. In grains much larger than the wavelength, phonons propagate almost in the same way as in perfect ''infinite'' crystals. The only perturbation then comes from vibrations involving the outer atomic layers, which do not meet the bulk conditions [37,79,195]. The structural transition between the surface and the bulk of each grain obviously is progressive but let us assume, for the sake of simplicity, that there is an homogeneous surface shell of definite thickness t. Fig. 9a then shows how the outer shell to bulk volume ratio reaches a critical value for $D/t \sim 5$, where D is the grain diameter. When the grain size further decreases, the confinement of optic modes begins and the PCM starts applying. Soon, the relative proportion of ''non-bulk'' skin and surface modes increases and, below a certain size, the very notion of collective vibrations disappears. As a principle, the ESM must then be considered but there is no clear-cut grain dimension for which one should switch from the PCM to the ESM. They do not necessarily exclude each other and, on occasion, were even used simultaneously [283,284].

(i) The PCM should be applicable between the grain size at which the ''bulk'' dispersion curves lose all significance ($\sim$5 nm [205,237]) and a high-end value where confinement has no effect on the spectrum, which will obviously depend on the mode dispersion around BZc [40,192,196,284]. Note that surface modes add a significant contribution for grain sizes up to 8 nm in SnO_2 [285] and even 20 nm in ZrO_2 [286].

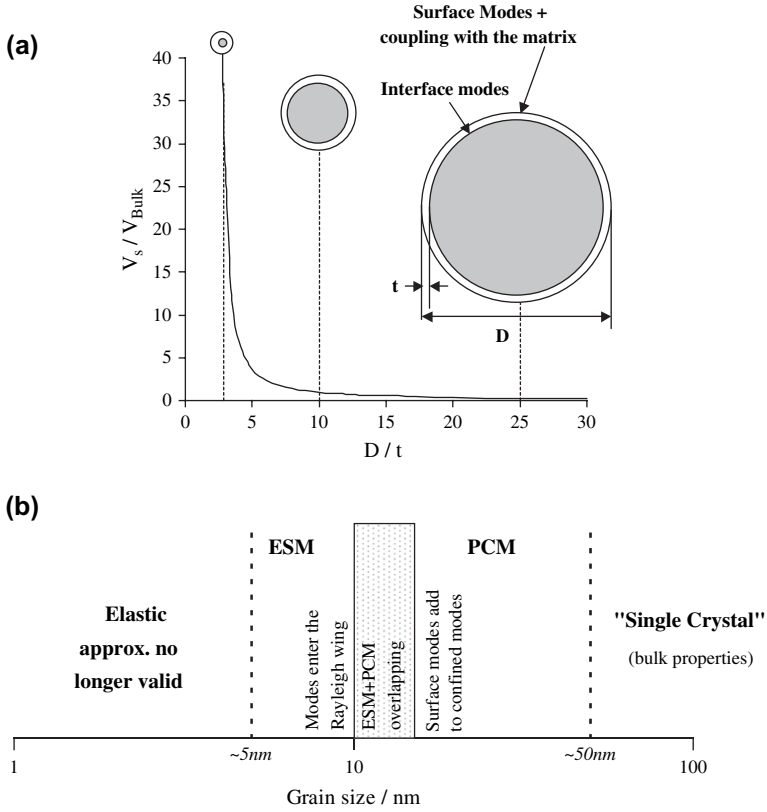

Fig. 9. (a) The ''surface to bulk'' volume ratio in nanospheres of diameter D, with a surface layer of definite thickness t (see text). (b) Applicability range of the different descriptions for the vibrations of spherical crystals (ESM, Elastic Sphere Model; PCM, Phonon Confinement Model). The grain size values are indicative and actual limits depend on the material.

(ii) The typical grain size below which nanocrystals cannot be assumed homogeneous and the ESM therefore no longer applies [249] is between 1 nm [265] and 5 nm [258,284,287], which is in good agreement with the ~40 interatomic distances predicted by Wittmer et al. [288]. Note that if particles with a size slightly above this limit are embedded in a glass phase, the ''so-called'' boson peak of the matrix (see Section 4.1) may hide the oscillations described by the ESM, unless wave-guided spectroscopy is used [265]. There is no theoretical upper limit to ESM applicability but the low frequency modes gradually enter the Rayleigh wing (quasi-elastic diffusion; see Section 2.2) as the grain size increases. Thus ESM becomes irrelevant for a D value that depends on both the material and the experimental resolution of the spectrometer [254,289].

One should not forget that peak altering effects like internal stress[16] [9,184,186,215,216,218,291], growth directionality [80], non-stoichiometry [185], local

[16] Residual stresses are unavoidable, even in free particles (the reduction of the surface atoms coordination number reduces the bond lengths [290]). They were investigated in detail by Gomonnai et al. [218] and Sirenko et al. [9].

heating [189,221,292], couplings or defect-induced diffusions [292] may add to the size effect on the Raman spectra of nanomaterials. The stress will act on the position of the peaks [186], defects (non-stoichiometry for instance) will widen them [185,186,191] and temperature will act on both position and width. Falkovsky and Camassel [293] wrote a short review on the contribution of all kinds of defects to band broadening.

4. Selected case studies

4.1. The structural variety of glass ceramics

Ceramics and glass-ceramics obtained from liquid precursors (molten glass and salts, solutions, gels, organic precursors [1,294–296]) form a large range of nanophased materials. The transition from the liquid to the solid state "freezes" a local steric disorder and thermal annealing is necessary for long distance Coulombian interactions to stabilize the thermodynamically stable crystalline phase. In these materials, strongly covalent species like the SiO_4^{4-} or PO_4^{3-} tetrahedra often experience a site symmetry different from the average one derived from crystallographic studies [296,297]. For instance, Fig. 10a compares the Raman spectrum of a $2GeO_2{-}Al_2O_3{-}2H_2O$ gel prepared through alkoxides hydrolysis–polycondensation with those of the phases obtained after thermal treatment up to 1450 °C [298]. The intermediate $Al_2Ge_2O_7$ phase (stable from 1250 to 1300 °C) has a low symmetry monoclinic structure but fine low frequency Raman peaks, characteristic of an ordered compound, while the bands of crystalline mullite are as broad as those of the glass in spite of a higher symmetry orthorhombic structure. This relates to an orientational disorder induced by oxygen vacancies in the AlO_4 tetrahedra. Moreover, since the occurrence of a broadening indicates distorted entities, it is

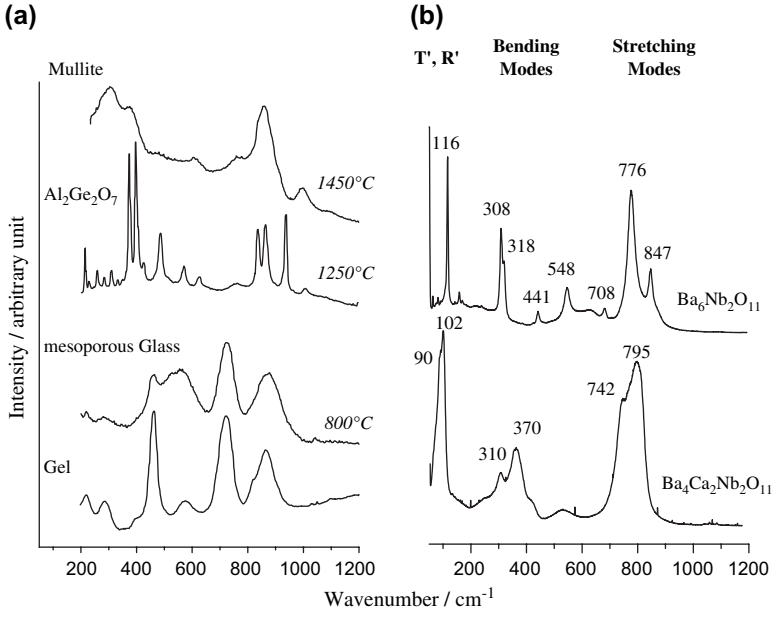

Fig. 10. (a) Germanium mullite in different physical states (adapted from Ref. [298, pp. 161–168]). (b) Perovskite-related barium niobiates (Adapted from Ref. [299, pp. 339–347]).

obvious from the figure that the GeO_4 tetrahedra as well as GeO_6 octahedra are more distorted in the mesoporous glass than in the gel phase [298]. In the example of the perovskite-related niobiates from Fig. 10b, the Nb–O modes around 800 cm^{-1} are split because of the occasional presence of oxygen vacancies in the NbO_6 octahedra. The (T′, R′) modes involving the Ba atoms located at the corners of the unit-cell are not modified by these vacancies in $Ba_6Nb_2O_{11}$ (hence the fine peaks) but are split again in $Ba_4Ca_2Nb_2O_{11}$ because chemical and mass decoupling isolate the Ba and Ca sub-lattices [299]. The same kind of vibrational decoupling due to defects has been observed for many silicates [296,297,300].

Two silicate spectra are shown in Fig. 11a and b. Most types of glass contain nanometric crystallites and the spectrum of silicates (SiO_2 tetrahedral network) is intermediate between that of a disordered network and the superposition of contributions from definite vibrational entities: tetrahedra rings in vitreous silica (the narrow defect bands in Fig. 11a originate from the vibrations of threefold (D_2) and fourfold (D_1) rings [301–304]) and complex arrangements of SiO_4 tetrahedra in alkali/earth-alkali silicates [301]. The deformation ($\delta_{Si-O-Si} \sim 500\ cm^{-1}$) and elongation ($\nu_{Si-O} \sim 800–1200\ cm^{-1}$) modes depend on the connectivity of the SiO_4 tetrahedra and can be fitted with components called Q_n and Q'_n, respectively (n represents the number of Si–O–Si bridges per tetrahedron) [305–307]. The position and area of these components then constitute characteristic parameters of silicate glass nanostructures and can be used for garnering additional information such as the original composition or the sintering temperature [305,306].

The most specific part of glass spectra is a band peaking at ~50 to 100 cm^{-1}, which is called the Boson Peak (BP) because its intensity obeys a Bose–Einstein distribution. Since

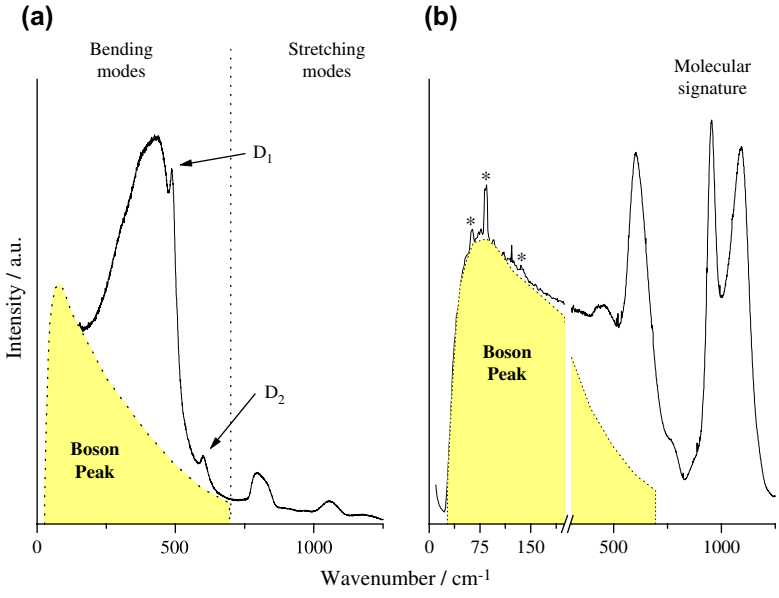

Fig. 11. (a) Raman spectrum of pure glassy silica (macro-configuration, $\lambda = 406$ nm; D_1 and D_2: see text). (b) Raman spectrum of a highly depolymerised potassium-rich calcium silicate stained glass (macro-configuration, $\lambda = 413$ nm; stars indicate plasma lines from the laser).

the F function in Eq. (N3) never becomes 0 in amorphous materials, their VDOS $G(\overline{\nu})$ is fully active and Raman intensity is given by [308][17]:

$$I(\overline{\nu}) = \frac{n^{B}(\overline{\nu}) + 1}{c\overline{\nu}} C(\overline{\nu}) G(\overline{\nu}) \tag{30}$$

The BP mostly originates from the probe-excitation coupling function $C(\overline{\nu})$, the reason why it best shows on $I/[\overline{\nu}(n^{B}(\overline{\nu}) + 1)]$ ''reduced intensity'' curves.[18] There is an ongoing debate to ascertain whether the extra vibrations from the BP correspond to propagating or localized modes but all interpretations make the BP a way of characterizing glasses intermediate range order at the nanometer scale:

(i) Some teams believe that collective acoustical waves are possible in glass, even at very low frequencies, but that the transverse acoustic branch is flattened [309–311]. Yet, $C(\overline{\nu})$ is expected to scale as $\overline{\nu}^2$ for slightly distorted plane-wave vibrations [312] though Surotsev and Sokolov [313] demonstrated experimentally that glasses rather exhibit the following behaviour[19]:

$$C(\overline{\nu}) = A \times \left(\frac{\overline{\nu}}{\overline{\nu}_{BP}} + B \right) \tag{31}$$

(ii) Duval et al. [318] explain the change in the VDOS by elastic constants' fluctuations in the random non-continuous structure of the glass.[20] In this scheme, amorphous regions whose only difference lies in the strength of their bonds coexist and the denser ones (referred to as ''blobs'') confine the vibrations. Surotsev [320] recently improved the model by taking into account the contact between the ''blobs'' instead of considering a separation by soft matter. This refinement introduces some diffusive character to the BP.

(iii) The Soft Potential Model (SPM) considers the additional vibrations as Quazi-Localized Vibrations (QLVs) that resonate with sonic waves. These QLVs are vibrations created by disorder (or, possibly, low lying optical modes) that concern all atoms but with only a small fraction of them vibrating with a significant amplitude. The model was recently improved by Gurevich et al. [321] who introduced anharmonic effects.

4.2. Analysis of localized species and sublattices

Features from μRS can be specific to localized vibrations of weakly bonded or light species like, for instance, S_2^- ions entrapped in Lapis Lazuli [60]. In Bi2201 and Bi2212 bismuth

[17] Note that the spectrum does not strictly identify with the VDOS. Moreover, by comparison with Eq. (N2), $C(\overline{\nu})G(\overline{\nu})$ is analogous to the conductivity of the material. Quasi-Elastic and Inelastic Neutron Scattering also give insight into the frequency dependence of conductivity through the $P(\omega) = \omega \times \sigma(\omega)$ function [50, Chapters 21, 23, 25, 30].

[18] If one assumes, following the standard Debye model for acoustic branches, that $G(\overline{\nu})$ is proportional to $\overline{\nu}^2$, then the reduced intensity is expected to be proportional to $C(\overline{\nu})$ (see Eq. (30)).

[19] Slopes different from 2 on Log–Log scale plots of $C(\overline{\nu})$ were tentatively explained by the fractal nature of the tetrahedral network in gel-derived silica glass (silica aerogels) [312,314–317].

[20] The once popular model from Martin and Brenig [319] attributed the activation of Raman acoustic modes to density fluctuations modelled with a phenomenological Gaussian function.

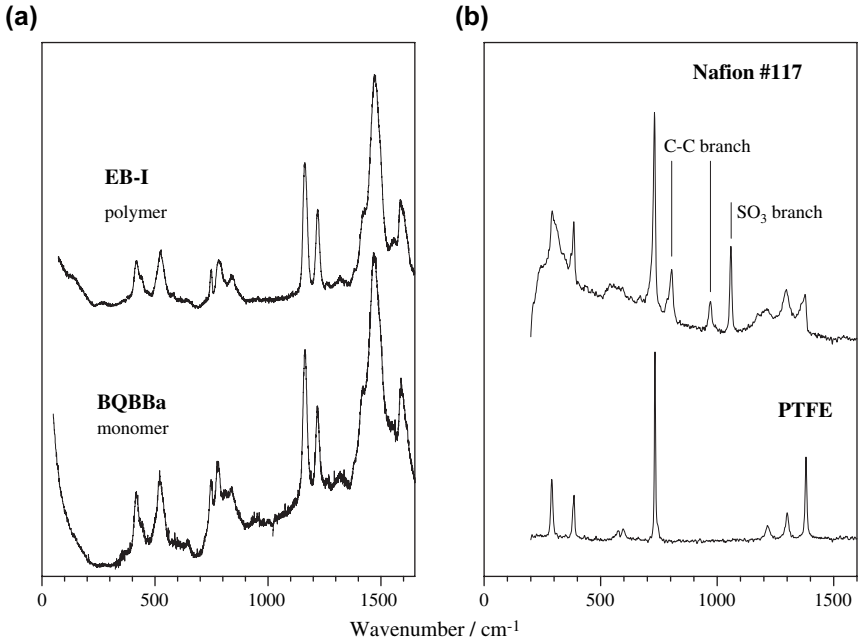

Fig. 12. (a) Comparison between the spectra from polyaniline precursor monomer ($l \sim 1$ nm) and polyaniline in one emeraldine base form ($l \sim 200$ nm) (adapted from Ref. [87]). (b) Comparison of PTFE and Nafion (PTFE-grafted with sulfonic groups) Raman spectra (adapted from Ref. [325, p. 215]).

cuprates, some modes are characteristic of the atom to which oxygen is bonded [322] while the activation of forbidden modes is related to the ordering of the mobile oxygens [323,324]. Similarly, Fig. 12 shows how polyaniline polymerisation produces little spectral modifications [87] while the orientational medium range disorder induced by the grafting of sulfonic groups on the PTFE framework of Nafion™ polymer membranes, for protonic conduction, produces obvious effects below 400 cm^{-1} [325].

In fact, μRS is very sensitive to sublattices in those many structures built with vibrationally independent species. Whenever the sublattices have chemical independence (e.g. iono-covalent silicate or phosphate frameworks hosting alkali ions), they give independent Raman contributions. If these contributions are taken apart by mass discrepancy, defects from either sublattice, for instance the cation and oxygen sublattices of perovskites, can be analysed separately [299,367,327]. The short distance cationic order in $ZrTiO_4$ [91,190] has also been investigated by RS but one of the best examples of sublattice discrimination is illustrated by ionic conductors.[21] For instance, Fig. 13 shows how a good energetic gap makes it possible to separate the short-range-ordered domains of conducting ions in β-alumina (a superionic solid selected in the seventies as a potential electrolyte) [55,328,329]. Because of their light weight and high polarisability, the protonic species exhibit particularly interesting dynamics, their vibrations being

[21] In ionic conductors, mobile ions are weakly bonded, which will add to mass contrast in distributing the vibrational energies.

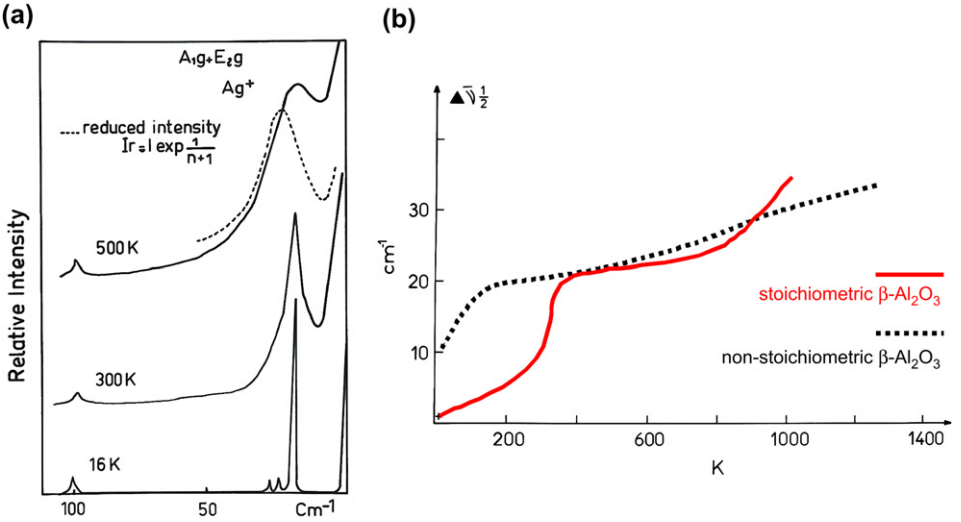

Fig. 13. (a) The ~25 cm^{-1} peak of β-alumina is characteristic of the conducting short range ordered Ag^+ bi-dimensional sub-lattice. (b) The half-width of the peak makes it possible to identify the melting temperature (~200 K) of this sub-lattice (adapted from Ref. [56, pp. 1388–1489]).

often independent from the host lattice (modes are localized and weakly coupled with the others) [50,330].

4.3. Carbon allotropy

The technique of μRS has been widely used to study carbon allotropes (diamond, graphite, fullerenes, nanotubes, …). It is indeed one of the few techniques sensitive to the full range of structural states present in this class of materials, from perfectly crystalline to amorphous. The common crystalline phases of carbon yield very simple spectra: diamond (sp^3 hybridisation) peaks at 1332 cm^{-1} (single mode of T_{2g} symmetry) whereas graphite (sp^2 hybridisation) has doubly degenerate E_{2g} modes at 42 and 1582 cm^{-1}. The latter is referred to as G band and corresponds to vibrations in the graphene planes (whose crystalline quality can be assessed by the width of the G band [168]) whereas the former corresponds to weak interplanar Van der Waals interactions (the reason for its low energy). Two additional modes appear whenever flaws are created, grain size is reduced or graphene planes are bent [168] (Fig. 14a). These modes are called D and D′ (the letter stands for "disorder"). D′ results from the splitting of the G band and peaks around 1620 cm^{-1}, at the value where the dispersion curve of graphite is the flattest. The intensity ratio of G to D′ bands depends on the proportion of distorted graphene planes [331]. Assuming the Raman scattering efficiencies σ are system-independent, then the number n of consecutive graphene planes should obey the following law [331]:

$$\frac{I_G}{I_{D'}} = \left(\frac{n-2}{2}\right)\frac{\sigma_G}{\sigma_{D'}} \tag{32}$$

The interpretation of the D band has been much debated. Despite its proximity to the diamond peak, D stems from graphite (the very low scattering efficiency of diamond would

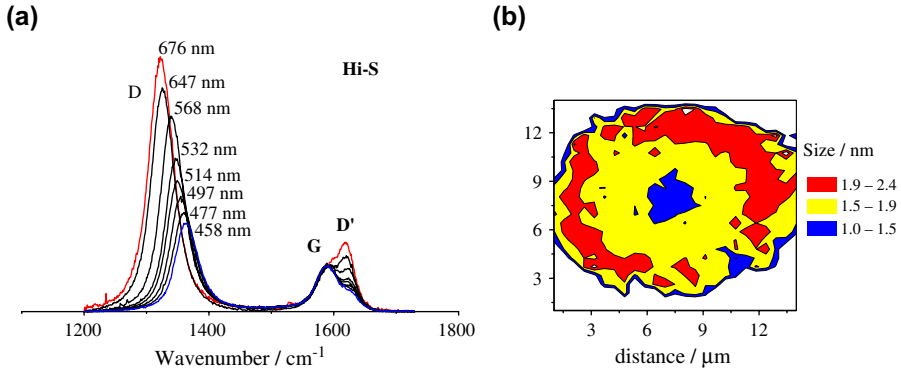

Fig. 14. (a) Raman spectra of the carbon nanoprecipitates in Hi–S Nicalon SiC fibres (Nippon Carbon) as a function of the laser excitation wavelength λ (adapted from Ref. [497, pp. 505–511]. (b) Tuinstra and Konig's calibration (Eq. (33)) was used to build a 2D "map" of carbon grain size in a SA3 SiC fibre (Ube Ind.). This is called "smart mapping" [39,212,214,333]. Reproduced from Ref. [39, pp. 8–16]. Copyright John Wiley & Sons Ltd.

otherwise make it much weaker). In 2000, Ferrari and Robertson [188] suggested that the D band resulted from a resonant enhancement of the modes from graphite dispersion curves having the same wavevector **k** as the exciting photons. This assignment provided an explanation for some peculiarities of the D band, such as its excitation wavelength dependence (Fig. 14a), but remained unsatisfying overall. Thomsen and Reich [332] showed that an unusually enhanced double resonance mechanism was at play for the D band.

Whatever the exact nature of the D band, it was soon shown that it depended on carbon grain size L_g, a feature for which an empirical law was proposed in 1970 by Tuinstra and Koenig [199][22]:

$$\frac{I_{D^{1350\ cm^{-1}}}}{I_{G^{1580\ cm^{-1}}}} = \frac{C(\lambda)}{L_g(\mathrm{nm})}, \quad C(\lambda = 514.5\ \mathrm{nm}) = 44 \tag{33}$$

The so-called "Tuinstra and Konig" calibration has been used extensively for the "qualitative" control of carbon structural transformations, mostly in amorphous carbon [334,335] and Diamond-Like Carbon (DLC) [336–342] films but also on radial cross sections in carbon micro-rods [343] and electrodes [344]. A direct proportionality between the I_D/I_G ratio and the sp^3 content, as obtained from EELS experiments, has been reported in amorphous carbon films [345].

In 1985, Kroto et al. [346] were the first to find experimental evidence of crystalline forms of carbon other than diamond and graphite. These corresponded to an assembling of pentagonal, hexagonal and heptagonal carbon rings to form spheroids (fullerenes) [347]. Crystallization by closing of rolled graphene planes is also possible, in which case Carbon Nanotubes (CNTs) are formed [348]. These CNTs have enormous application potential as they are among the hardest known materials and are able to conduct single charges unidirectionally [349]. Fig. 15a shows how a single $\{n,m\}$ couple of integers is sufficient to fully characterize one CNT. This tube is

[22] This calibration is not valid below 2 nm [188].

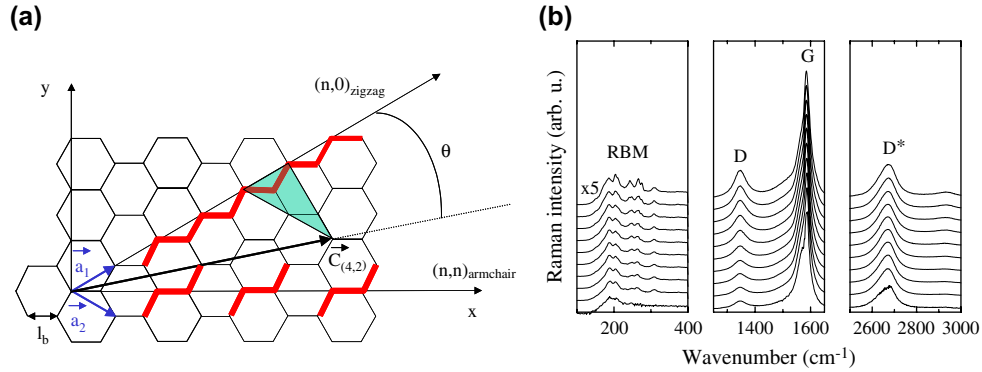

Fig. 15. (a) Nanotubes can be described by the rolling of a chiral vector $\vec{\mathbf{c}} = n\vec{\mathbf{a}}_1 + m\vec{\mathbf{a}}_2$ in a graphene plane. (b) Raman spectra of Double Wall Carbon Nanotubes (DWCNTs) filled with PbI_2. Reprinted from Ref. [498] with permission. Copyright 2005 by the American Physical Society.

obtained by the rolling of the chiral vector $\vec{\mathbf{c}} = n\vec{\mathbf{a}}_1 + m\vec{\mathbf{a}}_2$ in a graphene plane and its diameter d_{NT} and chiral angle θ are simply given by:

$$d_{\mathrm{NT}} = \frac{\|\vec{\mathbf{c}}\|}{\pi} = \frac{l_{\mathrm{b}}\sqrt{3}\sqrt{n^2+m^2+nm}}{\pi} \tag{34}$$

$$\theta = \arcsin\left(\frac{m\sqrt{3}}{2\sqrt{n^2+m^2+nm}}\right) \tag{35}$$

Fig. 15b shows the Raman spectra of some Double Wall CNTs (DWCNTs). The bond angles and lengths no longer correspond to a perfect sp^2 hybridisation but Raman modes can still be derived from the graphite dispersion curves [350,351]. Eklund et al. [352] showed the G wavenumber to remain at 1581 cm^{-1} in CNTs with radii above 15 nm but to drop to 1465 cm^{-1} below this value.

It should be noted that the Radial Breathing Mode (RBM) shown in Fig. 15b can be used to measure d_{NT} accurately [353]. Based on a zone folding model, Eklund et al. [352] predicted the relationship between $\overline{\nu}_{\mathrm{RBM}}$ and d_{NT}, which was calibrated afterwards [354–357]:

$$d_{\mathrm{NT}}(\mathrm{nm}) = \frac{223.75}{\overline{\nu}_{\mathrm{RBM}}(\mathrm{cm}^{-1})} \tag{36}$$

CNTs with different $\{n,m\}$ may be similar in diameter but they will resonate at different laser energies [358,359]. These correspond to interband transitions between the valence and conduction band at Van Hove singularities. The relationship has been established and $\{n,m\}$ can then be precisely found on the basis of μRS [360]. This is interesting because $\{n,m\}$ determines many properties. For instance, nanotubes with $|n-m| = 3q$ (q integer) are metallic whereas those for which $|n-m| = 3q \pm 1$ are semiconductors [361]. The behaviour of the D [362,363], G [364] or D*[23] [363] bands has also been studied extensively. Refs. [350] and [351] provide thorough descriptions of the RS of CNTs.

[23] D* is the overtone of D-band. It is alternatively referred to as G' by analogy with a second order band found in disordered graphite (see Fig. 21).

4.4. Nanophased SiC fibres

SiC fibres, which are among the most stable inorganic fibres, are mostly produced by the 3D reticulation of a polymeric precursor.[24] Their nano-crystalline structure offers the best compromise between a good homogeneity (a characteristics of the amorphous state) and a high bond density (a characteristics of the crystalline state). Their very smooth surface and the lack of defects explain tensile strengths σ_r as high as 3 GPa. These fibres are designed to reinforce composites working at very high temperatures ($\sim$1200 to 1400 °C) in oxidizing and corrosive atmospheres (carbon fibres oxidize at 500 °C whereas alumina, zirconia and mullite fibres properties degrade above 1100–1200 °C [365] as they crystallize).

Micro-Raman Spectroscopy is particularly well suited to study SiC fibres because it gives a good signal for both the main SiC and the secondary carbon phases. Fig. 16a illustrates this fact by the monitoring of the SiC decarburation in NLM fibres submitted to alkaline corrosion. First, the different forms of partially oxidized or nitrided carbon can be identified [23]. The SiC spectrum mainly consists of peaks around 795 and 970 cm^{-1}. They correspond respectively to the transverse optical (TO_1 and TO_2; degenerate) and longitudinal optical (LO) modes of β-SiC[25], which X-ray diffraction identified in Nicalon (NLM, Hi and Hi–S) [369], SA [370] and Sylramic [371] fibres. Additional bands correspond to SiC polytypes (see Fig. 17: the Brillouin Zone folding generates satellite lines on the low energy side of the TO and LO bands [212,213,372–377]), to amorphous SiC (broad symmetric background) and to asymmetric VDOS projections when a "random" faulting in the stacking sequence folds the BZ in countless ways [372].

The SiC contributions in the spectra in Fig. 16b were fitted using the PCM (see Section 3.3.1). This returned "coherence lengths" of 6.5 ± 1.2 nm (TO) or 3.8 ± 0.9 nm (LO), in good agreement with the size of SiC polytype domains appearing in Fig. 16c. We performed similar fits on spectra of Hi–S, SA and Sylramic nearly stoichiometric third generation SiC fibres [378], obtained from grafted polycarbosilane [370,379–382]. Only the Hi–S bands could not be adjusted at $\vec{\mathbf{k}}_0 = \vec{0}$, hinting at a greater stacking disorder. The coherence length was higher for Sylramic and SA fibres, in agreement with a higher grain size (100–500 nm [380] and 200 nm [383], respectively, against 20 nm in the Hi–S [379]).

4.5. CeO_2

The electrical properties and chemical reactivity of nano-crystalline CeO_2 make it interesting for applications such as gas sensor, fuel cells electrolyte material, catalyst for oxygen storage, etc. [153,196,215]. Ceria only first order Raman active mode is the triply degenerate symmetrical stretching vibration of the CeO_8 vibrational unit at $\sim$465 cm^{-1}. Only the oxygen atoms move in this mode [153,196,215], which is therefore very sensitive to the oxygen

[24] The main alternative is Chemical Vapour Deposition (CVD) of SiC on a carbon fibre core (SCS-6 fibre from Textron).

[25] In SiC structures, Si and C "bilayers" are referred to as "h" if they are deduced from the underlying bilayer by a simple translation. However, if an additional 180° rotation (around the Si–C bonds linking the bilayers) is required for superposition, then bilayers are referred to as "*k*". Each periodic stacking sequence defines a polytype which is classified according to Ramsdell notation by first giving the number *N* of bilayers in the stacking cell and then the cell type [366–368]. The "all *k*" polytype (β-SiC phase) is the 3C (cubic) polytype. All other polytypes (α-SiC phase) are either NH (hexagonal) or NR (rhombohedral).

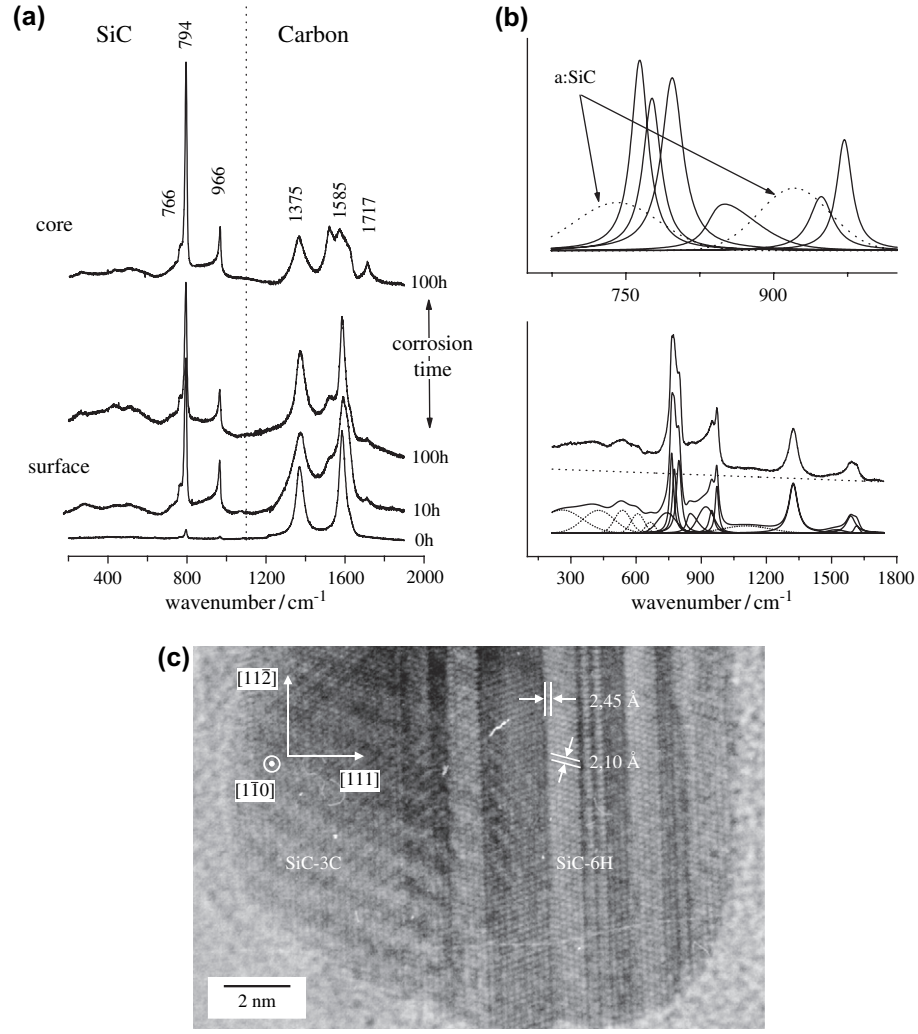

Fig. 16. (a) Effect of alkaline corrosion by $NaNO_3$ salt on the Raman spectrum of annealed NLM SiC fibres ($\lambda_{laser} = 457.94$ nm). Note the core spectrum was recorded on a fibre cross-section which has been exposed to corrosion (adapted from Ref. [23, pp. 306–315]). (b) Raman spectra recorded with 632.1 nm excitation on one NLM SiC fibre annealed for 10 h, at 1600 °C, under reducing atmosphere. The fit was obtained using the PCM [212,213] and a:SiC stands for "amorphous" silicon carbide. (c) High Resolution Transmission Electron Microscopy (HRTEM) micrograph of one NLM fibre, after 10 h reducing annealing at 1600 °C [209] (by courtesy of M. Havel and L. Mazerolles). The picture shows one SiC nanocrystal embedded in amorphous SiC.

sublattice disorder resulting from processing and/or grain-size-induced non-stoichiometry. Spanier et al. [215] simultaneously considered phonon confinement, stress, size distribution and non-stoichiometry as possible causes for lineshape variations in the Raman spectra of ceria. Fig. 6 shows the line width dependence versus the grain size for ceria samples prepared on Al_2O_3 substrates using a polymer precursor spin-coating process ensuring an homogeneous grain size distribution [386]. The broadening is obvious on Fig. 18a, which also shows

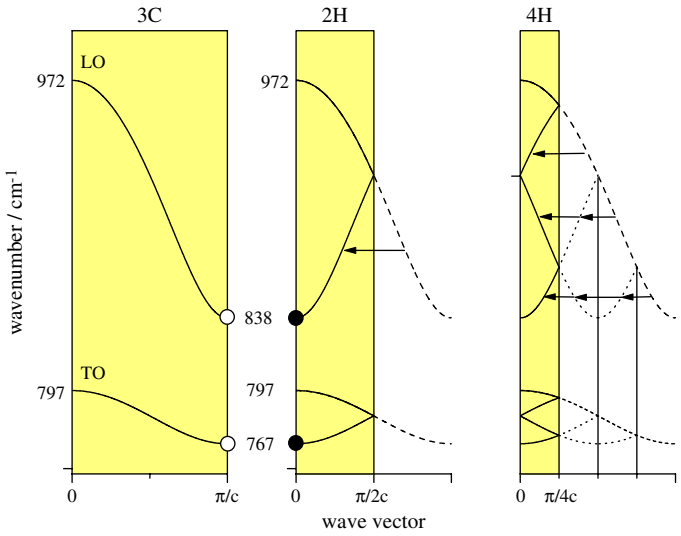

Fig. 17. Dispersion curves for the 3C, 2H and 4H polytypes, in equivalent directions of the reciprocal space. The ''extended Brillouin zone'' obtained by unfolding hexagonal (or rhombohedral) polytypes curves matches the ''standard zone'' of 3C SiC [244,384]. 3C–SiC modes marked with open circles are inactive but can be measured on the Raman spectra of 2H polytype (black circles) where they correspond to BZc.

PCM-derived fits of the Raman spectra [196]. The confinement lengths are plotted in Fig. 18b as a function of the grain size measured by X-ray diffraction: the extension of the homogeneous domains is constant for grain diameters above 100 nm. Since a direct relationship is expected for the 465 cm^{-1} band with the oxygen sublattice, Kosacki et al. [196,386] proposed L to correspond to the average distance between oxygen vacancies. Below 100 nm, it decreases with the grain size following a cubic root law and this could be successfully accounted for by the reduction of vacancy formation enthalpy for nanocrystalline microstructures.

Fig. 18c shows the evidence for the stronger influence of substitutional disorder over the stoichiometric one. The broadening in Gd-substituted CeO_2 is indeed much more important than the one associated with grain size-induced non-stoichiometry only (Fig. 18a). A separation of the short-range disorder and size-induced band broadening was similarly achieved for nano-$InVO_4$ oxide (an electrode material for Li^+ intercalation) [26,27]. Note all samples in Fig. 18c are single crystals with the same highly symmetric structure. Their X-ray diffractograms would look very much alike and only fine refinements characterize their differences.

5. The mechanical characterization of nanophases by micro-Raman Spectroscopy

A growing number of devices involve nanophased materials. Hence there is a need for *in situ* non-destructive characterization methods. We have already seen that the μRS sensitivity to chemical bonds (stretching and bending modes) and their spatial arrangement (libration and external modes) makes it a good tool for probing crystallo-chemistry and reactions at the nanoscale. We shall now demonstrate how nanoprecipitates can be used as ''mechanical probes'' [387–392]. In fact, very few experimental techniques lend themselves to micromechanical characterization of heterogeneous materials. Most of them are not specific and all of them have limitations. First, *X-rays* [393–395] and *neutron* [396,397] diffractions only work

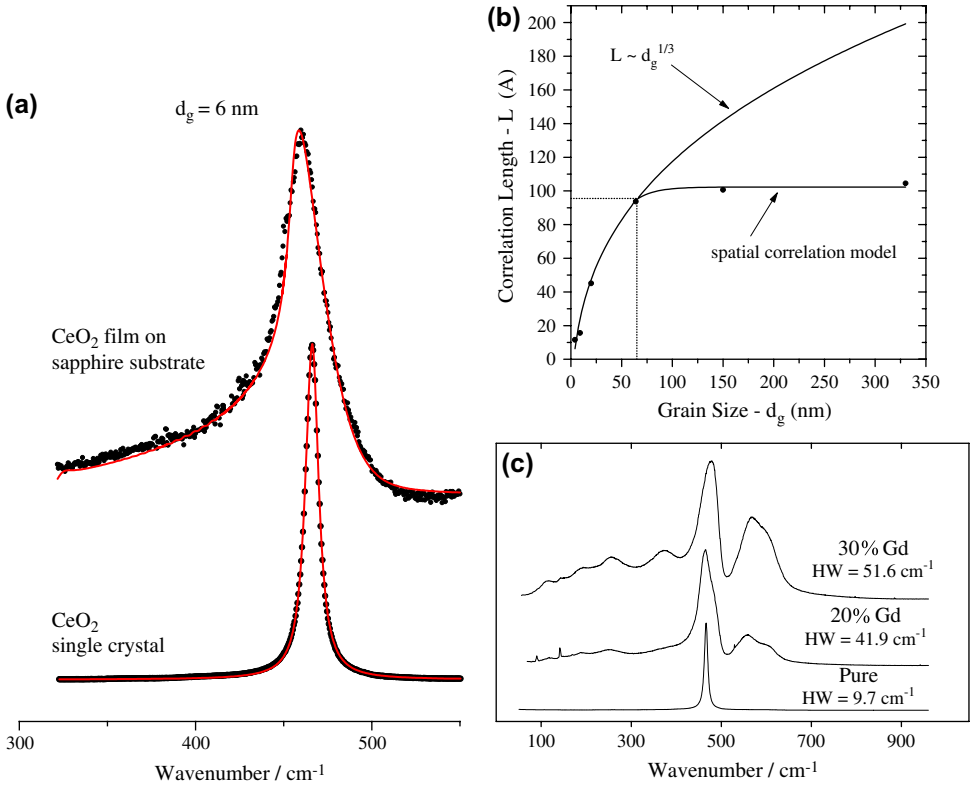

Fig. 18. (a) Grain size effect on ceria Raman signature. The fits were obtained using the PCM (Section 3.3.1). (b) Comparison of the confinement length L obtained through the PCM with the grain size obtained by X-ray diffraction. Reprinted from Ref. [196, pp. 99–105] with permission from Elsevier. (c) The spectra of gadolinium-doped ceria single crystals depend significantly on the doping level (I. Kosacki and Ph. Colomban, private communication).

on crystallized samples. *Ultrasound* analysis gives a dynamical view of cracking rather than stress measurements [398–400], *photoelastometry* supposes perfect transparency [401,402] and SEM observations of resin grids only give an indirect measure of the surface deformations [403–405]. Other specific methods exist like instrumented *(micro–nano)-indentation* [406–410], *fragmentation* [411–416], "*pull-out*" [417], "*push-out*" [418] and "*microdroplet*" [413] tests but the validity of the models used for data interpretation is often questionable due to their usually large number of parameters. Besides, these methods are sometimes inapplicable. For instance, carbon fibre-reinforced composites cannot be tested by conventional push-in micro-indentation because the fibres have a small diameter and cleave too easily.

5.1. Raman stress sensitivity

5.1.1. The anharmonicity of atomic bonds

Below, we will assume that each stretching mode is specific to one given chemical bond. As long as the elongation is limited, the bond can be modelled by a spring of length l_b, reduced

mass μ and constant stiffness k_b. This is the so-called harmonic model where the interatomic potential has the form $V(l_b) = (k_b/2)(l_b - l_0)^2$:

$$\overline{\nu}_{vib} = \frac{1}{2\pi c}\sqrt{\frac{k_b}{\mu}} \tag{37}$$

$$k_b = \frac{\partial^2 V}{\partial l_b^2} \tag{38}$$

There is no l_b dependence for the wavenumber in Eq. (37) and the harmonic potential does not predict any stress sensitivity for Raman bands. Yet such modelling rules out the phenomenon of bond dissociation ($l_b \to \infty$) and does not correctly account for atoms non-interpenetrability ($l_b \to 0$). In fact, the interaction potential should not be limited to a quadratic term and all real bonds are somewhat anharmonic (Fig. 19). They include attractive and repulsive contributions, for which Mie and Grüneisen (Table 1) proposed the following expression, with A, R, a and r being positive constants [419]:

$$V(l_b) = V_0 + V_{attractive}(l_b) + V_{repulsive}(l_b) = V_0 - A \times l_b^{-a} + R \times l_b^{-r} \tag{39}$$

In spite of its very significant influence on the physical behaviour of materials (only it can explain thermal expansion or the finite value of thermal conductivity [421]), anharmonicity is often considered as a simple perturbation: in what is referred to as the "quasi-harmonic" approximation, one considers that Eqs. (37) and (38) are applicable to real potentials. According to Fig. 19, atoms are bonded by strings whose stiffness ($\partial^2 V/\partial l_b^2$) increases under compression and decreases under tension.

In the case of the "quasi-harmonic" approximation, Eq. (39) is equivalent to:

$$\frac{d\overline{\nu}_{vib}}{\overline{\nu}_0} = \frac{dk}{2k} = \frac{1}{2}\frac{a(a+1)(a+2)A \times l_b^{-(a+3)} - r(r+1)(r+2)R \times l_b^{-(r+3)}}{r(r+1)R \times l_b^{-(r+2)} - a(a+1)A \times l_b^{-(a+2)}} dl_b \tag{40}$$

Introducing the bond elongation $\varepsilon_l = (l_b - l_0)/l_0$, a Taylor expansion of $l_b^x = l_0^x(1+\varepsilon_l)^x$ (small strain assumption) and the requirement for the potential first derivative to be nil at $l_b = l_0$ yield:

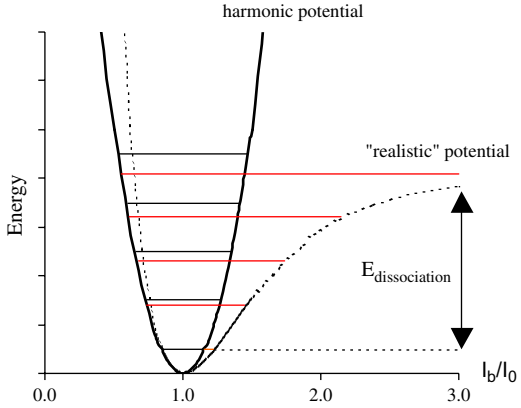

Fig. 19. Comparison of realistic and harmonic bond potentials.

Table 1
Parameters of Mie–Grüneisen potentials in solids [420]

Bonding	a	r
Van der Waals	6	12
Ionic	1	9
Covalent	$a+r\sim 3$	

$$\frac{\mathrm{d}\overline{\nu}_{\mathrm{vib}}}{\overline{\nu}_0} = -\frac{(a+r+3)}{2}\times \varepsilon_{l_{\mathrm{b}}} \tag{41}$$

$$\overline{\nu}_{\mathrm{vib}} = \overline{\nu}_0\left(1-\left(\frac{a+r+3}{2}\right)\times \varepsilon_{l_{\mathrm{b}}}\right) \tag{42}$$

There is therefore a direct proportionality factor between the wavenumber shift and bond deformation[26]:

$$\overline{\nu}_{\mathrm{vib}} = \overline{\nu}_0 + S^{\varepsilon}_{\mathrm{b}}\times \varepsilon^{\%}_{l_{\mathrm{b}}} \tag{43}$$

From a macroscopic point of view, a tensile (resp. compressive) stress is expected to decrease (resp. increase) $\overline{\nu}$. The effect will be the more significant as the coefficients a and r will be high, in other words as the bonds will be weak[27].

5.1.2. Raman Spectroscopy of single crystals under hydrostatic compression

Many RS experiments carried on stressed materials involve single crystals hydrostatically compressed in diamond anvil cells (DACs), where the pressure P_{h} is transmitted by a fluid [423–425]. Wavenumbers then obey a quasi-linear dependency with respect to P_{h} [366,426–429]:

$$\overline{\nu}_{\mathrm{vib}} = \overline{\nu}_0 + a\times P_{\mathrm{h}} + b\times P_{\mathrm{h}}^2 \sim \overline{\nu}_0 + a'\times P_{\mathrm{h}} \tag{44}$$

Such a behaviour indicates an equivalency between the macroscopic (Eq. (44)) and microscopic (Eq. (43)) responses to external perturbations. DAC experiments are usually used to measure the Grüneisen parameters of Raman modes [366,426–428,430–433]:

$$\gamma_{\mathrm{m}} = -\frac{\partial \log \overline{\nu}_{\mathrm{m}}}{\partial \log V} = \frac{1}{\beta_{\mathrm{T}}}\frac{\partial \log \overline{\nu}_{\mathrm{m}}}{\partial P} \tag{45}$$

In Eq. (45), V is the volume and β_{T} the isothermal compressibility. γ_{m} is almost independent of the mode in isotropic solids with one kind of bond controlling the lattice dynamics. This happens for covalent/iono-covalent materials like diamond and 3D semiconductors from groups IV and III-V, where γ is close to 1 [423,424]. It becomes about 2 in II–VI semiconductors and rises to 3 in alkali halides [424]. In molecular crystals, γ often changes from one mode to another [423] with, usually, $\gamma_{\text{internal modes}} \ll \gamma_{\text{external modes}}$.

[26] The superscript "%" indicates a deformation expressed as a percentage.

[27] The anharmonicity of the bonding potential is referred to as a "mechanical anharmonicity". Note that "electrical anharmonicity" also exists in RS. It corresponds to a second order Taylor expansion of the polarisability in Eq. (2) [422].

In an isotropic material under hydrostatic compression:

$$P_h = \frac{dV}{V_0} = 3\varepsilon_l \tag{46}$$

The combination of Eqs. (41), (45) and (46) then leads to:

$$\gamma = \frac{a + r + 3}{6} \tag{47}$$

The Grüneisen parameter thus becomes a direct characteristic of the interatomic potentials (parameters a and r were introduced in Eq. (39)).

5.1.3. Raman Spectroscopy of single crystals under general stress

If a deformation is applied to a single crystal, the vibrational mode independence is lost and phonon–phonon couplings occur [434]. The fundamental equation of Dynamics then becomes:

$$\mu\frac{\partial^2 r_i}{\partial t^2} = -\sum_{jlm}\frac{\partial k_{ij}}{\partial \varepsilon_{lm}}\varepsilon_{lm} r_j = -\sum_{jlm} K_{ijlm} r_j$$
$$= -\left[k_{ii} \times r_i + \sum_{\substack{jlm \\ j\neq i}} K_{ijlm} r_j\right], \quad \begin{cases} i,j,l,m = x,y \text{ or } z \\ r_i = \text{component of normal coordinate} \\ \qquad r \text{ in direction } i \\ \mu = \text{reduced mass} \end{cases} \tag{48}$$

The wavenumber shifts can then be directly linked to any macroscopic stress/strain via the elastic compliance tensor[28] and the K_{ijlm} coefficients that describe the strain-induced deformation of the bonding potentials, in other words: anharmonicity [434]. Few of these coefficients are independent in high-symmetry crystals (see [435] in cubic crystals or [436,437] for hexagonal corundum). The mathematical expressions for the stress dependency of optical modes in cubic crystals can be derived for given crystallographic directions [89,434] and planes [438–442][29]. Ager and Drory [440] reported less than 15% disagreement between the biaxial residual stress measured by RS in a diamond film (deposited on a titanium alloy) using linear combination of uniaxial stresses perpendicular to the growth direction, and the theoretical value expected from elasticity theory. The same kinds of measurements are common for semiconductors [443,444].

5.1.4. The case of non-crystalline materials

In polycrystalline or amorphous materials, the tensor formalism is irrelevant (stress directions are unknown). We must therefore adopt a ''statistical'' approach. Let θ_b be the initial angle between a bond and the solicitation axis in a material macroscopically strained to $\Delta\varepsilon_M^{\%}$. The

[28] Compliance terms S_{ij} are defined according of Voigt's notation by $\varepsilon_i = S_{ij} \times \sigma_j$ (ε = strain; σ = stress; $i = 1, 2, 3, 4, 5, 6$ correspond to directions xx, yy, zz, yz, xz and xy, respectively, with $\varepsilon_4 = 2 \times \varepsilon_{yz}$, $\varepsilon_5 = 2 \times \varepsilon_{xz}$ and $\varepsilon_6 = 2 \times \varepsilon_{xy}$).

[29] Some errors in formulas from Ager et al. [440] and Cheong et al. [441] were listed in Ref. [378].

simplest assumption is to consider that this bond is strained by an amount of $\Delta\varepsilon_{\mathrm{b}}^{\%} = \Delta\varepsilon_{\mathrm{M}}^{\%} \cos\theta_{\mathrm{b}}$. The resultant shift is an integration of Eq. (43) over all bonds:

$$\Delta\overline{\nu}_{\mathrm{tot}} \approx S_{\mathrm{b}}^{\varepsilon} \times \int_{\theta=0}^{\theta=\frac{\pi}{2}} \left[p(\theta) \times \Delta\varepsilon_{\mathrm{M}}^{\%} \cos(\theta)\right] \mathrm{d}\theta \tag{49}$$

In Eq. (49), $p(\theta)$ represents the probability for θ_{b} to be θ. If the material is isotropic, then $p(\theta)$ is a constant and:

$$\Delta\overline{\nu}_{\mathrm{total}} \sim S^{\varepsilon} \times \Delta\varepsilon_{\mathrm{M}}^{\%} \tag{50}$$

Therefore, a proportionality factor S^{ε}, expressed in units of $\mathrm{cm}^{-1}/\%$, links the wavenumber shift to the macroscopic strain in isotropic materials. Besides, if Hooke's law applies over the full strain exploration,[30] then:

$$\Delta\overline{\nu} = S^{\varepsilon} \times \frac{100 \times \Delta\sigma}{E} = S^{\sigma} \times \Delta\sigma \tag{51}$$

The applied stress $\Delta\sigma$ and Young's modulus E are expressed in GPa. From hereon, the $S^{\varepsilon/\sigma}$ symbol, let us name it the Raman Mechanical Coefficient (RMC),[31] will be used whenever comments apply to both S^{σ} and S^{ε} factors. $S^{\varepsilon/\sigma}$ is usually negative: wavenumbers decrease under tension and conversely.[32]

The technique of micro-Raman Extensometry (μRE) consists of deriving an S^{ε} value from a reference sample subjected to controlled strain (Fig. 20) for later in situ strain determination in a composite [79,387,390–392,413] (see Sections 5.2 and 5.3). A peculiarity of nanophased materials is that stress relaxation is expected at grain interfaces/interphases. The numerical values of the RMC end up being lower than in a single crystal. They are even lower if nanocrystals from a secondary phase are used as the mechanical probe: the more dispersed a phase, the lower its contribution to stress transfer and the lower the corresponding $S^{\varepsilon/\sigma}$ (Fig. 21). For instance, S^{σ} for the O–Si–O bending mode $\sim 450\ \mathrm{cm}^{-1}$ (see Fig. 11) is $-5\ \mathrm{cm}^{-1}$/GPa in amorphous silica fibres, where the tetrahedra are continuously bridged by oxygen atoms, but is 5–10 times lower for isolated rings of only 3–4 tetrahedra [445].

5.2. In-situ micro-Raman Extensometry of ceramic fibre-reinforced composites

The reinforcement of ceramic materials with long ceramic fibres leads to low density and refractory materials of high damage tolerance. Therefore they should be an appropriate substitute for metal alloys in advanced engines (turbines) and waste treatment energy plants [365]. Ceramic fibres can also be directly incorporated in metal matrices to increase their high temperature mechanical properties [365]. These are often hard to measure and an optical non-destructive technique such as μRE will prove very useful in this regard. One of the peculiarities observed in ceramic fibres prepared from polymeric precursors is that there is no accumulation of impurities at the grain boundaries. Due to the lack of such usual diffusion regulators,

[30] Hooke's law ($\sigma = E\varepsilon$) supposes a proportionality factor (the so-called Young's modulus) exists between stress (σ) and deformation (ε).

[31] S^{ε} is sometimes referred to as the Raman Frequency Gauge Factor (RFGF).

[32] ε and σ are positive for tensile solicitations.

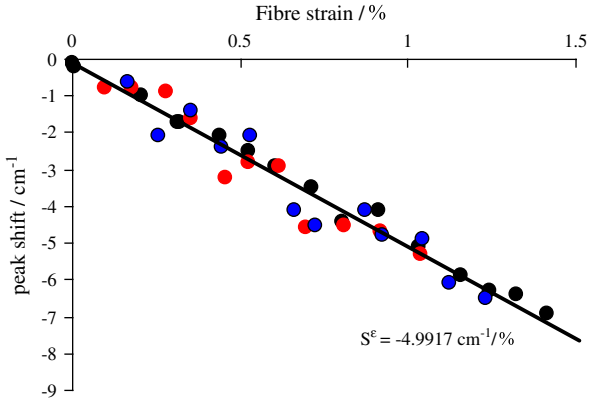

Fig. 20. Calibration of the Raman Mechanical Coefficient ($S^{\varepsilon/\sigma}$) of the carbon G band (see Section 4.3) for three IM7 fibres (adapted from Ref. [485, pp. 646–651]).

abnormal grain growth is therefore very common and responsible for mechanical degradation [1]. A close relationship has been proven, for instance, between the micro-hardness and short-range ordering in sol–gel prepared nano-crystalline oxides [446] and some authors have already pointed out that the overall mechanical ability of fibres is governed by their microstructure [447–449]. The expertise of the fibre manufacturers consists in postponing the onset of crystallization and grain growth. The RMC difference between the reference single crystals and embedded nanoparticles under the same macroscopic stress can tell a lot about the fibre structure (Fig. 21). Thus, S^{ε} is $-4.2\ \mathrm{cm}^{-1}/\%$ ($\sim -1\ \mathrm{cm}^{-1}/\mathrm{GPa}$ with $E = 420$ GPa [369]) for

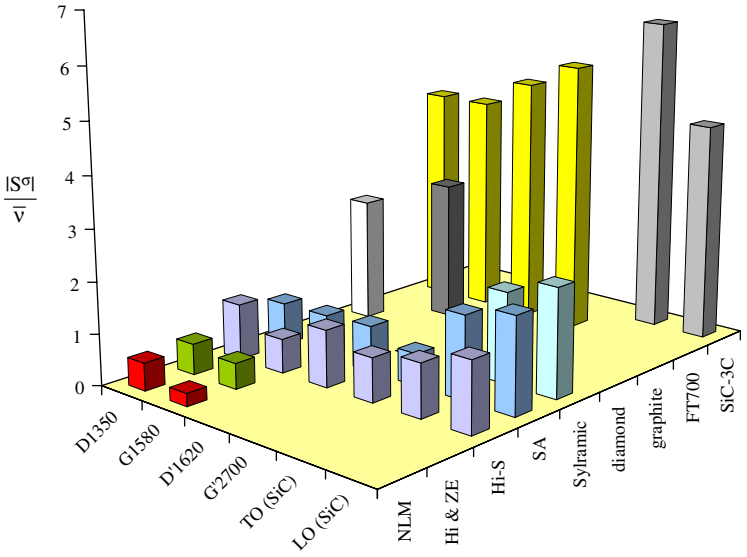

Fig. 21. Comparison of $S^{\sigma}/\bar{\nu}$ values for the D, G, D' and G' modes of carbon and the optical modes of SiC in different materials (NLM, Hi, Hi–S, SA, Sylramic: SiC fibres; FT700: carbon fibre). Reprinted from Ref. [499; pp. 617–620] with the permission of Trans Tech Public Inc.

the SiC LO mode in the Hi–S fibre [378], which is lower than in SiC single crystals axially strained along [100] ($-1.5\ \mathrm{cm^{-1}/GPa}$) or [001] ($-3.0\ \mathrm{cm^{-1}/GPa}$) directions [378]. In such a quasi-stoichiometric SiC fibre, the carbon sensitivity is almost nil.

Eq. (50), which is derived from Eq. (43), assumes a small bond deformation. Yet, the RMCs are measured up to the breaking point. For actual fibres, a better description of S^{ε} is given with second or third order polynomial laws [450–452] and $S^{\varepsilon}_{\mathrm{Compression}} < S^{\varepsilon}_{\mathrm{Tension}}$ [388,452–454]. Yet, the $S^{\varepsilon}_{\mathrm{Compression}}$ to $S^{\varepsilon}_{\mathrm{Tension}}$ ratio gets close to one in stiff materials (high Young's modulus) containing iono-covalent bonds and isotropic 3D-bonded inorganic structures. Such materials do indeed have a lower sensitivity to flaws than chain-like structures, which flaws open under tension and close under compression. Thus, the difference between $S^{\varepsilon/\sigma}_{\mathrm{Compression}}$ and $S^{\varepsilon/\sigma}_{\mathrm{Tension}}$ is lower in graphitic carbon fibres than in linear chain-based fibres (PPTA, PBZT). Pitch fibres have better aligned and closer graphene planes than PAN fibres. They also have more ''reversible'' S^{ε} coefficients [391,416]. The technique of μRE was most specifically applied to model polymer matrix systems reinforced with PAN [389,415,416,454–463] and Pitch [414,452] carbon fibres, aramid fibres [389,413,417,447,464–469], polyethylene fibres [470] or carbon nanotubes [471]. The matrix was then sufficiently transparent for *in situ* analysis of the embedded reinforcement material. The S^{ε} calibrations and in-situ measurement of Raman spectra could be used to generate strain profiles $\varepsilon_{\mathrm{f}}(l)$ along the fibre, from which other properties like (longitudinal) residual strain ($\varepsilon_{\mathrm{f}}(l)$ in the lack of external stress) [414,452,455,458,459,469,470], interfacial shear stress τ_{ci} (Fig. 22 and Ref. [458]), stress concentration factors [454,456–458,460,462,468]), ineffective lengths[33] (IL) [458], the interfacial fracture energy G_{i} [462] or the Coulombian friction coefficient (the proportionality factor between σ_{radial} and τ_{ci}) [415] can be derived.

The key points for getting reliable μRE results are an accurate determination of S^{ε} (Fig. 20) keeping in mind that stress is not the only possible reason for peak shifts. Fibre/matrix interdiffusion and laser-induced heating[34] produce chemical and thermal shifts, which are accounted for in the following expression[35] [90,378]:

$$\Delta\sigma = \frac{E_{\mathrm{f}} \times \left((\overline{\nu}_{\text{in situ}} - \overline{\nu}_{\sigma=0}) + (\overline{\nu}^{\text{fibre}}_{\text{as-received}} - \overline{\nu}^{\text{fibre}}_{\text{extracted from the composite}}) + P_{\mathrm{l}} \times (S^{P}_{\text{reference}} - S^{P}_{\text{sample}}) \right)}{100 \times S^{\varepsilon}_{\text{fibre}}} \tag{52}$$

In Eq. (52), E_{f} is the fibre Young's modulus and measures the quasi-linear dependence of the wavenumber on the laser power P_{l}. The spatial resolution of μRE makes it easy to study the effect of a fibre environment (neighbouring fibres or cracks, fibre sizing, humidity, etc.) on stress [454,456–459,465,468,469]. The results fulfil relatively well the predictions of micromechanical models such as Cox's (axial stress for elastic fibre and matrix, the so-called ''shear-lag'' model) [413,415], Piggott's (applies after fibre/matrix decohesion and for matrix creeping) [413,417,465,473], the friction model of Kelly and Tyson [415,459,473] or that of Cook and Gordon (stress concentration in the vicinity of cracks) [465].

[33] The length over which stress builds up from zero (at a fibre tip or a matrix crack) to its maximum value.

[34] Thermal expansion has the same effect on bond lengths (hence on $\overline{\nu}$) as a tensile stress [472].

[35] This equation neglects the statistical wavenumber dispersion in the reference and supposes wavenumbers are corrected for any instability of the Raman spectrometer.

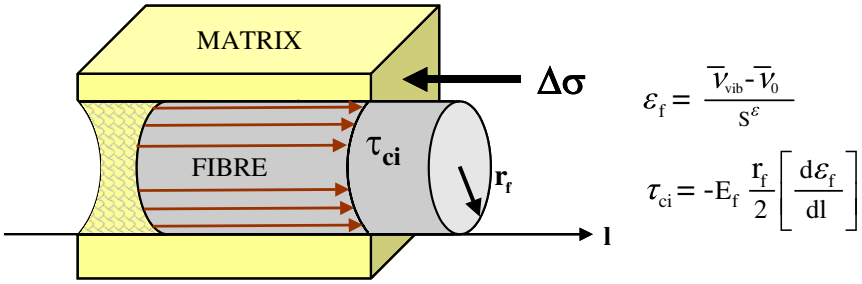

Fig. 22. Diagram of fibre–matrix sliding. The deformations of the fibre and matrix when a stress $\Delta\sigma$ is applied to the composite are in the ratio of the Young's Moduli ($\Delta\sigma = E_f \times \Delta\varepsilon_f = E_m \times \Delta\varepsilon_m$). Hence the interfacial shear stress τ_{ci} between the fibre and the matrix [458].

The applicability of μRE to composites with either low transparency ceramic matrix [90,373,474] or intrinsically opaque inter-metallic matrix [475] has recently been demonstrated, despite their high consolidation temperatures; fibre/matrix inter-diffusions might complicate the study. Given the much higher Young's modulus of such matrices with respect to resins, Ineffective Lengths (ILs) are small enough (a few micrometers only instead of hundreds [458]) for a cross-section analysis to give results close to those obtained with longitudinal probing [90,389,392,474,475]. Yang and Young [473,476,477] studied $\varepsilon_f(l)$ in model single fibre NLM/pyrex and NLM/SiC [478] composites. Bollet et al. [479] measured the influence of micro-cracking in SiC/glass–ceramic composites. Pezzotti [480] also used μRE to study cracking in "monolithic" ceramics. Chollon and Takahashi [481] studied a C/C composite. Colomban and co-workers measured residual stress in C_f/mullite [474], NLM/mullite [474] and Hi-Nicalon/mullite [373,482] composites.

5.3. In-situ analysis of a C_f/epoxy composite

Nine-micrometer diameter PAN-based low crystallinity IM7 carbon fibres (Hexcel Fibres, USA) were used for the unidirectional reinforcement of an epoxy matrix processed by radical-polymerisation under γ irradiation. The resulting composite (γ-pol) was nearly opaque, rather unfavourable conditions for a μRE study. These notwithstanding, γ-pol was subjected to a constant tensile strain of 1% and the spectra of one particular fibre chosen in a fibre-poor region could be recorded, starting from the tip, through a few tens of micrometers of the matrix material (Fig. 23a). This ~300 μm long fibre was longer than the usual IL in polymer matrices (~200 μm [390,456,458]), which was mandatory to observe full fibre–matrix interaction. The results of the spectra fitting are illustrated in Fig. 23b. The D and G bands (see Section 4.3) have very similar variations, with a few singular points. These might result from the local environment, such as the presence of cracks or neighbouring fibres, as expected from the conclusions of van den Heuvel et al. [456]. At these points, the jumps in opposite directions for D and G wavenumbers support an attribution to stresses of different nature (axial vs. radial). It is indeed a well established fact that graphite planes preferentially orientate along the longitudinal direction of high-performance carbon fibres [483,484]. The G wavenumber should thus be representative of the axial loading of the fibre. As for the D band, it corresponds to defective graphene, possibly the forming of C^2_{sp}–C^3_{sp} bonds where graphite nanocrystals transform into amorphous carbon. Such bonds located at the surface

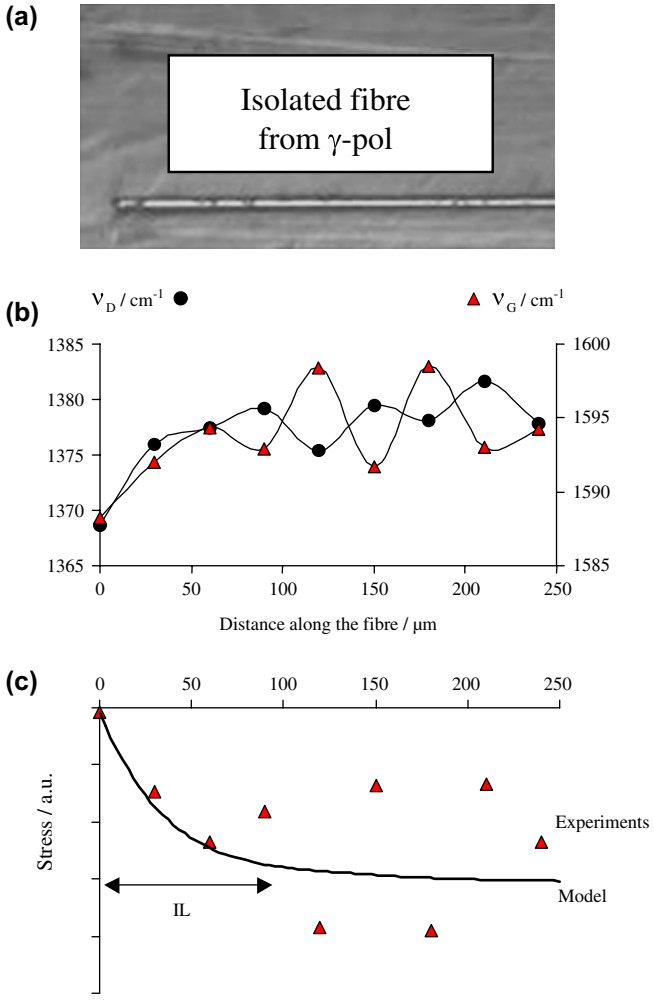

Fig. 23. (a) Optical micrograph of an IM7 fibre entering the matrix of "γ-pol" composite (see text) strained to 1%. (b) Wavenumber variations along the same fibre (origin at fibre tip, $\lambda_{laser} = 457.9$ nm, $P_{illumination} = 1.5$ mW). (c) Modelling of ν_G-derived axial compressive stress along the same fibre (IL, ineffective length) [485]. Reprinted from Ref. [485, pp. 646–651] with permission from Elsevier.

and in-between the graphite planes would be expected to be less specifically sensitive to the loading direction. In Fig. 23c the G wavenumbers have been converted into an axial compressive stress (σ_f) and the resulting data were fitted according to the following model [365]:

$$\sigma_f = -\sigma_{max}\frac{(1-\cosh(\beta((1/2)-x)))}{\cosh\left(\frac{\beta l}{2}\right)} - 3.7, \quad \beta = \frac{1}{r}\sqrt{\frac{E_m}{(1+\nu_m)E_f \ln\left(\frac{r_m}{r}\right)}} \tag{53}$$

where x is the position along the fibre of length l and radius r, σ_{max} is the maximum stress, ν_m is the matrix Poisson's ratio and E_f and E_m are the fibre and matrix Young's moduli, respectively.

As for r_m, it corresponds to the effective matrix thickness responsible for the fibre stress. A value $\beta \sim 0.03\ \mu m^{-1}$ gave the best fit and the variation in Fig. 23c shows the axial compression to rise from zero (at the tip) to its maximum value over a typical IL $\sim$100 μm.

5.4. ''Micro–Macro'' correlations

In this section, we will demonstrate how the local information accessed by RS through very simple spectra fittings correlates with ''macroscopic'' parameters such as Young's modulus, tensile strength and micro-hardness. The reason why such a correlation exists is the common dependence of the Raman signal and the mechanical behaviour on the micro/nanostructure of materials.

5.4.1. Comparison of Raman Spectra with micro-indentation results

Strong correlations between Raman and microhardness data have been reported by Gogotsi et al. [133,486] for semiconductors, quartz and carbon and by Amer et al. [487] for ''diamond-like carbon''. Fig. 24 illustrates how ''mechanical changes'' (Fig. 24c) are similarly related to a change of the Raman spectrum of either carbon or SiC nanoprecipitates (Fig. 24a and b) in an SCS-6 fibre.[36] The variations in Berkovich's micro-hardness (μH; three-sided diamond tip) and Young's modulus were measured by Mann et al. [489] and we highlighted different zones with vertical dots. From core to periphery, they correspond to:

(I) The 32-μm diameter carbon core consisting of graphitic units 1–5 nm in size [475].
(II) A 1.5-μm thick layer of pyrolytic carbon (grains are 25–50 nm in size). It has been identified as the weakest part of the fibre because its graphitic planes are parallel to the fibre axis [489].
(III) A zone in which carbon coexists with SiC and evolves over 30 μm towards a highly disordered carbon.
(IV) A zone where only SiC is detected (C–C bonds abundance $\leq 0.1\%$). The TO and LO band widening and the increase of the background level reveal stacking faults are all the more frequent as thickness increases [475]. In spite of this, the mechanical properties are constant, which suggests they are governed by free carbon in insertion.
(V) The interfacial carbon deposit (thickness 3 μm).

5.4.2. Comparison of Raman Spectra with fibre strength

Fig. 25 shows the correlation of the strength measured on NLM [370] and Hi-Nicalon [383] SiC fibres annealed at different temperatures (up to about 1500 °C) with their Raman spectra recorded at room-temperature. The linearity suggests that the macroscopic (strength measurement) and microscopic (Raman spectrum) responses to stress have the same dependence on grain size. A strength reduction resulting from grain boundary creeping is ruled out since it would not alter the Raman spectra. Two atmospheres were tested for the NLM grade. The mechanical failure is postponed in a reducing atmosphere but this does not seem to modify the ''micro–macro'' mechanical correlation.

[36] This is a 140-μm diameter fibre used for metal-matrix reinforcement [365]. It has a high heterogeneity along the radius, due to a preparation by CVD of SiC (and carbon), on a carbon core [488].

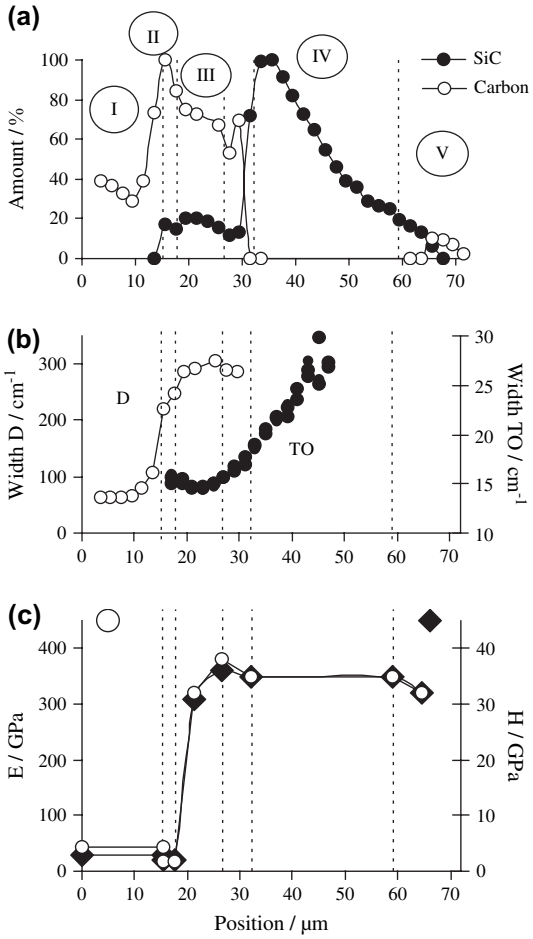

Fig. 24. (a) Raman detection of carbon (intensities of D, G and D' peaks are added) and SiC (intensities of TO and LO peaks are added) as a function of the position along the fibre radius ($\lambda_{laser} = 632.8$ nm). A 100% corresponds to the maximum intensity detected for each phase. (b) Bandwidths obtained after spectra fitting for D carbon peak ($\lambda_{laser} = 632.8$ nm) and SiC TO modes (three separate scans; $\lambda = 514.5$ nm). (c) Young's modulus and "Berkovich's hardness" (data from Mann et al [489]). Reprinted from Ref. [38, pp. 1249–1259] with permission from Elsevier.

5.4.3. Young's modulus and "Raman microextensometry"

At the macroscopic scale, fibres present the same tendency as their bonds to strengthen in compression and soften in tension [453]. Hooke's law being nothing but the macroscopic manif estation of bond stiffness, one may indeed expect to find a relationship linking E to k_b (introduced in Eq. (37)) via S^{ε}.

The simplest expression modelling a "realistic" bond potential $V(l_b)$ would be the following:

$$V(l_b) = \frac{k_b}{2}(l_b - l_0)^2 + \frac{k'_b}{6}(l_b - l_0)^3;\ k' < 0 \tag{54}$$

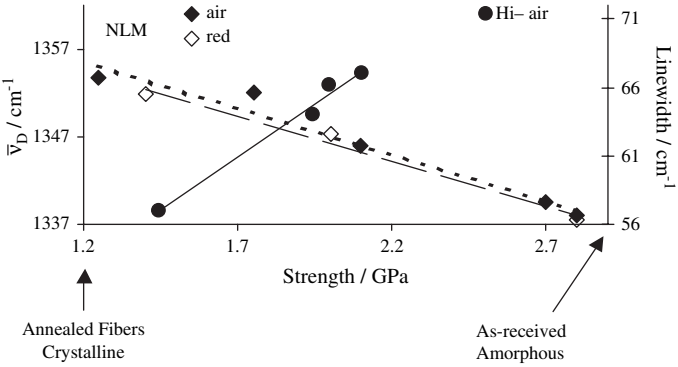

Fig. 25. Raman shift and linewidth of the carbon *D* mode ($\lambda = 514.5$ nm) plotted as a function of tensile strengths found in Berger et al. [383] or Kumagawa et al. [370] for heat-treated SiC fibres. Reprinted from Ref. [38, pp. 1249–1259] with permission from Elsevier.

With this form, the quasi-harmonic approximation (Eqs. (37) and (38)) leads to:

$$\overline{\nu}(l_b) \propto \sqrt{k_b \times \left(1 + \frac{k'_b}{k_b} \times (l_b - l_0)\right)} \tag{55}$$

where k'_b is expected to be much smaller than k so, as long as l_b remains close to l_0 (small strain assumption), a Taylor expansion is justified:

$$\overline{\nu}(l_b) \sim \sqrt{k_b} + \frac{k'_b}{\sqrt{k_b}} \times (l_b - l_0) \tag{56}$$

$$\overline{\nu}(l_{b_2}) - \overline{\nu}(l_{b_1}) \sim \frac{k'_b}{\sqrt{k_b}} \times (l_{b_2} - l_{b_1}) \tag{57}$$

Upon comparison with Eq. (50), this is equivalent to:

$$S^{\varepsilon}_b = \frac{k'_b l_0}{100\sqrt{k_b}} < 0 \tag{58}$$

Here again, we find that the energy shift for a strained bond can be expected to be proportional to the bond deformation. Besides, in such isotropic structures as most nanophased fibres are, the ''bond compression model'' predicts a Young's modulus in the following form [490]:

$$E = \sum_{\text{bonds}} \frac{l_b^2 k_b}{9} \tag{59}$$

For fibres with a single (or dominant) type of bonds, k_b and k'_b have unique values and, according to Eqs. (58) and (59), S^{ε}_b must then be proportional to $E^{-1/2}$ and the same will apply to S^{ε} (see discussion of Eqs. (49) and (50)). Fig. 26 plots S^{ε}_G coefficient measured in different carbon and ''first generation'' SiC fibres as a function of Young's modulus square root. The proportion and the distribution of the carbon and SiC phases differ in the fibres and, yet, a global classification is possible. Note that a direct proportionality between S^{ε} and E has been reported

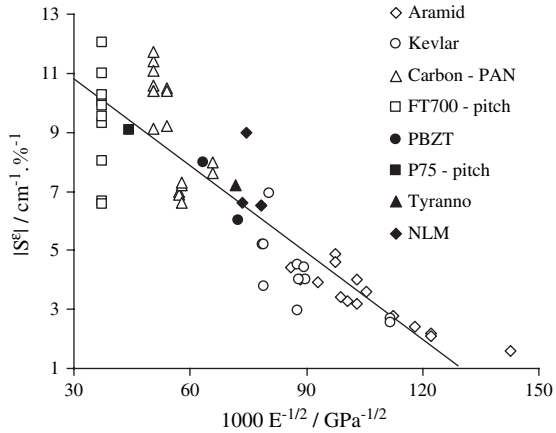

Fig. 26. Absolute value of the Raman Mechanical Coefficient (RMC) of the carbon G band plotted versus the inverse of Young's modulus square root. Reprinted from Ref. [38, pp. 1249–1259] with permission from Elsevier.

in the literature but these results were based on a narrower exploration of Young's Modulus, limited to aramid [447,467,491], polyethylene [492] or carbon [453] fibres. Deviations from the linear trend in Fig. 26 can be explained with the following arguments:

(i) A few of the S^{ε} values appearing in Fig. 26 were measured under compression and they are not necessarily comparable with those obtained through tensile straining. Indeed, the S^{ε} coefficients suppose a linear dependence of the Raman wavenumbers on the macroscopic deformation but a general relationship would rather be quadratic [450]:

$$\Delta\overline{\nu} = a\,\Delta\varepsilon + b(\Delta\varepsilon)^2 \tag{60}$$

S^{ε} is thus subject to change when passing from tensile to compressive stress. There is almost no effect ($b \sim 0$) for isotropic structures like SiC fibres with strong covalent bonds in all directions but Melanitis et al. [451] found $a/b \sim 5$ (only!) in "PAN-based" carbon fibres.

(ii) Not all S^{ε} values in Fig. 26 were obtained with the same laser line. Yet, carbon is a resonant species and both the spectrum and the penetration depth therefore depend on the actual wavelength. Most papers on Raman extensometry of carbon have neglected this aspect of the problem.

(iii) The reasoning that drove to Fig. 26 neglected the k_b and k'_b distributions in the material. This simplification is probably acceptable for carbon fibres but certainly not for SiC fibres (Tyranno and NLM grades), where C–C and C–SiC bonds coexist. For that matter, the second and third generation SiC fibres have such a specific behaviour that they were not even included in Fig. 26. In such fibres with small amorphous or crystalline particles, C–C bonds are largely outnumbered by Si–C and inter-particles bonds. The E_{fibre} (macroscopic scale) can no longer be considered as the counterpart of $S^{\varepsilon/\sigma}_{\text{particles}}$ (bond scale) [375].

Fig. 27 shows that the variations of Young's Modulus (the slope on the strain–stress curve) in a semi-crystalline polymer such as PET can be correlated with the Raman shifts of the low frequency contributions corresponding to the amorphous and crystalline substructures (see

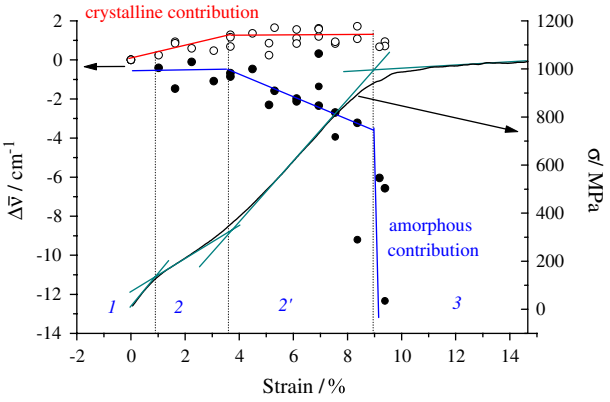

Fig. 27. Comparison of the strain dependency of the crystalline and amorphous low frequency Raman contributions (left hand scale) with the stress–strain tensile curve (right hand scale) for PET fibres. Reprinted from Ref. [172, pp. 2463–2475] with permission from Elsevier.

Fig. 5). In PET fibres, most of the stress is obviously transferred to the amorphous matrix, whereas nano-crystallites are only slightly compressed by a Poisson's effect. In polyamide fibres, both the amorphous and crystalline moieties accommodate the stress because the nanostructure puts them "in series". Wavenumber–strain curves then start with a plateau that corresponds to the disentanglement of the polymer chains (visco-elastic regime) and wavenumbers start downshifting as soon as "knots" block this process (elastic regime) [169–172].

5.5. CNTs used as nanometric stress gauges

On account of their very small dimension, the direct determination of CNTs Young's modulus is difficult. Most experimental values were obtained through manipulations with an AFM tip (see Table 4 in Ref. [493]) but Lourie and Wagner [494] demonstrated that an indirect measurement was possible using RS on "quenched" matrix-embedded nanotubes. Using a "concentric cylinders" modelling of each CNT and the surrounding matrix, they calculated the axial tube stress due to cooling by ΔT degrees and established an expression for nanotubes Young's modulus E_{NT}:

$$E_{NT} = \left[\frac{\Delta\alpha\,\Delta T}{\varepsilon_{NT}} - 1\right]\frac{(1-f_{NT})}{f_{NT}}E_m \tag{61}$$

where $\Delta\alpha$ is the difference in thermal expansion, f_{NT} is the volume fraction of nanotubes, E_m the Young's modulus of the matrix and ε_{NT} is the compressive strain. The latter was measured by the strain dependency of the D^* Raman band of SWCNTs, which allowed Young's modulus determination. Conversely, some authors filled composites matrices with nanotubes and used them to sense fibre stress in polymers [471,495,496].

References

[1] Ph. Colomban, Ceramics Int. 15 (1989) 23.
[2] Ph. Colomban, G. Sagon, X. Faurel, J. Raman Spectrosc. 32 (2001) 351.

[3] J. Pérez-Arantegui, J. Molera, A. Larrea, T. Pradell, M. Vendrell-Saz, I. Borgia, B.G. Brunetti, F. Cariati, P. Fermo, M. Mellini, A. Sgamellotti, C. Viti, J. Am. Ceram. Soc. 84 (2001) 442.
[4] Ph. Colomban, C. Truong, J. Raman Spectrosc. 35 (2004) 195.
[5] A.S. Edelstein, R.C. Cammarata (Eds.), Nanomaterials: Synthesis, Properties and Applications, CRC Press, Boca Raton, Fl, USA, 1998.
[6] National Research Council, Small Wonders, Endless Frontiers, National Academy Press, Washington, DC, USA, 2002.
[7] R.A. Andrievski, A.M. Glezer, Scripta Mater. 44 (2001) 1621.
[8] S.C. Tjong, H. Chen, Mater. Sci. Eng. R45 (1–2) (2004) 1.
[9] A.A. Sirenko, J.R. Fox, I.A. Akimov, X.X. Xi, S. Ruvimov, Z. Liliental-Weber, Sol. State Comm. 113 (2000) 553.
[10] M. Sternitzke, J. Eur. Ceram. Soc. 17 (1997) 1061.
[11] S. Gvasaliya, S. Lushnikov, B. Roessli, R. Katiyar, Ferroelectrics 302 (2004) 347.
[12] H.M. Jang, T.-Y. Kim, I.-W. Park, Sol. State Comm. 127 (2003) 645.
[13] M.P. Thi, G. March, Ph. Colomban, J. Eur. Ceram. Soc. 25 (14) (2005) 3335.
[14] M. Iwata, N. Tomisato, H. Orihara, N. Arai, N. Tanaka, H. Ohwa, N. Yasuda, Y. Ishibashi, Jap. J. Appl. Phys. 40 (2001) 5819.
[15] E. Stura, C. Nicolini, Analytica Chimica Acta 568 (2006) 57.
[16] E. Stathatos, P. Lianos, V. Jovanovski, B. Orel, J. Photochem. Photobio. 169 (2005) 57.
[17] National Research Council of the National Academies (AFSTB), Implications of Emerging Micro and Nanotechnology, The National Academies Press, Washington, DC, USA, 2002.
[18] U. Simon, M.E. Franke, Microporous Mesoporous Mater. 41 (1–3) (2000) 1.
[19] E. Rossinyol, J. Arbiol, F. Peiró, A. Cornet, J.R. Morante, B. Tian, T. Bo, D. Zhao, Sens. Actuators B109 (2005) 57.
[20] J.Y. Ying, A. Tschöpe, D. Levin, Nanostruct. Mater. 6 (1–4) (1995) 237.
[21] Y. Wang, Z. Tang, N.A. Kotov, Mater. Today 8 (2005) 20.
[22] G. Gouadec, Ph. Colomban, N.P. Bansal, J. Am. Ceram. Soc. 84 (2001) 1129.
[23] Ph. Colomban, G. Gouadec, L. Mazerolles, Mater. Corros. 53 (2002) 306.
[24] J.-P. Schnell, G. Velasco, D. Dubreuil, D. Dieumegard, M. Croset, Ph. Colomban, Solid State Ionics 9/10 (1983) 1465.
[25] U. Lavrencic-Stangar, B. Orel, N. Groselj, Ph. Colomban, E. Statthatos, P. Lianos, J. Electrochem. Soc. 149 (11) (2002) E413.
[26] A. Surca-Vuk, U. Opara-Krasovec, B. Orel, Ph. Colomban, J. Electrochem. Soc. 148 (2002) H49.
[27] A. Surca-Vuk, B. Orel, G. Drazic, Ph. Colomban, in: H. Hofman, et al. (Eds.), Nanostruct. Mater. 153, 2002 (Springer, Wien).
[28] A. Cabot, A. Diéguez, A. Romano-Rodriguez, J.R. Morante, N. Barsan, Sensors and Actuators B79 (2001) 98.
[29] P. Cassoux, D. de-Caro, L. Valade, H. Casellas, S. Roques, J.-P. Legros, Synth. Mater. 133–134 (2003) 659.
[30] G.J. Fang, K.-L. Yao, Z.-L. Liu, Thin Solid Films 394 (2001) 64.
[31] V.V. Poborchii, Solid State Comm. 107 (1998) 513.
[32] Z. Wang, V. Pischedda, S.K. Saxena, P. Lazor, Solid State Comm. 121 (2002) 275.
[33] J.C. Rodríguez-Cabello, L. Quintanilla, J.M. Pastor, J. Raman Spectrosc. 25 (1994) 335.
[34] S. Bandow, Y. Maruyama, X.-X. Bi, R. Ochoa, J.M. Holden, W.-T. Lee, P.C. Eklund, Mater. Sci. Eng. A204 (1995) 222.
[35] X. Li, W. Chen, C. Bian, J. He, N. Xu, G. Xue, Appl. Surf. Sci. 217 (2003) 16.
[36] A.G. Kalampounias, D.T. Kastrissios, S.N. Yannopoulos, J. Non-Cryst. Sol. 326&327 (2003) 115.
[37] Ph. Colomban, Mater. Sci. Forum 453–454 (2004) 269.
[38] G. Gouadec, Ph. Colomban, J. Eur. Ceram. Soc. 21 (2001) 1249.
[39] Ph. Colomban, Spectrosc. Eur. 15 (2003) 8.
[40] A.K. Arora, M. Rajalakshmi, T.R. Ravindran, in: H.S. Nalwa (Ed.), Encyclopedia of Nanoscience and Nanotechnology, 499, American Scientific Publishers, 2004.
[41] A. Singha, P. Dhar, A. Roy, Am. J. Phys. 73 (2005) 224.
[42] W.B. White, J. Ceram. Process. Res. 6 (2005) 1.
[43] Z.V. Popovic, Z. Dohcevic-Mitrovic, M. Stepanovic, M. Grujic-Brojcin, Nanopowders Characterization using the vibrational spectroscopy methods, in: Proceedings of the First International Workshop on Nanoscience & Nanotechnology, Belgrade, Serbia and Montenegro, vol. 88, 2005.
[44] W. Kiefer, G. Gouadec, Ph. Colomban (Eds.), Special Issue on the Raman Study of Nanomaterials, J. Raman Spectrosc. 39, 2007.
[45] C. Kittel, Introduction to Solid State Physics, seventh ed., John Wiley and Sons, NY, 1996.

[46] I.R. Lewis, H.G.M. Edwards (Eds.), Handbook of Raman Spectroscopy – From the Research Laboratory to the Process Line, Marcel Dekker Inc., NY, USA, 2001.
[47] D.A. Long, Raman Spectroscopy, McGraw-Hill, New York (1977).
[48] R. Yakimova, T. Paskova, I. Ivanov, K. Germanova, M. Peev, Sci. Technol. 8 (1993) 179.
[49] H. Shen, F.H. Pollak, Appl. Phys. Lett. 45 (1984) 692.
[50] Ph. Colomban (Ed.), Proton Conductors. Solids, Membranes and Gels – Materials and Devices, 329, Cambridge University Press, Cambridge, U.K., 1992.
[51] M. Bee, Chem. Phys. 292 (2–3) (2003) 121.
[52] H. Poulet, J.P. Mathieu, Vibration Spectra and Symmetry of Crystals, Gordon and Breach, New York, 1976.
[53] W. Hayes, G.F. Hopper, F.L. Pratt, J. Phys. C: Solid State Phys. 15 (1982) L675.
[54] M.J. Delaney, S. Ushioda, Sol. State Comm. 19 (1976) 297.
[55] Ph. Colomban, G. Lucazeau, J. Chem. Phys. 72 (1980) 1213.
[56] Ph. Colomban, R. Mercier, G. Lucazeau, J. Chem. Phys. 75 (1981) 1388.
[57] K. Funke, R.D. Banhatti, S. Brückner, C. Cramer, C. Krieger, A. Mandanici, C. Martiny, I. Ross, Phys. Chem. Chem. Phys. 4 (2002) 3155.
[58] K. Funke, in: P. Hagenmuller, W. van Gool (Eds.), Solid Electrolytes. General Principles, Characterization, Materials, Applications, vol. 77, Academic Press, New York, 1978.
[59] X. Faurel, A. Vanderperre, Ph. Colomban, J. Raman Spectrosc. 34 (2003) 290.
[60] Ph. Colomban, J. Raman Spectrosc. 34 (2003) 420.
[61] Ph. Colomban (Chapter 13), in: H.G.M. Edwards, J.M. Chalmers (Eds.), Raman Spectroscopy in Archaeology and Art History, 192, Royal Society of Chemistry, U.K., 2004.
[62] B.-K. Kim, J.-W. Hahn, K.R. Han, J. Mater. Sci. Lett. 16 (1997) 669.
[63] L.M. Fraas, S.P.S. Porto, E. Loh, Sol. State Comm. 8 (1970) 803.
[64] M.V. Abrashev, M.N. Iliev, Phys. Rev. B 45 (14) (1992) 8046.
[65] C. Thomsen, M. Cardona, in: D.M. Ginzberg (Ed.), Physical Properties of High Temperature Superconductors I, vol. 409, World Scientific, Singapore, 1989.
[66] P. D'Arco, B. Piriou, Amer. Miner. 74 (1989) 191.
[67] G. Gouadec, Ph. Colomban, N. Piquet, M.-F. Trichet, L. Mazerolles, J. Eur. Ceram. Soc. 25 (2005) 1447.
[68] G. Turrell, J. Corset (Eds.), Raman Microscopy. Developments and Applications, Academic Press, London, 1996.
[69] A. Paipetis, C. Vlattas, C. Galiotis, J. Raman Spectrosc. 27 (1996) 519.
[70] Renishaw Spectroscopy Products Division, Drug Detection using Raman Spectroscopy – Simple, Rapid Identification and Characterisation of Illicit Substances, AN/097, 2004.
[71] L. Rayleigh, Phil. Mag. 8 (1879) 261.
[72] M. Born, E. Wolf, Principles of Optics, Pergamon Press, Oxford, 1985 441.
[73] A.E. Conrady, Applied Optics and Optical Design, Part 2, Dover Publications 627, 1960.
[74] N.T. Goldsmith, Image Anal. Stereol. 19 (2000) 163.
[75] M. Havel, Ph. Colomban, Microsc. Anal. 20 (2006) 13.
[76] C.H. Shek, G.M. Lin, J.K. Lai, Nanostruct. Mater. 11 (1999) 831.
[77] H. Kuzmany, P. Knoll, Mol. Cryst. Liq. Cryst. 117 (1985) 385.
[78] J. Kürti, H. Kuzmany, Phys. Rev. B 44 (1991) 597.
[79] Ph. Colomban, Ceram. Trans. 103 (2000) 517.
[80] D. Routkevich, T.L. Haslett, L. Ryan, T. Bigioni, C. Douketis, M. Moskovits, Chem. Phys. 210 (1996) 343.
[81] C. Raptis, D. Nesheva, Y.C. Boulmetis, Z. Levi, Z. Aneva, J. Phys.: Condens. Matter 16 (2004) 8221.
[82] S. Folch, A. Regis, A. Gruger, Ph. Colomban, Synth. Metals 110 (2000) 219.
[83] J. Godlewski, P. Bouvier, G. Lucazeau, L. Fayette, ASTM STP 1354 (2000) 877.
[84] G. Lucazeau, Quelques Exemples d'Application de la Spectroscopie Raman en Physique et en Chimie du Solide, in: Proc. ''Ecole Thématique de Spectroscopie Raman en Chimie et Physique des Matériaux'', Autrans, France, 1998.
[85] P. Bouvier, Mesures de Contraintes dans des Couches d'Oxydation d'Alliages de Zirconium, in: Proc. ''Ecole Thématique de Spectroscopie Raman en Chimie et Physique des Matériaux'', Autrans, France, 1998.
[86] A. El-Khalki, A. Gruger, Ph. Colomban, Synth. Metals 139 (2003) 215.
[87] Ph. Colomban, S. Folch, A. Gruger, Macromolecules 32 (1999) 3080.
[88] G. Gouadec, S. Karlin, Ph. Colomban, Composites B 29 (1998) 251.
[89] I. De Wolf, J. Raman Spectrosc. 30 (10) (1999) 877.
[90] G. Gouadec, Ph. Colomban, N.P. Bansal, J. Am. Ceram. Soc. 84 (2001) 1136.
[91] Y.K. Kim, H.M. Jang, J. Phys. Chem. Solids 64 (2003) 1271.
[92] S. Loridant, G. Lucazeau, T. Le-Bihan, J. Phys. Chem. Solids 63 (2002) 1983.

[93] M.N. Iliev, M.V. Abrashev, H.-G. Lee, V.N. Popov, Y.Y. Sun, C. Thomsen, R.L. Meng, C.W. Chu, Phys. Rev. B 57 (1998) 2872.
[94] D.G. Georgiev, P. Boolchand, K.A. Jackson, Phil. Mag. 83 (25) (2003) 2941.
[95] W.P. Griffith, J. Chem. Soc. (A) (1970) 286.
[96] W.P. Griffith, Nature 224 (1969) 264.
[97] W.P. Griffith, J. Chem. Soc. (A) (1969) 1372.
[98] P. Gillet, V. Sautter, J. Harris, B. Reynard, B. Harte, M. Kuntz, Am. Miner. 87 (2002) 312.
[99] T. Chaplin, G.D. Price, N.L. Ross, Am. Miner. 83 (1998) 841.
[100] D.N. Argyriou, H.N. Bordallo, B.J. Campbell, A.K. Cheetham, D.E. Cox, J.S. Gardner, K. Hanif, A. dos Santos, G.F. Strouse, Phys. Rev. B 22 (2000) 15269.
[101] L.-G. Hwa, S.-L. Hwang, L.-C. Liu, J. Non-Cryst. Sol. 238 (1998) 193.
[102] W.P. Griffith, in: J.C. Carr (Ed.), Infrared and Raman Spectroscopy of Lunar and Terrestrial Minerals, 299, Academic Press, New York, 1975.
[103] K. Nakamoto, Infrared and Raman Spectra of Inorganic and Coordination Compounds, John Wiley and Sons, New York, 1986.
[104] A. Otto, J. Raman Spectrosc. 22 (1991) 743.
[105] T.M. Cotton, J.-H. Kim, G.D. Chumanov, J. Raman Spectrosc. 22 (1991) 729.
[106] J. Zhang, X. Li, X. Sun, Y. Li, J. Phys. Chem. B 109 (2005) 12544.
[107] J.-L. Yao, J. Tang, D.-Y. Wu, D.-M. Sun, K.-H. Xue, B. Ren, B.-W. Mao, Z.-Q. Tian, Surface Sci. 514 (2002) 108.
[108] W. Kiefer, Z.-Q. Tian (Eds.), J. Raman Spectrosc. 36 (6–7) (2005) (Special Issue on Surface Enhanced Raman Spectroscopy).
[109] M.P. Thi, Chem. Phys. Lett. 115 (1985) 130.
[110] S. Bernad, T. Soulimane, S. Lecomte, J. Raman Spectrosc. 35 (2003) 47.
[111] M. Roy, V.C. George, A.K. Dua, P. Raj, S. Schulze, D.A. Tenne, G. Salvan, D.R.T. Zahn, Diamond Relat. Mater. 11 (2002) 1858.
[112] D. Roy, Z.H. Barber, T.W. Clyne, J. Appl. Phys. 91 (2002) 6085.
[113] J. Azoulay, A. Débarre, A. Richard, P. Tchénio, S. Bandow, S. Iijima, Chem. Phys. Lett. 331 (2000) 347.
[114] E.A. Ash, G. Nichols, Nature 237 (1972) 510.
[115] D.P. Tsai, A. Othonos, M. Moskovits, Appl. Phys. Lett. 64 (1994) 1768.
[116] B. Hecht, B. Sick, U.P. Wild, V. Deckert, R. Zenobi, O.J.F. Martin, D.W. Pohl, J. Chem. Phys. 112 (18) (2000) 7761.
[117] D.W. Pohl, W. Denk, M. Lanz, Appl. Phys. Lett. 44 (1984) 651.
[118] U. Dürig, D.W. Pohl, F. Rohner, J. Appl. Phys. 59 (10) (1986) 3318.
[119] P.G. Gucciardi, S. Trusso, C. Vasi, S. Patane, M. Allegrini, Optics 42 (15) (2003) 2724.
[120] C.L. Jahncke, H.D. Hallen, M.A. Paesler, J. Raman Spectrosc. 27 (1996) 579.
[121] H.D. Hallen, C.L. Jahncke, J. Raman Spectrosc. 34 (2003) 655.
[122] D.A. Smith, S. Webster, M. Ayad, S.D. Evans, D. Fogherty, D. Batchelder, Ultramicroscopy 61 (1995) 247.
[123] S. Webster, D.A. Smith, D.N. Batchelder, S. Karlin, Synthetic Metals 102 (1–3) (1999) 1425.
[124] A. Hartschuh, N. Anderson, L. Novotny, J. Microscopy 210 (Pt 3) (2003) 234.
[125] W.X. Sun, Z.X. Shen, Mater. Phys. Mech. 4 (2001) 17.
[126] W.X. Sun, Z.X. Shen, J. Raman Spectrosc. 34 (2003) 668.
[127] D. Richards, R.G. Milner, F. Huang, F. Festy, J. Raman Spectrosc. 34 (2003) 663.
[128] A. Hartschuh, M.R. Beversluis, A. Bouhelier, L. Novotny, Phil. Trans. Roy. Soc. Lond. A362 (2004) 807.
[129] B.E. Sernelius, Surface Modes in Physics, Wiley-VCH, Berlin, 2001.
[130] B. Cao, W. Cai, G. Duan, Y. Li, Q. Zhao, D. Yu, Nanotechnology 16 (2005) 2567.
[131] K.N. Yu, Y. Xiong, Y. Liu, C. Xiong, Phys. Rev. B 55 (1997) 2666.
[132] H.C. Choi, Y.M. Jung, S.B. Kim, Vibr. Spectrosc. 37 (2005) 33.
[133] A. Kailer, K.G. Nickel, Y.G. Gogotsi, J. Raman Spectrosc. 30 (1999) 939.
[134] G.S. Cheng, S.H. Chen, X.G. Zhu, Y.Q. Mao, L.D. Zhang, Mater. Sci. Eng. A 286 (2000) 165.
[135] R.J.K. Wood, D.W. Wheeler, D.C. Lejeau, B.G. Mellor, Wear 233–235 (1999) 134.
[136] K.-H. Lee, H. Sugimura, Y. Inoue, O. Takai, Thin Solid Films 435 (2003) 150.
[137] V.V. Guliants, S.A. Holmes, J.B. Benziger, P. Heaney, D. Yates, I.E. Wachs, J. Mol. Catal. A172 (2001) 265.
[138] H. Chen, X. Zhou, C. Ding, J. Eur. Ceram. Soc. 23 (2003) 1449.
[139] S.-K. Lee, G.-J. Choi, U.-Y. Hwang, K.-K. Koo, T.-J. Park, Mater. Lett. 57 (2003) 2201.
[140] M.-S. Zhang, J. Yu, W.-C. Chen, Z. Yin, Progr. Crystal Growth Charact. Mater. (2000) 33.
[141] S.K. Tadokoro, E.N.S. Muccillo, J. Alloys Compd. 344 (2002) 186.
[142] D.W. Zeng, C.S. Xie, B.L. Zhu, W.L. Song, Mater. Lett. 58 (3–4) (2004) 312.

[143] T. Zeng, Y. Qiu, L. Chen, X. Song, Mater. Chem. Phys. 56 (1998) 163.
[144] P. Thangadurai, S. Ramasamy, R. Kesavamoorthy, J. Phys. Cond. Matter 17 (2005) 863.
[145] Y. Yang, C. Wang, J. Hou, J. Dai, Mater. Lett. 57 (2003) 2185.
[146] P. Durán, F. Capel, J. Tartaj, D. Gutierrez, C. Moure, Solid State Ionics 141–142 (2001) 529.
[147] Z. Wang, S.K. Saxena, Solid State Comm. 118 (2001) 75.
[148] M. Boulova, G. Lucazeau, J. Solid State Chem. 167 (2002) 425.
[149] J.F. Meng, R.S. Katiyar, G.T. Zou, J. Phys. Chem. Solids 59 (6–7) (1998) 1161.
[150] K.C.V. Lima, A.G. de Souza Filho, A.P. Ayala, J.M. Filho, P.T.C. Freire, F.E.A. Melo, E.B. Araujo, J.A. Eiras, Phys. Rev. B 63 (18) (2001) 41051.
[151] R.E. Melgarejo, M.S. Tomar, S. Bhaskar, P.S. Dobal, R.S. Katiyar, Appl. Phys. Lett. 81 (14) (2002) 2611.
[152] Z. Wang, S.K. Saxena, Solid State Comm. 123 (2002) 195.
[153] A. Trovarelli, F. Zamar, J. Llorca, C. de-Leitenburg, G. Dolcetti, J.T. Kiss, J. Catal. 169 (1997) 490.
[154] E. Djurado, P. Bouvier, G. Lucazeau, J. Solid State Chem. 149 (2000) 399.
[155] P. Bouvier, J. Godlewski, G. Lucazeau, J. Nucl. Mater. 300 (2002) 118.
[156] P. Bouvier, G. Lucazeau, J. Phys. Chem. Solids 61 (2000) 569.
[157] E. Barborini, I.N. Kholmanov, P. Piseri, C. Ducati, C.E. Bottani, P. Milani, Appl. Phys. Lett. 81 (16) (2002) 3052.
[158] M.H. Frey, D.A. Payne, Phys. Rev. B 54 (1996) 3158.
[159] M.V. Abrashev, V.G. Ivanov, M.N. Iliev, R.A. Chakalov, R.I. Chakalova, C. Thomsen, Phys. Stat. Sol. (b) 215 (1999) 631.
[160] R.C. Garvie, J. Phys. Chem. 69 (1965) 1238.
[161] T. Furukawa, W.B. White, J. Non-Cryst. Sol. 38 & 39 (1980) 87.
[162] Y. Wang, K. Tanaka, T. Nakaoka, K. Murase, Physica B 316–317 (2002) 568.
[163] M. Mortier, A. Monteville, G. Patriarche, G. Mazé, F. Auzel, Opt. Mater. 16 (2001) 255.
[164] Ph. Colomban, J. Raman Spectrosc. 27 (1996) 747.
[165] Ph. Colomban, Ceram. Eng. Sci. Proc. 21 (2000) 143.
[166] A. Guinier, Théorie et Technique de la Radiocristallographie, Dunod, Paris, 1956.
[167] Y. Guinet, T. Denicourt, A. Hedoux, M. Descamps, J. Mol. Struct. 651–653 (2003) 507.
[168] D. Roy, M. Chhowalla, H. Wang, N. Sano, I. Alexandrou, T.W. Clyne, G.A.J. Amaratunga, Chem. Phys. Lett. 373 (2003) 52.
[169] J.-M. Herrera-Ramirez, Ph. Colomban, A. Bunsell, J. Raman Spectrosc. 35 (12) (2004) 1063.
[170] A. Marcellan, A.R. Bunsell, R. Piques, Ph. Colomban, J. Mater. Sci. 38 (2003) 2117.
[171] A. Marcellan, Ph. Colomban, A. Bunsell, J. Raman Spectrosc. 35 (2004) 308.
[172] Ph. Colomban, J.M. Herrera-Ramirez, R. Paquin, A. Marcellan, A. Bunsell, Eng. Fract. Mech. 73 (16) (2006) 2463.
[173] B.H. Stuart, Vibr. Spectrosc. 10 (1996) 79.
[174] C.C.C. Lesko, J.F. Rabolt, R.M. Ikeda, B. Chase, A. Kennedy, J. Molec. Struct. 521 (2000) 127.
[175] E. Bustarret, M.A. Hachicha, M. Brunel, Appl. Phys. Lett. 52 (20) (1988) 1675.
[176] M.F. Cerqueira, L. Rebouta, M. Andritschky, J.A. Ferreira, M.F. Da-Silva, Vacuum 46 (12) (1995) 1385.
[177] D.G. Georgiev, M. Mitkova, P. Boolchand, G. Brunklaus, H. Eckert, M. Micoulaut, Phys. Rev. B 64 (2001) 134204.
[178] Y. Wang, J. Wells, D.G. Georgiev, P. Boolchand, K. Jackson, M. Micoulaut, Phys. Rev. Lett. 87 (18) (2001) 185503.
[179] H. Richter, Z.P. Wang, L. Ley, Solid State Comm. 39 (1981) 625.
[180] R. Carles, A. Mlayah, M.B. Amjoud, A. Reynes, R. Morancho, Jap. J. Appl. Phys. 31 (pt 1) (1992) 3511.
[181] S. Rohmfeld, M. Hundhausen, L. Ley, Phys. Stat. Sol. (b) 215 (1999) 115.
[182] P. Parayanthal, F.H. Pollak, Phys. Rev. Lett. 52 (20) (1984) 1822.
[183] A. Fischer, L. Anthony, A.D. Compaan, Appl. Phys. Lett. 72 (20) (1998) 2559.
[184] M. Fujii, S. Hayashi, K. Yamamoto, Jap. J. Appl. Phys. 30 (1991) 687.
[185] W.F. Zhang, Y.L. He, M.S. Zhang, Z. Yin, Q. Chen, J. Phys. D33 (2000) 912.
[186] J.W. Ager III, D.K. Veirs, G.M. Rosenblatt, Phys. Rev. B 43 (1991) 6491.
[187] R.J. Nemanich, S.A. Solin, R.M. Martin, Phys. Rev. B 23 (12) (1981) 6348.
[188] A.C. Ferrari, J. Robertson, Phys. Rev. B 61 (20) (2000) 14095.
[189] S. Hofmann, C. Ducati, R.J. Neil, S. Piscanec, A.C. Ferrari, J. Geng, R.E. Dunin-Borkovski, J. Robertson, J. Appl. Phys. 94 (2003) 6005.
[190] Y.K. Kim, H.M. Jang, Solid State Comm. 127 (2003) 433.
[191] B. Li, D. Yu, S.-L. Zhang, Phys. Rev. B 59 (1999) 1645.
[192] Q. Xiong, R. Gupta, K.W. Adu, E.C. Dickey, G.D. Lian, D. Tham, J.E. Fischer, P.C. Eklund, J. Nanosci. Nanotech. 3 (2003) 335.

[193] I.H. Campbell, P.M. Fauchet, Solid State Comm. 58 (10) (1986) 739.
[194] J. Zi, H. Büscher, C. Falter, W. Ludwig, K. Zhang, X. Xie, Appl. Phys. Lett. 69 (1996) 200.
[195] M.I. Vasilevskiy, A.G. Rolo, M.J.M. Gomes, Solid State Comm. 104 (1997) 381.
[196] I. Kosacki, T. Suzuki, V. Petrovsky, H.U. Anderson, Ph. Colomban, Solid State Ionics 149 (1–2) (2002) 99.
[197] W.H. Weber, K.C. Hass, J.R. McBride, Phys. Rev. B 48 (1993) 178.
[198] K.K. Tiong, P.M. Amirtharaj, F.H. Pollak, D.E. Aspnes, Appl. Phys. Lett. 44 (1984) 122.
[199] F. Tuinstra, J.L. Koenig, J. Chem. Phys. 53 (1970) 1126.
[200] F. Maury, R. Carles, G. Landa, B. Renucci, Thin Solid Films 155 (1987) 331.
[201] J. Zi, K. Zhang, X. Xie, Phys. Rev. B 55 (15) (1997) 9263.
[202] G.D. Mahan, R. Gupta, Q. Xiong, C.K. Adu, P.C. Eklund, Phys. Rev. B 68 (2003) 073402.
[203] A. Tanaka, S. Onari, T. Arai, Phys. Rev. B 45 (12) (1992) 6587.
[204] V. Paillard, P. Puech, M.A. Laguna, R. Carles, B. Kohn, F. Huisken, J. Appl. Phys. 86 (1999) 1921.
[205] J. Zuo, C. Xu, Y. Liu, Y. Quian, Nanostruct. Mater. 10 (1998) 1331.
[206] R.S. Chen, C.C. Chen, Y.S. Huang, C.T. Chia, H.P. Chen, D.S. Tsai, K.K. Tiong, Sol. State Comm. 131 (2004) 349.
[207] J. Zuo, C. Xu, B. Hou, C. Wang, Y. Xie, Y. Quian, J. Raman Spectrosc. 27 (1996) 921.
[208] S. Rohmfeld, M. Hundhausen, L. Ley, Phys. Rev. B 58 (15) (1998) 9858.
[209] M. Havel, PhD Thesis, Imageries Raman et Rayleigh de Nanophases, Nouveaux Outils pour l'Etude de la Corrosion de Matériaux Hétérogènes, University of Paris 6-P & M. Curie, 2004.
[210] L. Bergman, M.D. Bremser, W.G. Perry, R.F. Davis, M. Dutta, R.J. Nemanich, Appl. Phys. Lett. 71 (15) (1997).
[211] A.K. Arora, T.R. Ravindran, G.L.N. Reddy, A.K. Sikder, D.S. Misra, Diamond Relat. Mater. 10 (2001) 1477.
[212] M. Havel, D. Baron, Ph. Colomban, J. Mater. Sci. 39 (20) (2004) 6183.
[213] M. Havel, Ph. Colomban, J. Raman Spectrosc. 34 (10) (2003) 786.
[214] M. Havel, Ph. Colomban, Comp. Sci. Technol. 65 (3–4) (2005) 353.
[215] J.E. Spanier, R.D. Robinson, F. Zhang, S.-W. Chan, I.P. Herman, Phys. Rev. B 64 (2001) 2450407.
[216] W.K. Choi, Y.W. Ho, V. Ng, Mater. Phys. Mech. 4 (2001) 46.
[217] M. Ivanda, K. Babocsi, C. Dem, M. Schmitt, M. Montagna, W. Kiefer, Phys. Rev. B 67 (2003) 235329.
[218] A.V. Gomonnai, Y.M. Azhniuk, V.O. Yukhymchuk, M. Kranjcec, V.V. Lopushansky, Phys. Stat. Sol. (b) 239 (2003) 490.
[219] Y. Yan, S.-L. Zhang, S. Fan, W. Han, G. Meng, L. Zhang, Solid State Comm. 126 (2003) 649.
[220] L. Zhang, H.-J. Xie, C.-Y. Chen, Eur. Phys. J. B 27 (2002) 577.
[221] Q. Xiong, J. Wang, O. Reese, L.C. Lew-Yan-Voon, P.C. Eklund, NanoLetters 4 (10) (2004) 1991.
[222] A. Roy, A.K. Sood, Phys. Rev. B 53 (18) (1996) 12127.
[223] M.C. Klein, F. Hache, D. Ricard, C. Flytzanis, Phys. Rev. B 42 (17) (1990) 11123.
[224] S. Hayashi, H. Kanamori, Phys. Rev. B 26 (12) (1982) 7079.
[225] V.A. Fonoberov, A.A. Balandin, J. Phys. Cond. Matter 17 (2005) 1085.
[226] R. Ruppin, J. Phys. C Solid State Phys. 8 (1975) 1969.
[227] S. Hayashi, R. Ruppin, J. Phys. C Solid State Phys. 18 (1985) 2583.
[228] R. Ruppin, R. Englman, Rep. Prog. Phys. 33 (1970) 149.
[229] J. Xu, G. Cheng, W. Yang, Y. Du, J. Phys. B At. Mol. Opt. Phys. 29 (1996) 6227.
[230] F. Comas, C. Trallero-Giner, J. Appl. Phys. 94 (2003) 6023.
[231] J.P. Sun, H.B. Teng, G.I. Haddad, M.A. Stroscio, Semicond. Sci. Technol. 13 (1998) A147.
[232] N. Mori, T. Ando, Phys. Rev. B 40 (1989) 6175.
[233] E. Roca, C. Trallero-Giner, M. Cardona, Phys. Rev. B 49 (19) (1994) 13704.
[234] T.D. Krauss, F.W. Wise, D.B. Tanner, Phys. Rev. Lett. 76 (1996) 1376.
[235] S. Nomura, T. Kobayashi, Phys. Rev. B 45 (1992) 1305.
[236] E. Menéndez, C. Trallero-Giner, M. Cardona, Phys. Stat. Sol. (b) 199 (1997) 81.
[237] X. Hu, J. Zi, J. Phys. Cond. Matter 14 (2002) L671.
[238] D. Alexson, L. Bergman, M. Dutta, K.W. Kim, S. Komirenko, R.J. Nemanich, B.C. Lee, M.A. Stroscio, S. Yu, Physica B 263–264 (1999) 510.
[239] I.M. Tiginyanu, A. Sarua, G. Irmer, J. Monecke, S.M. Hubbard, D. Pavlidis, V. Valiaev, Phys. Rev. B 64 (2001) 233317.
[240] Y.A. Pusep, M.T.O. Silva, J.C. Galzerani, N.T. Moshegov, P. Basmaji, Phys. Rev. B 58 (16) (1998) 10683.
[241] M.I. Vasilevskiy, A.G. Rolo, M.J.M. Gomes, O.V. Vikhrova, C. Ricolleau, J. Phys. Cond. Matter 13 (14) (2001) 3491.
[242] K. Ushizawa, M.N. Gamo, K. Watanabe, I. Sakaguchi, Y. Sato, T. Ando, J. Raman Spectrosc. 30 (1999) 957.
[243] P. Gonon, E. Gheeraert, A. Deneuville, F. Fontaine, L. Abello, G. Lucazeau, J. Appl. Phys. 78 (12) (1995) 7059.
[244] S. Nakashima, H. Harima, Phys. Stat. Sol. (a) 162 (39) (1997) 39.

[245] M. Park, V. Sakhrani, J.-P. Maria, J.J. Cuomo, C.W. Teng, J.F. Muth, M.E. Ware, B.J. Rodriguez, R.J. Nemanich, J. Mater. Res. 18 (2003) 768.
[246] R. Meyer, L.J. Lewis, S. Prakash, P. Entel, Phys. Rev. B 68 (2003) 104303.
[247] H. Lamb, Proc. London Math. Soc. 13 (1882) 189.
[248] H. Portalès, PhD Thesis, Etude par Diffusion Raman de Nanoparticules Métalliques en Matrice Diélectrique Amorphe, University of Lyon 1, Claude Bernard, 2001.
[249] A. Tamura, K. Higeta, T. Ichinokawa, J. Phys. C Solid State Phys. 15 (1982) 4975.
[250] K.R. Patton, M.R. Geller, Phys. Rev. B 67 (2003) 155418.
[251] L. Saviot, D.B. Murray, Phys. Stat. Sol. (c) 1 (11) (2004) 2634.
[252] J.A. Lobo, Phys. Rev. D 52 (1995) 591.
[253] D.A. Mazurenko, PhD Thesis, Ultrafast Optical Switching in Three-Dimensional Photonic Crystals, Chapter 7, Coherent Vibrations of Submicron Gold Shells, University of Utrecht, 2004.
[254] A. Tanaka, S. Onari, T. Arai, Phys. Rev. B 47 (1993) 1237.
[255] M. Talati, P.K. Jha, Physica E 28 (2005) 171.
[256] P. Verma, W. Cordts, G. Irmer, J. Monecke, Phys. Rev. B 60 (1999) 5778.
[257] R.S. Cataliotti, G. Compagnini, A. Morresi, M. Ombelli, P. Sassi, Phys. Chem. Chem. Phys. 4 (2002) 2774.
[258] E. Duval, L. Saviot, A. Mermet, D.B. Murray, J. Phys. Cond. Matter 17 (2005) 3559.
[259] E. Duval, Phys. Rev. B 46 (1992) 5795.
[260] M. Montagna, R. Dusi, Phys. Rev. B 52 (14) (1995) 10080.
[261] E. Duval, A. Boukenter, B. Champagnon, Phys. Rev. Lett. 56 (19) (1986) 2052.
[262] A. Tamura, T. Ichinokawa, J. Phys. C Solid State Phys. 16 (1983) 4779.
[263] P. Gangopadhyay, R. Kesavamoorthy, K.G.M. Nair, R. Dhandapani, J. Appl. Phys. 88 (2000) 4975.
[264] M. Ferrari, F. Gonella, M. Montagna, C. Tosello, J. Appl. Phys. 79 (1996) 2055.
[265] M. Ferrari, F. Gonella, M. Montagna, C. Tosello, J. Raman Spectrosc. 27 (1996) 793.
[266] R. Govindaraj, R. Kesavamoorthy, R. Mythili, B. Viswanathan, J. Appl. Phys. 90 (2001) 958.
[267] A. Gajovic, M. Stubicar, M. Ivanda, K. Furic, J. Molec. Struct. 563–564 (2001) 315.
[268] A. Turkovic, M. Ivanda, S. Popovic, A. Tonejc, M. Gotic, P. Dubcek, S. Music, J. Molec. Struct. 410–411 (1997) 271.
[269] M. Gotic, M. Ivanda, A. Sekulic, S. Music, S. Popovic, A. Turkovic, K. Furic, Mater. Lett. 28 (1996) 225.
[270] M. Fujii, Y. Kanzawa, S. Hayashi, K. Yamamoto, Phys. Rev. B 54 (12) (1996) R8373.
[271] F. Liu, L. Liao, G. Wang, G. Cheng, X. Bao, Phys. Rev. Lett. 76 (1996) 604.
[272] M. Ikezawa, T. Okuno, Y. Masumoto, A.A. Lipovskii, Phys. Rev. B 64 (2001) 201315.
[273] T.D. Krauss, F.W. Wise, Phys. Rev. Lett. 79 (25) (1997) 5102.
[274] G. Mariotto, M. Montagna, G. Viliani, E. Duval, S. Lefrant, E. Rzepka, C. Mai, EuroPhys. Lett. 6 (1988) 239.
[275] J. Hernandez-Rosas, M. Picquart, E. Haro-Poniatowski, M. Kanehisa, M. Jouanne, J.F. Morhange, J. Phys. Cond. Matter 15 (2003) 7481.
[276] G. Irmer, J. Monecke, P. Verma, G. Goerigk, M. Herms, J. Appl. Phys. 88 (2000) 1873.
[277] A. Roy, A.K. Sood, Solid State Comm. 97 (1996) 97.
[278] D.B. Murray, L. Saviot, Phys. Rev. B 69 (2004) 094305.
[279] L. Saviot, D.B. Murray, M.d.C. Marco de Lucas, Phys. Rev. B 69 (2004) 113402.
[280] N.N. Ovsyuk, V.N. Novikov, Phys. Rev. B 53 (1996) 3113.
[281] G. Bachelier, A. Mlayah, Phys. Rev. B 69 (2004) 205408.
[282] O.L. Lazarenkova, A.A. Balandin, Superlattices and Microstructures 33 (2003) 95.
[283] M. Rajalakshmi, A.K. Arora, Nanostruct. Mater. 11 (1999) 399.
[284] P. Nandakumar, C. Vijayan, M. Rajalakshmi, A.K. Arora, Y.V.G.S. Murti, Physica E 11 (2001) 377.
[285] D. Shuo, L. Jin-Quan, L. Yu-Long, Chinese Phys. 13 (11) (2004) 1854.
[286] G.G. Siu, M.J. Stokes, Y. Liu, Phys. Rev. B 59 (1999) 3173.
[287] Y.M. Yang, X.L. Wu, L.W. Yang, G.S. Huang, G.G. Siu, P.K. Chu, J. Appl. Phys. 98 (2005) 064303.
[288] J.P. Wittmer, A. Tanguy, J.-L. Barrat, L. Lewis, Europhys. Lett. 57 (2002) 423.
[289] M. Fujii, T. Nagareda, S. Hayashi, K. Yamamoto, Phys. Rev. B 44 (12) (1991) 6243.
[290] C.Q. Sun, T.P. Chen, B.K. Tay, S. Li, H. Huang, Y.B. Zhang, L.K. Pan, S.P. Lau, X.W. Sun, J. Phys. D Appl. Phys. 34 (2001) 3470.
[291] M.S. Benrakkad, M.A. Benitez, J. Esteve, J.M. Lopez-Villegas, J. Samitier, J.R. Morante, J. Micromech. Microeng. 5 (1995) 132.
[292] K.A. Alim, V.A. Fonoberov, A.A. Balandin, Appl. Phys. Lett. 86 (2005) 053103.
[293] L.A. Falkovsky, J. Camassel, Physica B 284–288 (2000) 1145.
[294] S. Karlin, Ph. Colomban, J. Am. Ceram. Soc. 82 (1999) 735.

[295] F. Touati, N. Gharbi, Ph. Colomban, J. Mater. Sci. 35 (2000) 1565.
[296] Ph. Colomban, H. Courret, F. Romain, G. Gouadec, D. Michel, J. Am. Ceram. Soc. 83 (12) (2000) 2974.
[297] A. Kremenovic, Ph. Colomban, B. Piriou, D. Massiot, P. Florian, J. Phys. Chem. Solids 64 (11) (2003) 2253.
[298] D. Michel, Ph. Colomban, S. Abolhassani, F. Voyron, A. Kahn-Harari, J. Eur. Ceram. Soc. 16 (1996) 161.
[299] Ph. Colomban, F. Romain, A. Neiman, I. Animitsa, Solid State Ionics 145 (2001) 339.
[300] R. Dimitrijevic, A. Kremenovic, V. Dondur, M. Tomasevic-Canovic, M. Mitrovic, J. Phys. Chem. B 101 (1997) 3931.
[301] R.A. Barrio, F.L. Galeener, E. Martinez, R.J. Elliott, Phys. Rev. B 48 (21) (1993) 15672.
[302] A. Pasquarello, R. Car, Phys. Rev. Lett. 80 (23) (1998) 5145.
[303] T. Uchino, Y. Kitagawa, T. Yoko, Phys. Rev. B 61 (2000) 234.
[304] A. Rahmani, M. Benoit, C. Benoit, Phys. Rev. B 68 (2003) 184202.
[305] Ph. Colomban, J. Non-Cryst. Sol. 323 (1–3) (2003) 180.
[306] Ph. Colomban, O. Paulsen, J. Am. Ceram. Soc. 88 (2005) 390.
[307] F.A. Seifert, B.O. Mysen, D. Virgo, Am. Miner. 67 (1982) 696.
[308] R. Shuker, R.W. Gammon, Phys. Rev. Lett. 25 (1970) 222.
[309] C. Masciovecchio, V. Mazzacurati, G. Monaco, G. Ruocco, T. Scopigno, F. Sette, P. Benassi, A. Cunsolo, A. Fontana, M. Krisch, A. Mermet, M. Montagna, F. Rossi, M. Sampoli, G. Signorelli, R. Verbeni, Phil. Mag. Pt B, Phys. Cond. Matter 79 (11–12) (1999) 2013.
[310] M.J. Harris, M.T. Dove, J.M. Parker, Miner. Mag. 64 (2000) 435.
[311] M.J. Harris, S.M. Bennington, M.T. Dove, J.M. Parker, Physica B 263–264 (1999) 357.
[312] G. Mariotto, M. Montagna, G. Viliani, R. Campostrini, G. Carturan, J. Phys. C Solid State Phys. 21 (1988) L797.
[313] N.V. Surovtsev, A.P. Sokolov, Phys. Rev. B 66 (2002) 54205.
[314] A. Chmel, V.S. Shashkin, Europhys. Lett. 55 (2001) 235.
[315] A. Roy, A.K. Sood, Solid State Comm. 93 (12) (1995) 995.
[316] A. Boukenter, B. Champagnon, E. Duval, J.L. Rousset, J. Dumas, J. Serughetti, J. Phys. C Solid State Phys. 21 (1988) L1097.
[317] E. Courtens, R. Vacher, Proc. Royal Soc. London A 423 (1864) (1989) 55.
[318] E. Duval, A. Boukenter, T. Achibat, J. Phys. Cond. Matter 2 (1990) 10227.
[319] A.J. Martin, W. Brenig, Phys. Stat. Sol. (b) 64 (1974) 163.
[320] N.V. Surotsev, Phys. Stat. Sol. (c) 1 (11) (2004) 2867.
[321] V.L. Gurevich, D.A. Parshin, H.R. Schober, Phys. Rev. B 67 (2003) 094203.
[322] C. Boulesteix, K.C. Hewitt, J.C. Irwin, J. Phys. Cond. Matter 12 (2000) 9637.
[323] P. Li, W. Yang, P. Tan, H. Wen, Z. Zhao, Phys. Rev. B 61 (17) (2000) 11324.
[324] K.C. Hewitt, N.L. Wang, J.C. Irwin, D.M. Pooke, A.E. Pantoja, H.J. Trodahl, Phys. Rev. B 60 (1999) R9943.
[325] A. Gruger, A. Regis, T. Schmatko, Ph. Colomban, Vibr. Spectrosc. 26 (215–225) (2001).
[326] I.G. Siny, R.S. Katiyar, A.S. Bhalla, J. Raman Spectrosc. 29 (1998) 358.
[327] T. Runka, R. Aleksiyko, M. Berkowski, M. Drozdowski, Cryst. Res. Technol. 40 (4/5) (2005) 453.
[328] J.-P. Boilot, Ph. Colomban, R. Collongues, G. Collin, R. Conoes, Phys. Rev. Lett. 42 (12) (1979) 785.
[329] R. Collongues, D. Gourier, A. Kahn, J.P. Boilot, Ph. Colomban, A. Wicker, J. Phys. Chem. Sol. 45 (10) (1984) 981.
[330] Ph. Colomban, F. Fillaux, J. Thomkinson, G.J. Kearley, Solid State Ionics 77 (1995) 45.
[331] S.A. Solin Chapter 5, in: H. Zabel, S.A. Solin (Eds.), Graphite Intercalation Compounds I. Structure and Dynamics, vol. 157, Springer-Verlag, 1990.
[332] C. Thomsen, S. Reich, Phys. Rev. Lett. 85 (24) (2000) 5214.
[333] M. Havel, Ph. Colomban, Composites B 35 (2004) 139.
[334] E. Tomasella, L. Thomas, C. Meunier, M. Nadal, S. Mikhailov, Surf. Coat. Technol. 174–175 (2003) 360.
[335] E. Tomasella, C. Meunier, S. Mikhailov, Surf. Coat. Technol. 141 (2001) 286.
[336] A.H. Jayatissa, F. Sato, N. Saito, H. Ohnishi, K. Takizawa, Y. Nakanishi, T. Yamaguchi, Mater. Sci. Eng. B 55 (1–2) (1998) 143.
[337] W.-Y. Wu, J.-M. Ting, Thin Solid Films 420–421 (2002) 166.
[338] K.W.R. Gilkes, H.S. Sands, D.N. Batchelder, J. Robertson, W.I. Milne, Appl. Phys. Lett. 70 (15) (1997) 1980.
[339] M. Yoshikawa, G. Katagiri, H. Ishida, A. Ishitani, T. Akamatsu, Appl. Phys. Lett. 52 (19) (1988) 1639.
[340] M. Yoshikawa, G. Katagiri, H. Ishida, A. Ishitani, T. Akamatsu, Solid State Comm. 66 (11) (1988) 1177.
[341] H.-J. Scheibe, D. Drescher, P. Alers, Fresenius J. Anal. Chem. 353 (1995) 695.
[342] M. Park, S.M. Camphausen, A.F. Myers, P.T. Barletta, V. Sakhrani, L. Bergman, R.J. Nemanich, J.J. Cuomo, Mater. Lett. 41 (1999) 229.
[343] C. Fauteux, R. Longtin, J. Pegna, M. Boman, J. Appl. Phys. 95 (2004) 2737.

[344] R.C. Mani, S. Sharma, M.K. Sunkara, J. Gullapalli, R.P. Baldwin, R. Rao, A.M. Rao, J.M. Cowley, Electrochem. Solid State Lett. 5 (2002) E32.
[345] B.K. Tay, X. Shi, H.S. Tan, H.S. Yang, Z. Sun, Surf. Coat. Technol. 105 (1998) 155.
[346] H.W. Kroto, J.R. Heath, S.C. O'Brien, R.F. Curl, R.E. Smalley, Nature 318 (6042) (1985) 162.
[347] J.F. Maguire, M.S. Amer, J. Busbee, Appl. Phys. Lett. 82 (16) (2003) 2592.
[348] S. Iijima, Nature 354 (1991) 56.
[349] R.H. Baughman, A.A. Zakhidov, W.A. de Heer, Science 297 (5582) (2002) 787.
[350] C. Thomsen, S. Reich Chapter 3, in: M. Cardona, R. Merlin (Eds.), Light Scattering in Solids IX: Novel Materials and Techniques, Springer, Heidelberg, 2006.
[351] M.S. Dresselhaus, G. Dresselhaus, R. Saito, A. Jorio, Phys. Rep. 409 (2005) 47.
[352] P.C. Eklund, J.M. Holden, R.A. Jishi, Carbon 33 (1995) 959.
[353] E. Richter, K.R. Subbaswamy, Phys. Rev. Lett. 79 (14) (1997) 2738.
[354] J. Kürti, G. Kresse, H. Kuzmany, Phys. Rev. B 58 (14) (1998) 8869.
[355] S. Bandow, S. Asaka, Y. Saito, A.M. Rao, L. Grigorian, E. Richter, P.C. Eklund, Phys. Rev. Lett. 80 (17) (1998) 3779.
[356] H. Kuzmany, W. Plank, M. Hulman, C. Kramberger, A. Grüneis, T. Pichler, H. Peterlik, H. Kataura, Y. Achiba, Eur. Phys. J. B 22 (2001) 307.
[357] R. Saito, T. Takeya, T. Kimura, G. Dresselhaus, M.S. Dresselhaus, Phys. Rev. B 57 (1998) 4145.
[358] A.G. de Souza Filho, A. Jorio, G.G. Samsonidze, G. Dresselhaus, M.S. Dresselhaus, A.K. Swan, M.S. Unlu, B.B. Goldberg, R. Saito, J.H. Hafner, C.M. Lieber, M.A. Pimenta, Chem. Phys. Lett. 354 (2002) 62.
[359] M.A. Pimenta, A. Marucci, S.D.M. Brown, M.J. Matthews, A.M. Rao, P.C. Eklund, R.E. Smalley, G. Dresselhaus, M.S. Dresselhaus, J. Mater. Res. 13 (1998) 2396.
[360] M.S. Dresselhaus, G. Dresselhaus, A. Jorio, A.G. de Souza Filho, R. Saito, Carbon 40 (2002) 2043.
[361] T.W. Odom, J.-L. Huang, P. Kim, M. Ouyang, C.M. Lieber, J. Mater. Res. 13 (1998) 2380.
[362] M. Hulman, R. Pfeiffer, H. Kuzmany, New J. Phys. 6 (2004) 1.
[363] M.A. Pimenta, E.B. Hanlon, A. Marucci, P. Corio, S.D.M. Brown, S.A. Empedocles, M. Bawendi, G. Dresselhaus, M.S. Dresselhaus, Braz. J. Phys. 30 (2000) 423.
[364] V.N. Popov, P. Lambin, Phys. Rev. B 73 (2006) 085407.
[365] K.K. Chawla, Composite Materials Science and Engineering, second ed. Springer-Verlag, New York, 1998.
[366] G. Salvador, W.F. Sherman, J. Mol. Struct. 247 (1991) 373.
[367] W.J. Choyke, G. Pensl, MRS Bull. 22 (1997) 25.
[368] D.W. Feldman, J.H. Parker, W.J. Choyke, L. Patrick, Phys. Rev. 170 (1968) 698.
[369] M. Takeda, J. Sakamoto, A. Saeki, Y. Imai, H. Ichikawa, Ceram. Eng. Sci. Proc. 16 (1995) 37.
[370] K. Kumagawa, H. Yamaoka, M. Shibuya, T. Yamamura, Ceram. Eng. Sci. Proc. 19 (1998) 65.
[371] Dow Corning Corp., Information about Sylramic™ SiC Fiber, Product Inform. Form No.10-754-97, 1997.
[372] S. Karlin, Ph. Colomban, J. Raman Spectrosc. 28 (1997) 219.
[373] S. Karlin, Ph. Colomban, Composites B 29 (1998) 41.
[374] H. Okumura, E. Sakuma, J.H. Lee, H. Mukaida, S. Misawa, K. Endo, S. Yoshida, J. Appl. Phys. 61 (1987) 1134.
[375] Y. Sasaki, Y. Nishina, M. Sato, K. Okamura, J. Mater. Sci. 22 (1987) 443.
[376] S.-I. Nakashima, Y. Nakakura, I. Zenzaburo, J. Phys. Soc. Jap. 56 (1987) 359.
[377] Y.G. Gogotsi, K.G. Nickel, D. Bahloul-Hourlier, T. Merle-Mejean, G.E. Khomenko, K.P. Skjerlie, J. Mater. Chem. 6 (1996) 595.
[378] G. Gouadec, PhD Thesis, Analyse (Micro)-Mécanique et (Nano)-Structurale de Solides Hétérogènes par Spectroscopie Raman, University of Rennes, 1, 2001.
[379] M.-H. Berger, N. Hochet, A.R. Bunsell, Chapter 6, in: A.R. Bunsell, M.-H. Berger (Eds.), Fine Ceramic Fibers, vol. 207, Marcel Dekker Inc., New York, 1999.
[380] J. Lipowitz, J.A. Rabe, K.T. Nguyen, L.D. Orr, R.R. Androl, Ceram. Eng. Sci. Proc. 16 (1995) 55.
[381] M. Takeda, J. Sakamoto, Y. Imai, H. Ichikawa, T. Ishikawa, Ceram. Eng. Sci. Proc. 15 (1994) 133.
[382] T. Ishikawa, Y. Kohtoku, K. Kumagawa, T. Yamamura, T. Nagasawa, Nature 391 (6669) (1998) 773.
[383] M.-H. Berger, N. Hochet, A.R. Bunsell, Ceram. Eng. Sci. Proc. 19 (1998) 39.
[384] D.W. Feldman, J.H. Parker, W.J. Choyke, L. Patrick, Phys. Rev. 173 (1968) 787.
[386] I. Kosacki, V. Petrovsky, H.U. Anderson, Ph. Colomban, J. Am. Ceram. Soc. 85 (11) (2002) 2646.
[387] R.J. Young, J. Microscopy 185 (1996) 199.
[388] C. Vlattas, C. Galiotis, Polymer 32 (10) (1991) 1788.
[389] C. Galiotis, Mater. Technol. 8 (9/10) (1993) 203.
[390] I.J. Beyerlein, M.S. Amer, L.S. Schadler, S.L. Phoenix, Sci. Eng. Comp. Mater. 7 (1–2) (1998) 204.
[391] L.S. Schadler, C. Galiotis, Inter. Mater. Rev. 40 (1995) 116.

[392] Ph. Colomban, Adv. Eng. Mater. 4 (2002) 535.
[393] B. Prinz, E. Schnack, J. Comp. Mater. 31 (1997) 852.
[394] C. Genzel, Phys. Stat. Sol. (a) 165 (1998) 347.
[395] C. Genzel, W. Reimers, Phys. Stat. Sol. (a) 166 (1998) 751.
[396] H. Choo, P. Rangaswamy, M.A.M. Bourke, Evolution of phase fraction and elastic lattice strains in a Ti-6Al-4V/SiC composite during heating: a neutron diffraction study, in: Proceedings of ICCE/6, Orlando, FL, U.S.A., vol. 127, 1999.
[397] M. Dutta, G. Bruno, L. Edwards and M.E. Fitzpatrick, Internal stress changes measured by neutron diffraction in a metal matrix composite after mechanical and thermal treatments, in: Proceedings of ICCE/6, Orlando, FL, U.S.A., vol. 195, 1999.
[398] M. Surgeon, E. Vanswijgenhoven, M. Wevers, O. Van-Der-Biest, Composites A 28 (1997) 473.
[399] S.-C. Wooh, Potential use of ultrasonic phased arrays for non destructive evaluation of concrete and composite materials, in: Proceedings of ICCE/6, Orlando, FL, U.S.A., vol. B41, 1999.
[400] H.E. Gundtoft, K.K. Borum, Characterization of composites by ultrasonic-scanning examples and experience from participation in european and national projects, in: Proceedings of ICCE/6, Orlando, FL, U.S.A., vol. 273, 1999.
[401] B. Fiedler, K. Schulte, Comp. Sci. Technol. 57 (1997) 859.
[402] W.K. Binienda, Photoelastic visualisation of the fracture events in a model of functionaly graded material, in: Proceedings of ICCE/6, Orlando, FL, U.S.A., vol. 65, 1999.
[403] A. Dalmaz, P. Reynaud, D. Rouby, G. Fantozzi, J. Mater. Sci. 31 (1996) 4213.
[404] C. Briançon, P. Sigety, C. G'Sell, Comp. Sci. Technol. 56 (1996) 835.
[405] H.-A. Crostack, G. Fischer, E. Soppa, S. Schmauder and Y.-L. Liu, Localization of strain in metal–matrix composites, in: Proceedings of ICCE/6, Orlando, FL, U.S.A., vol. 223, 1999.
[406] B. Passilly, M. Parlier, Caractérisation Mécanique des Interfaces et des Fibres dans les Composites à Matrice Céramique, Rapport technique ONERA no. 67/3548 MY, 1994.
[407] M. Drissi-Habti, K. Nakano, Comp. Sci. Technol. 57 (1997) 1381.
[408] C.-H. Hsueh, J. Mater. Sci. Lett. 8 (1989) 739.
[409] D.B. Marshall, W.C. Oliver, Mater. Sci. Eng. A 126 (1990) 95.
[410] T. Weihs, W.D. Nix, J. Am. Ceram. Soc. 74 (1991) 524.
[411] P.W.J. van den Heuvel, B. Hogeweg, T. Peijs, Composites A 28 (1997) 237.
[412] W. Wu, M. Desaeger, I. Verpoest, J. Varna, Comp. Sci. Technol. 57 (1997) 809.
[413] R.J. Young, Key Eng. Mater. 116–117 (1996) 173.
[414] J.R. Wood, Y. Huang, R.J. Young, G. Marom, Comp. Sci. Technol. 55 (1995) 223.
[415] D. Lévêque, M.H. Auvray, Comp. Sci. Technol. 56 (1996) 749.
[416] N. Melanitis, C. Galiotis, P.L. Tetlow, C.K.L. Davies, J. Comp. Mater. 26 (1992) 574.
[417] D.J. Bannister, M.C. Andrews, A.J. Cervenka, R.J. Young, Comp. Sci. Technol. 53 (1995) 411.
[418] B. Guichet, J.-C. Sangleboeuf, A. Vassel, T. Bretheau, Comp. Sci. Technol. 58 (1998) 665.
[419] H. Ledbetter, Phys. Stat. Sol. (b) 181 (1994) 81.
[420] J.P. Petitet, Influence de la Pression sur les Spectres Raman. Corrélation avec les Propriétés Intra et Intermoléculaires, in: Proceedings of Ecole Thématique de Spectroscopie Raman en Chimie et Physique des Matériaux, Autrans, France, 1998.
[421] M.A. White, Can. J. Chem. 74 (1996) 1916.
[422] B. Schrader Chapter 1, in: B. Schrader (Ed.), Infrared and Raman Spectroscopy, Methods and Applications, vol. 7, VCH, Weinheim, 1995.
[423] B.A. Weinstein, R. Zallen, in: M. Cardona, G. Güntherodt (Eds.), Topics in Applied Physics, Light Scattering in Solids IV, vol. 463, Springer-Verlag, Heidelberg, Germany, 1984.
[424] A. Jayaraman, Rev. Mod. Phys. 55 (1983) 65.
[425] J.R. Ferraro, Vibrational Spectroscopy at High External Pressures, The Diamond Anvil Cell, Academic Press, New York, 1984.
[426] D. Olego, M. Cardona, P. Vogl, Phys. Rev. B 25 (1982) 3878.
[427] J.F. Di Gregorio, T.E. Furtak, J. Am. Ceram. Soc. 75 (1992) 1854.
[428] J. Liu, Y.K. Vohra, Phys. Rev. Lett. 72 (26) (1994) 4105.
[429] T.L. Schindler, Y.K. Vohra, J. Phys. Cond. Matter 7 (1995) L637.
[430] M. Hanfland, K. Syassen, S. Fahy, S.G. Louie, M.L. Cohen, Phys. Rev. B 31 (10) (1985) 6896.
[431] S.-J. Jeon, D. Kim, S.K. Kim, I.C. Jeon, J. Raman Spectrosc. 23 (1992) 311.
[432] S.H. Tolbert, A.P. Alivisatos, H.E. Lorenzana, M.B. Kruger, R. Jeanloz, Chem. Phys. Lett. 188 (3,4) (1992) 163.

[433] I.V. Aleksandrov, A.F. Goncharov, E.V. Yakovenko, S.M. Stishov, in: Y. Syono, M.H. Manghnani (Eds.), High-Pressure Research: Application to Earth and Planetary Sciences, 409, Terra Scientific Publishing Company/ American Geophysical Union, Tokyo/Washington, D.C., 1992.
[434] E. Anastassakis, A. Pinczuk, E. Burnstein, F.H. Pollak, M. Cardona, Solid State Comm. 8 (1970) 133.
[435] E. Anastassakis, J. Appl. Phys. 82 (1997) 1582.
[436] S.H. Shin, F.H. Pollak, P.M. Raccah, Effects of uniaxial stress on the Raman frequencies of Ti_2O_3 and Al_2O_3, in: Proceedings of Third International Conference on Light Scattering in Solids, Paris, France, vol. 401, 1975.
[437] W. Jia, W.M. Yen, J. Raman Spectrosc. 20 (1989) 785.
[438] T. Englert, G. Abstreiter, J. Pontcharra, Solid State Elec. 23 (1980) 31.
[439] H. Mukaida, H. Okumura, J.H. Lee, H. Daimon, E. Sakuma, S. Misawa, K. Endo, S. Yoshida, J. Appl. Phys. 62 (1987) 254.
[440] J.W. Ager III, M.D. Drory, Phys. Rev. B 48 (1993) 2601.
[441] Y.M. Cheong, H.L. Marcus, F. Adar, J. Mater. Res. 2 (1987) 902.
[442] H. Mohrbacher, K.V. Acker, B. Blanpain, P.V. Houtte, J.-P. Celis, J. Mater. Res. 11 (1996) 1776.
[443] I. De Wolf, H.E. Maes, S.K. Jones, J. Appl. Phys. 79 (1996) 7148.
[444] S. Rohmfeld, M. Hundhausen, L. Ley, C.A. Zorman, M. Mehregany, J. Appl. Phys. 91 (2002) 1113.
[445] T.A. Michalske, D. Tallant, W.L. Smith, Phys. Chem. Glasses 29 (1988) 150.
[446] Ph. Colomban, Proceedings of the Seventh CIMTEC, Montecatini Terme, It., vol. 599, Elsevier Publisher B.V., Amsterdam, 1991.
[447] R.J. Young, D. Lu, R.J. Day, W.F. Knoff, H.A. Davis, J. Mater. Sci. 27 (1992) 5431.
[448] G. Chollon, R. Pailler, R. Naslain, Ceram. Trans. 58 (1995) 299.
[449] G. Chollon, R. Pailler, R. Naslain, P. Olry, J. Mater. Sci. 32 (1997) 1133.
[450] P.A. Tarantili, A.G. Andreopoulos, C. Galiotis, Macromolecules 31 (1998) 6964.
[451] N. Melanitis, P.L. Tetlow, C. Galiotis, S.B. Smith, J. Mater. Sci. 29 (1994) 786.
[452] C. Filiou, C. Galiotis, D.N. Batchelder, Composites 23 (1992) 28.
[453] N. Melanitis, C. Galiotis, J. Mater. Sci. 25 (12) (1990) 5081.
[454] M.S. Amer, L.S. Schadler, Comp. Sci. Technol. 57 (1997) 1129.
[455] R.J. Young, R.J. Day, Br. Polymer J. 21 (1989) 17.
[456] P.W.J. van den Heuvel, T. Peijs, R.J. Young, Comp. Sci. Technol. 57 (1997) 899.
[457] V. Chohan, C. Galiotis, Comp. Sci. Technol. 57 (1997) 1089.
[458] C. Galiotis, A. Paipetis, C. Marston, J. Raman Spectrosc. 30 (10) (1999) 899.
[459] A. Paipetis, C. Galiotis, Comp. Sci. Technol. 57 (1997) 827.
[460] C. Marston, B. Gabbitas, J. Adams, P. Marshall, C. Galiotis, Comp. Sci. Technol. 57 (1997) 913.
[461] P.W.J. van den Heuvel, T. Peijs, R.J. Young, J. Mater. Sci. Lett. 15 (1996) 1908.
[462] M.S. Amer, L.S. Schadler, J. Raman Spectrosc. 30 (10) (1999) 919.
[463] S. Narayanan, L.S. Schadler, Comp. Sci. Technol. 59 (10) (1999) 1589.
[464] M.C. Andrews, R.J. Young, J. Raman Spectrosc. 24 (1993) 539.
[465] J.A. Bennett, R.J. Young, Comp. Sci. Technol. 57 (1997) 945.
[466] C. Galiotis, I.M. Robinson, R.J. Young, B.J.E. Smith, D.N. Batchelder, Polymer Comm. 26 (1985) 354.
[467] S. van der Zwaag, M.G. Northolt, R.J. Young, I.M. Robinson, C. Galiotis, D.N. Batchelder, Polymer Comm. 28 (1987) 276.
[468] H.D. Wagner, M.S. Amer, L.S. Schadler, J. Mater. Sci. 31 (1996) 1165.
[469] M. Kawagoe, S. Hashimoto, M. Nomiya, M. Morita, J. Qiu, W. Mizuno, H. Kitano, J. Raman Spectrosc. 30 (1999) 913.
[470] P. Masse, J.P. Cavrot, C. Depecker, J. Laureyns, B. Escaig, Macromol. Symp. 94 (1995) 249.
[471] C.A. Cooper, R.J. Young, M. Halsall, Composites A 32 (2001) 401.
[472] J.Z. Wan, F.H. Pollak, B.E. Dorfman, J. Appl. Phys. 81 (1997) 6407.
[473] X. Yang, D.J. Bannister, R.J. Young, J. Am. Ceram. Soc. 79 (1996) 1868.
[474] J. Wu, Ph. Colomban, J. Raman Spectrosc. 28 (1997) 523.
[475] G. Gouadec, S. Karlin, J. Wu, M. Parlier, Ph. Colomban, Comp. Sci. Technol. 61 (2001) 383.
[476] X. Yang, R.J. Young, Composites 25 (1994) 488.
[477] X. Yang, R.J. Young, Br. Ceram. Trans. 93 (1994) 1.
[478] X. Yang, R.J. Young, J. Mater. Sci. 28 (1993) 2536.
[479] F. Bollet, C. Galiotis, M.J. Reece, Proceedings of the Seventh European Conference on Composite Materials, vol. 505, Woodhead Publishing Ltd., Cambridge, UK, 1996.
[480] G. Pezzotti, J. Raman Spectrosc. 30 (10) (1999) 867.
[481] G. Chollon, J. Takahashi, Proceedings of "JNC11", Arcachon, France, vol. 777, Editions AMAC, Paris, 1998.

[482] S. Karlin, PhD Thesis, Analyse Chimique et Mécanique ex situ et in situ, de Fibres et Composites Céramiques (CMC), Apport de la Microscopie Raman, University of Montpellier 2-Sci. et Techn. du Languedoc, 1996.
[483] M. Monthioux, O.P. Bahl, R.B. Mathur, T.L. Dhami, H.O. Dwivedi, S.P. Sharma, Carbon 38 (2000) 475.
[484] D.D. Edie, Carbon 36 (1998) 345.
[485] Ph. Colomban, G. Gouadec, J. Mathez, J. Tschiember, P. Pérès, Composites Part A Appl. Sci. Manuf. 37 (2006) 646.
[486] Y.G. Gogotsi, A. Kailer, K.G. Nickel, Mater. Res. Innov. 1 (1997) 3.
[487] M.S. Amer, J. Busbee, S.R. Leclair, J.F. Maguire, J. Johns, A. Voevodin, J. Raman Spectrosc. 30 (1999) 947.
[488] X.J. Ning, P. Pirouz, J. Mater. Res. 6 (10) (1991) 2234.
[489] A.B. Mann, M. Balooch, J.H. Kinney, T.P. Weihs, J. Am. Ceram. Soc. 82 (1999) 111.
[490] R. El-Mallawany, A. Abd-El-Moneim, Phys. Stat. Sol. (a) 166 (1998) 829.
[491] R.J. Day, I.M. Robinson, M. Zakikhani, R.J. Young, Polymer 28 (1987) 1833.
[492] B.J. Kip, M.C.P. Van-Eijk, R.J. Meier, J. Polym. Sci. B 29 (1991) 99.
[493] C. Hierold, J. Micromech. Microeng. 14 (2004) S1.
[494] O. Lourie, H.D. Wagner, J. Mater. Res. 13 (1998) 2418.
[495] J.R. Wood, Q. Zhao, M.D. Frogley, E.R. Meurs, A.D. Prins, T. Peijs, D.J. Dunstan, H.D. Wagner, Phys. Rev. B 62 (11) (2000) 7571.
[496] Q. Zhao, M.D. Frogley, H.D. Wagner, Comp. Sci. Technol. 61 (2001) 2139.
[497] G. Gouadec, J.-P. Forgerit, Ph. Colomban, Comp. Sci. Technol. 62 (2002) 505.
[498] P. Puech, A. Bassil, J. Gonzalez, Ch. Power, E. Flahaut, S. Barrau, Ph. Dernont, C. Lacabanne, E. Perez, W.S. Basca, Phys. Rev. B 72 (2005) 155436.
[499] G. Gouadec, Ph. Colomban, Key Eng. Mater. 206–213 (2002) 617.

Gwénaël Gouadec (born in 1973) is Associate Professor at Pierre & Marie Curie (Paris VI) University where he teaches Physical Chemistry. He took an Engineering degree in Materials Science from the University of Rennes in 1996 and served his French National Duty period at ONERA, the French Aeronautics and Space Research Centre, developing Sol–Gel interphases for Al_2O_3/Al_2O_3 Composites. In 2001, he got a Ph.D. on the "Physical and Chemical Characterization of Aerospace Ceramic Matrix Composites by Raman (micro)-Spectroscopy". In 2002, he was appointed as post-doctoral fellow at the University of Alabama at Birmingham. His Research project on the nano-compressibility of carbon micro-ballons was funded by Los Alamos National Laboratory (LANL). In 2003, Dr. Gouadec joined the Laboratoire de Dynamique Interaction et Réactivité (LADIR). He now specializes in the Raman Spectroscopy of nanocrystalline and amorphous domains found in fibres reinforcing Polymer and Ceramic Matrix Composites (PMC/CMC).

Philippe Colomban (born in 1952) is the Head of the "*Laboratoire de Dynamique, Interaction et Réactivité*", a CNRS and Pierre & Marie Curie (Paris VI) University joint laboratory. He got his Engineering degree from Sèvres "*Ecole Nationale Supérieure de Céramique Industrielle*" in 1975 and a Ph.D. degree from Paris VI University in 1979. In 1975, Dr. Colomban was at Thomson-CSF (now Thalès) Central Laboratory one of the first to develop Sol–Gel routes for advanced ceramics (PLZT optically clear ferroelectric ceramics). In 1976 he was appointed as CNRS Research Associate at the "*Ecole Nationale Supérieure de Chimie de Paris*" and studied superionic conductors structure and ion mobility. In 1980 he created the Solid State Chemistry Group at the "*Ecole Polytechnique*", focusing on Nasicon solid electrolytes, proton conductors and Sol–Gel ceramics and became a Consultant for the French Science and Technology Minister. From 1989 to 1993 Dr. Colomban took charge of the new projects at the Materials Department of ONERA, the French Aeronautics and Space Research Establishment (Sol–Gel routes, Oxide–oxide ceramic–matrix composites, microwave absorbing materials and Functionally-Graded composites, etc.). From 1994 to present, as a CNRS Senior Scientist, his research specialized in the use of Raman, IR and neutron spectroscopies for in situ stress and phase distribution imaging (in composites, solid state devices, fuel cells, synthetic and natural fibres) and the identification of the technologies used for the fabrication of ancient ceramics and glasses. Philippe Colomban was an invited speaker at International Conferences on many different topics. His publications comprise more than 300 original papers and reviews, and five patents. He is a board member of Composite Part B Journal, Editor of Taoci (the series of the French Oriental Ceramic Society) and received the Société Française de Chimie (SFC) "Solid State Chemistry Award" in 1984.